# Non-invasive Imaging and Single-cell Analysis of Three-dimensional Bacterial Biofilms

Mingxing Zhang
Anhui, China

B.S. in Chemical Engineering and Technology, Dalian University of Technology, 2010

M.S. in Physical Chemistry, Dalian University of Technology, 2013

A Dissertation presented to the Graduate Faculty of the University of Virginia in Candidacy for the Degree of Doctor of Philosophy

Department of Chemistry

University of Virginia
November 2020

Andreas Gahlmann
David Cafiso
Ian Harrison
Kevin Lehmann
Acton, Scott T.

## ACKNOWLEDGEMENTES

There are many people that I must thank for their help and support in the pursuit of my education.

First, I would like to thank my advisor Dr. Andreas Gahlmann for helping me become a confident and capable scientist. His enthusiasm for, and commitment to, his work and to his students is truly inspiring. His unwavering support for me and our work offers me the success that I've had in my graduate school career. I would also like to thank Dr. David Cafiso, Dr. Ian Harrison, Dr. Kevin Lehmann and Dr. Acton, Scott T. for both serving in my research committee and support in my work.

I need to also acknowledge all group members of the Gahlmann lab and Jie of the Scott lab for their support and hard work. I would especially like to thank Ji, Yibo and Jie. Ji and I worked together to solve a lot of questions, such as constructing the lattice light sheet microscopy, developing the flow chamber system and designing protocols to image bacterial biofilms. Ji, Yibo, Jie and I collaborated on the bacterial cell segmentation project. I would not have survived without you guys' help. I am thankful for all of the experiences we shared. I need to also thank Ting, my desk-mate. Sharing with her thoughts on reading added characteristics of poetry to our lives in the lab. She is also good at drawing. I wish her success in academia and in pursuit of art. I would like to thank Alecia for her help on the wet lab experiments. I wish she finds success in her graduate school career. Finally I want to thank Josh, who has helped me a lot on proofreading my thesis.

Of course I need to thank my family, as they have continued to support me throughout my life. Without their support I would never have been able to pursue the level of education that I have and I would not be the person I am today.

# ABSTRACT

Tissue-like 3-dimensional (3D) microbial communities called biofilms colonize a wide variety of biotic and abiotic surfaces and, in aggregate, constitute a major component of bacterial biomass on earth. As such, biofilms have a tremendous impact on the biogeochemistry of our planet and the biochemistry of higher living organisms. However, how macroscopic biofilm properties, such as its tolerance up to 1000 times higher concentrations of antibiotic drugs, its mechanical adhesion/cohesion and its biochemical metabolism, emerge from the collective actions of individual bacteria remains unclear.

There are two critical barriers to study single cell behaviors within thick 3D biofilms in a non-invasive manner. First, conventional imaging modalities are not able to non-invasively resolve individual cells within thick 3D biofilms. Second, accurate cell detection and cellular shape measurements in densely packed biofilms are challenging because of the limited resolution and low signal to background ratios (SBRs) in fluorescence microscopy images. The focus of the research described in this dissertation is to solve these problems.

To image bacterial biofilms with cellular/subcellular resolution, we used lattice light-sheet microscopy (LLSM), a new imaging technology that effectively combines low photo-toxicity and high spatiotemporal resolution. To enable growing and imaging biofilms, especially pathogenic species, at high resolution, we designed a flow chamber system that is compatible with LLSM. To accurately segment and classify single bacterial cells in 3D fluorescence images, we developed Bacterial Cell Morphometry 3D (*BCM3D*), an image analysis workflow that combines deep learning with mathematical image analysis.

Compared to state-of-the-art bacterial cell segmentation approaches, *BCM3D* consistently achieves higher segmentation accuracy and further enables automated morphometric cell classifications in multi-population biofilms. The accurate segmentation results from *BCM3D* provide precise single-cell observables, including cell positions, orientation, morphologies, volumes and fluorescent intensities. We developed a multi-cell tracking method by utilizing these cell observables to associate the same cells imaged at different time points.

The integrated workflow, namely non-invasive imaging biofilms with subcellular resolution, accurate segmentation and classification of single bacterial cells in 3D fluorescence images and tracking multi-cell in the segmentation results are applied to study the diffusive behavior of individual cells in *Shigella flexneri* biofilms.

## Table of Contents

# Glossary

| | |
|---|---|
| **AOGM** | Acyclic oriented graph matching |
| **AOTF** | Acousto-optic tunable filter |
| **API** | Application programming interface |
| **BCM3D** | Bacterial Cell Morphometry 3D |
| **CA** | Cholate acid |
| **CBD** | Calgary biofilm device |
| **CFP** | Cyan fluorescent protein |
| **CNNs** | Convolutional neural networks |
| **CSLM** | Confocal scanning laser microscopy |
| **CV** | Coefficient of variation |
| **DAPI** | 4', 6-Diamidino-2-phenylindole dilactate |
| **DOC** | Deoxycholate |
| **EABs** | Electrochemically active biofilms |
| **ECM** | Extracellular matrix |
| **EET** | Extracellular electron transfer |
| **EGFP** | Enhanced green fluorescent protein |
| **EPS** | Extracellular polymeric substances |
| **FEP** | Fluorinated ethylene propylene |
| **FWHM** | Full width at half maximum |
| **FOV** | Field of view |
| **GFP** | Green fluorescent protein |

| | |
|---|---|
| **GT** | Ground truth |
| **IoU** | Intersection-over-Union |
| **LCuts** | Linear cuts |
| **LED** | Light-emitting diode |
| **LLSM** | Lattice light sheet microscopy |
| **MRD** | Modified Robbins device |
| **MSD** | Mean squared displacement |
| **MTP** | Microtiter plate |
| **NA** | Numerical aperture |
| **OD** | Optical density |
| **PI** | Propidium iodide |
| **PSF** | Point spread function |
| **RFP** | Red fluorescent protein |
| **SBRs** | Signal to background ratios |
| **sCMOS** | scientific Complimentary metal-oxide semiconductor |
| **SLM** | Spatial light modulator |
| **TRA** | Tracking accuracy |
| **YFP** | Yellow fluorescent protein |

# Chapter 1: Introduction

## 1.1 Overview

Tissue-like 3-dimensional (3D) microbial communities called biofilms colonize and grow on a wide variety of biotic and abiotic surfaces and constitute a major component of bacterial biomass on earth (1-3). As such, biofilms have been widely recognized for their impact on the biogeochemistry of our planet and the biochemistry of higher living organisms, including humans (4, 5). Electrochemically active biofilms (EABs), such as *Shewanella* and *Geobacter* species are capable of extracellular electron transfer (EET) to insoluble minerals or electrode, which are used as electron acceptors for their anaerobic respiration (6-18). The EET process plays critical role in mineral cycling, including not only carbon and iron but also trace metals, metalloids and phosphates (6, 10, 11, 13). To harness this capability, microbial fuel cells (MFCs) that convert the energy stored in organic compound to electrical energy by the catalytic reaction of microorganism have been invented (12, 17, 19-26). In medical settings, pathogenic biofilms are responsible for both acute and chronic infections. For example, *Pseudomonas aeruginosa* biofilms were found in the respiratory tract of cystic fibrosis patients (27-30). *Shigella flexneri* is an intracellular bacterial pathogen that leads to bloody diarrhea by invading epithelial cells in the colonic mucosa (31-37). Previous studies found that *S. flexneri* forms biofilms under the presence of the bile salts, deoxycholate (DOC) and cholate acid (CA) (33, 36, 38). It has been reported that about 1 million hospital-acquired infections each year are biofilm-mediated and these infections result in an estimated 100’000 deaths per year (39-42).

To enable either the efficient removal of pathogenic biofilms in medical settings or the rational design of microbial ecosystems with desirable biomedical and bioengineering

capabilities (19, 43-45), it is necessary to understand how macroscopic biofilm properties, such as its size and shape, its mechanical cohesion/adhesion, and its biochemical metabolism, emerge from the collective actions of individual bacteria. Specifically, we need to understand the biochemical and mechanical mechanisms employed by bacteria to cooperate or antagonize each other in spatially and temporally heterogeneous biofilm microenvironments (46-53). However, due to the complexity of biofilms, the lack of non-invasive imaging methods, and the scarcity of reliable single cell segmentation methods for thick 3D biofilm images, it is still challenging to study single cell behaviors in dense 3D biofilms.

## 1.2 Biofilm Formation

Biofilm formation can be categorized into four main stages: (1) reversible bacterial adhesion to a surface (**Figure 1a**); (2) irreversible attachment (microcolony formation, **Figure 1b**); (3) biofilm maturation (**Figure 1c**); and (4) bacterial dispersion (**Figure 1d**). Each stage is represented by unique phenotype. The first stage, initial reversible adhesion, is partially stochastic, driven by Brownian motion and influenced by environmental factors such as shear forces, pH, ionic strength, temperature, and van der Waals and electrostatic interactions between bacterial and host surfaces (3, 54-58). Previous studies also found that flagellar motility is important for initial attachment of several pathogenic species, including *P. aeruginosa*, *Vibrio cholerae*, and *E. coli* (59-63).

The second stage, irreversible attachment (microcolony formation), is achieved by bacterial cells that can tolerate surrounding hydrodynamic forces and stay on the surface.

Different types of pili and bacterial surface anchor proteins are involved in this stage (59, 62, 64-66). For example, in addition to flagella, *P. aeruginosa* uses type IV pili-mediated twitching motility to maintain adherence, and move across the attachment surface (59, 62).

The third stage, biofilm maturation, is initiated with the production of extracellular polymeric substances (EPS), a matrix typically composed of extracellular DNA, proteins and polysaccharides (58, 67, 68). The matrix supports the three-dimensional structure of the biofilm. During or after biofilm maturation, cell dispersal becomes an option for maintaining biofilm architecture and creating a beneficial environment for the resident bacterial cells to live (56). Biofilm dispersal can be induced by several different environmental factors, such as shear stresses, nutrient concentration, oxygen concentration and accumulation of toxic products (69-72). Bacteria have developed to gauge whether it is beneficial to reside within the biofilm or resume a planktonic lifestyle in response to environmental changes (56, 69-72). The released cells could then colonize other regions to form new biofilms.

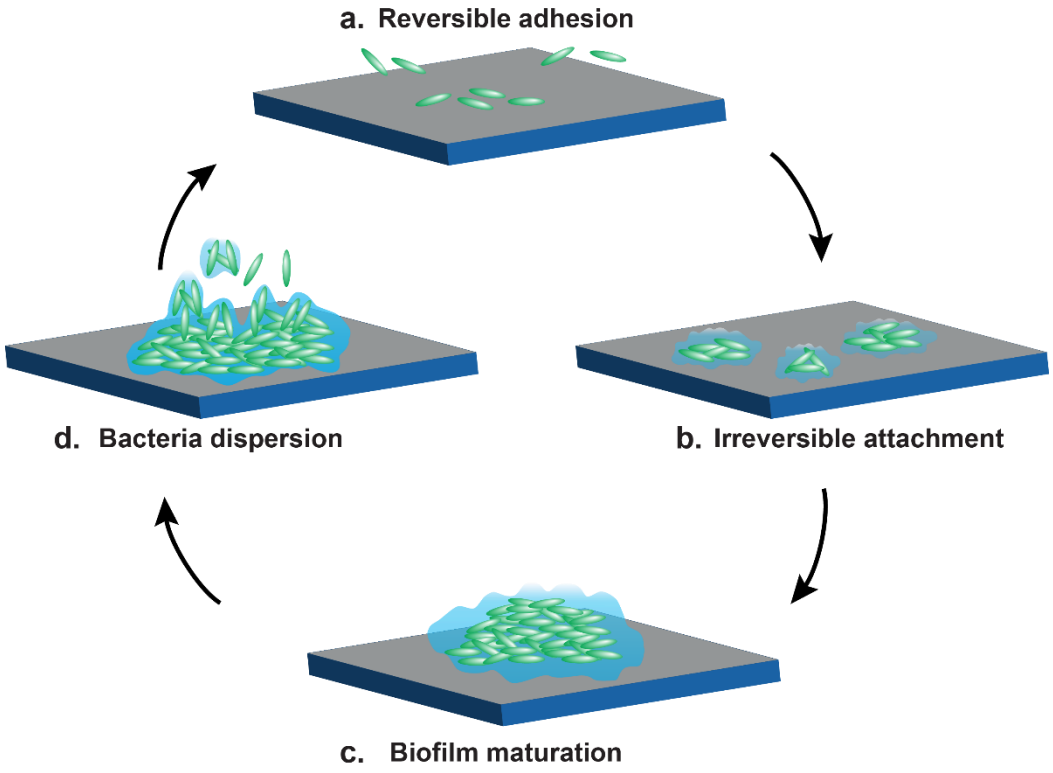


**Figure 1.1** Biofilm formation steps. Biofilm formation are generally categorized into four main stages: (a) reversible bacterial adhesion to a surface, (b) irreversible attachment (microcolony formation), (c) biofilm maturation, and (d) bacterial dispersion.

### 1.3 Biofilm Complexity

The complexity of biofilms is due to the fact that biofilms are inherently heterogeneous (73, 74). In multi-species biofilms, the biofilm structure is optimized for different organisms to have the best opportunity to access oxygen and nutrients (74-77). In single-species biofilms, subpopulations in the community can also show heterogeneous features. The reason for the generation of biofilm heterogeneity can be generalized into the following three aspects (73, 74). First, physiological heterogeneity, caused by bacterial

cells' adaptation to their local microenvironments. When metabolic substrates, such as oxygen and nutrients diffuse into biofilms and are consumed by bacterial cells, chemical concentration gradients are created. The gradients of waste products or secreted bacterial-signaling compounds will also develop within biofilms. The chemical gradients result in forming locally different microenvironments within biofilms. The physiology of individual cells will vary depending on the responses of the bacteria to their local environmental conditions (74, 78-80). Second, genetic variation, where mutations may occur during the growth of bacterial cells in biofilms. Cells within the community may develop variant subpopulations with colony morphologies that are different from the parent strain (81, 82). This phenomenon has been found in a wide range of bacterial species. For example, the formation of colonies with rough and wrinkly appearance in *P. aeruginosa* biofilms (**Figure 1.2 a, b**) (83, 84). Another example is the formation of rugose colonies in *Vibrio cholerae* biofilms (**Figure 1.2 c, d**) (85). Third, stochastic gene expression, where bacterial cells express the same genes at different levels independent of the prevailing environmental conditions (74, 86-91). Bacteria evolved 'division of labor' strategy by expressing the same genes at different levels to increase the functional complexity of biofilms (74, 92). This cooperative behavior can increase the overall fitness of the microbial population (93, 94). Stochastic gene expression events contribute to the formation of the persister cells in biofilms (74, 95-98). The persister cells are a subpopulation of the community, which might be in dormant state and less susceptible to antibiotics. Under the treatment of antibiotics, the susceptible cells are killed, but the persister cells can regenerate the biofilms after antibiotic drugs are removed.

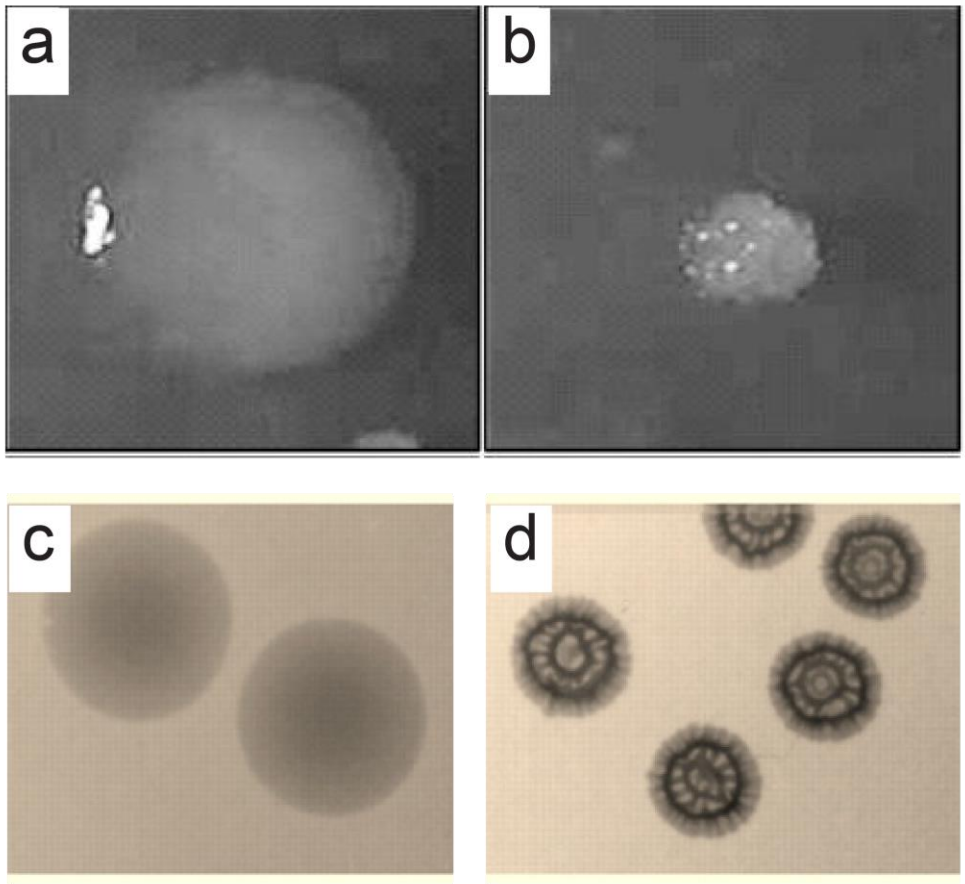


**Figure 1.2** Variant subpopulations with different colony morphologies. Reprinted from (83, 85) with permission. (a) Appearance of wild type *P. aeruginosa* colony morphology on solid medium. (b) Variant colonies of *P. aeruginosa* with small, wrinkled appearance. (c) Colonies of *V. choleare* with the smooth appearance grown on LB agar. (d) Colonies of *V. choleare* with the smooth rugose appearance. c, d ©Copyright (1999) National Academy of Sciences.

Due to the complex structure of biofilms, phenotype diversity and coordination of cellular behaviors within biofilms, bacterial populations obtain emergent capabilities beyond those of individual planktonic cells (1, 3, 57, 99). For example, biofilms are orders

of magnitude more tolerant towards physical, chemical, and biological stressors, most notably high resistance to antibiotic drugs (99, 100). The biofilm matrix, EPS makes important contribution for bacterial cells within biofilms obtaining the high tolerance to the environmental stressors (101). For example, the complex nature of the EPS do not only limit the depth that antibiotics could penetrate into biofilms (102, 103), but could also interact with antimicrobial agents, and finally leading to a decrease of their activities (68, 104).

The above-mentioned heterogeneous features of biofilms make it challenging to inspect live biofilms from cellular/subcellular level. Divergent local microenvironments in biofilms can vary the signal for inspection. For example, bacterial cells under different local microenvironments in biofilms express fluorescent proteins at different level. This will result in non-uniform fluorescence signal across the biofilm. Imaging biofilms with non-uniform fluorescence will cause extra challenges in imaging processing. The dense 3D structure and the complicated EPS components of biofilms add more barriers for signal detection. Taking microscopic imaging as an example, both of them will impact light penetration and increase the background noise, which will finally produce low quality images. To conduct desired studies on single cell behaviors in heterogeneous biofilms, the first requisite is the ability to image biofilms with cellular/subcellular resolution, in other words, advanced microscopy techniques.

## 1.4 Biofilm Imaging

### 1.4.1 Imaging Techniques

Among different types of tools for biofilm studies, microscopy techniques provide the direct way to inspect biofilms *in vivo* (74, 105-131). Among different kinds of microscopy techniques, confocal scanning laser microscopy (CSLM) has been the most widely used one (Figure 3a) (111, 113, 117, 118, 122, 127, 132). CSLM is the powerful microscopic technique to unravel the spatial structure and associated functions of biofilms. Even though powerful, CSLM is disadvantaged by its intrinsic limitations including insufficient resolution, slow data acquisition speed and photodamage. The diffraction-limited axial z-resolution (~570 nm) is comparable to the diameter of a single bacterial cell, so that densely-packed cells quickly become unresolvable in the axial z-dimension. In CSLM, information is collected from a single point, the confocal volume. The point must be scanned through all three spatial dimensions, in order to build up 3D images. The scanning process will cause two problems. First, the scanning driven by mechanical devices, such as galvanometer mirror, limits the image acquisition speed of CSLM. Second, in confocal microscopy, the undesired out-of-focus fluorescence emission is filtered out by confocal pinholes to yield high signal-to-background ratios (SBRs), but the repeated illumination of out-of-focus regions during laser scanning and the high light intensities at the focal volume induce undesired photodamage to the specimen (phototoxicity) and photobleaching to the fluorophores used for labeling (133-135), especially in long-term imaging experiments. These limitations make confocal-based microscope not able to

resolve single bacterial cells in dense and thick (>10 micrometers) biofilms in a non-invasive manner.

Light sheet microscopy has been developed to overcome the drawbacks of confocal-based microscopy (108, 136). Herein, the excitation beam is engineered into a thin sheet and the emission fluorescence is imaged onto a camera by a perpendicular lens (**Figure 1.3b**). To improve the axial resolution that is determined by the thickness of the excitation light sheet, several optical configurations have been developed to create thinner light sheets. Among these, lattice light sheet microscopy (LLSM) (137, 138) and field synthesis variants thereof (139), axially-swept light sheet microscopy (ASLM) (140, 141), and single-objective oblique plane light sheet microscopes (142-145) now combine excellent 3D spatial resolution (200-400 nm) with fast temporal resolution (up to the scale of ms) and low phototoxicity which is two or three orders of magnitude smaller than that of the confocal microscopy modalities (137, 146-148). Long-term imaging is necessary to study biofilm development which occurs in the time scale from hours to days. Imaging over a long period of time will have higher chance to cause photodamage and photobleaching to the biofilm sample. Thus, light sheet-based microscopy which combines subcellular resolution with fast temporal resolution and low phototoxicity, is a more suitable imaging technique to study biofilms than confocal-based microscopies. LLSM can cover length scales differing by 4 orders of magnitude (~200 nm to 2000 μm) and time scales differing by 7 orders of magnitude (ms to days). The ability to acquire 3D movies of living cells that contain information spanning orders of magnitude in length- and time-scales enables the measurement of the spatial, phenotypic, and developmental trajectories

of individual cells in 3D biofilms over multiple hours and days. The work described in this dissertation utilizes a home-built LLSM, described in detail in Chapter 2.

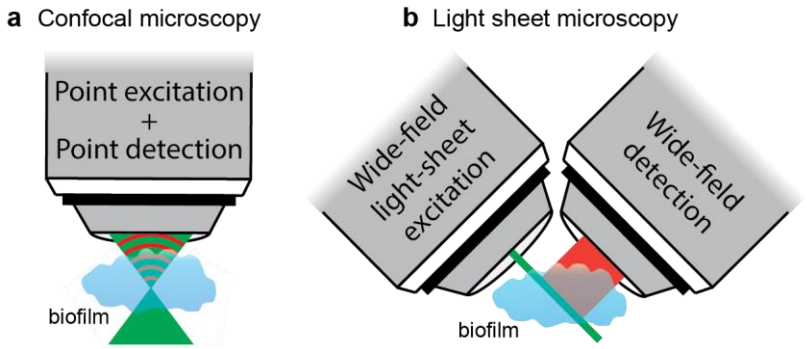


**Figure 1.3** Confocal microscopy and light sheet microscopy. (a) Confocal microscopy, 3D images is constructed by scanning the sample with a single point, the confocal volume. (b) Light sheet microscopy, the excitation and detection objectives are orthogonally installed. 3D images is constructed by scanning the sample with a thin light sheet.

### 1.4.2 Labeling Methods

To be imaged with a fluorescent microscope, biofilms need to be labeled with fluorescent probes. In general, the fluorescence labeling methods can be categorized into two types, fluorescent proteins labeling and fluorescent dyes labeling. Labelling cells with fluorescent proteins can be achieved by either introduction of a plasmid that contains the fluorescent protein gene or incorporation of the fluorescent protein gene into the chromosomal DNA. Green fluorescent protein (GFP) and variants of GFP, such as enhanced green fluorescent protein (EGFP), are the most commonly used ones. Cyan

fluorescent protein (CFP), yellow fluorescent protein (YFP) and red fluorescent protein (RFP) allow for multicolor labeling of different cells in biofilms of multiple species or different components in biofilms of single species (86, 88, 149). The two most attractive features of fluorescent proteins labelling are the high specificity due to genetic encoding and enabling visualization of the 3D architecture of the biofilm cells during biofilm development. Fluorescent proteins are also particularly useful for tracking gene expression within biofilms (86, 88, 149). However, a disadvantage of fluorescent proteins is that their fluorescence brightness are ~10 times lower than organic dyes.

The other option to label biofilms is to stain biofilms with fluorescent dyes. Many fluorescent dyes are commercially available for designing experiments with different goals. For example, DAPI (4', 6-Diamidino-2-phenylindole dilactate) is highly selective for nucleic acids (150), while FM 4-64 stains the cell membrane (151). Propidium Iodide (PI) will not stain live cells because it is not cell membrane permeable (152-154), while SYTO-9 can freely enter live cells and stain nucleic acids (152, 154, 155). Therefore, PI and SYTO-9 can provide information about cell viability. Fluorescent dyes can often provide brighter fluorescence than fluorescent proteins. However, one issue of using fluorescent dyes is that dense and thick biofilms may limit the penetration depth of dyes. It may result in incomplete and non-uniform labeling of the biofilm. Both the fluorescent protein and dye labeling methods are used in this dissertation. Specifically, *S. flexneri* and *Shewanella oneidensis* MR-1 strains are labeled with GFP. *Myxococcus xanthus* strains are labeled with PAmCherry or FM 4-64 depending on the requirements of different experiments, as described in Chapters 2 and 4.

### 1.4.3 Biofilm Formation Device for Imaging

Polystyrene microtiter plates are the most commonly used device for biofilm formation. The classical procedure is to grow bacterial cells in the wells of a microtiter plate (59, 156, 157). In these assays, the biofilm can be quantified by measuring all biomass attached to the surface of the wells. The Calgary biofilm device was derived from the microtiter plates (158). Biofilms grow on the coverlid instead of the surface of the wells. The coverlid is composed of pegs that fit into the wells of the microtiter plate (**Figure 1.4a**).

Microtiter plate devices can only grow biofilm under static conditions, which means hydrodynamic conditions cannot be changed. To overcome this problem, the Robbins device (**Figure 1.4b**), drip flow biofilm reactors (**Figure 1.4c**) and rotary biofilm reactors were developed (159-162). The basic design of these devices are coupons, such as a standard microscope slide, inserted into the liquid stream. The coupons can be removed separately for examination. Those coupon-based devices have been applied to study biofilm formation under controlled conditions, such as different hydrodynamic conditions and different surface materials. However, in order to inspect biofilms in these assays, coupons must be taken out, therefore these devices are not available for direct observation of the biofilm development.

To study biofilm development in real time, flow chamber (**Figure 1.4d**) systems have been developed for direct inspection of live biofilms (163-169). Those devices can be categorized into two types, the open type and the closed type (106). In the open type, the detection devices, like an objective lens of a microscope, can be directly placed in the

media in which biofilms are growing. In the other type, the flow chamber is a closed system but has a detection glass or plastic window on which the biofilm can grow. Then, the biofilm can be imaged from its substratum side through the detection window with microscopes. Flow chamber systems allow real-time monitoring of the growth dynamics of biofilms. Many researches to study the combined effects of several influencing factors on biofilm formation and the *in situ* gene expression in live biofilms have been carried out by the combination of these devices with microscopy techniques (163-165).

Those flow chamber systems have two obvious limitations. First, the open type cannot be used to image for long-term, like several days, since biofilms can develop on the objective lens. This issue will not only disable the microscope for imaging but also raise danger of spreading pathogenic bacteria, such as *P. aeruginosa* and *S. flexneri*. Second, the closed type cannot be applied to study biofilms growing on materials that are not transparent. For example, *Shewanella* and *Geobacter* species form on minerals or electrode that might not be transparent. Considering these limitations, we designed a novel flow chamber system that is compatible with LLSM. This flow chamber system, described in Chapter 3, allows growing biofilm on any materials of interest for long-term imaging under precisely controlled growth conditions. This work has not been published yet

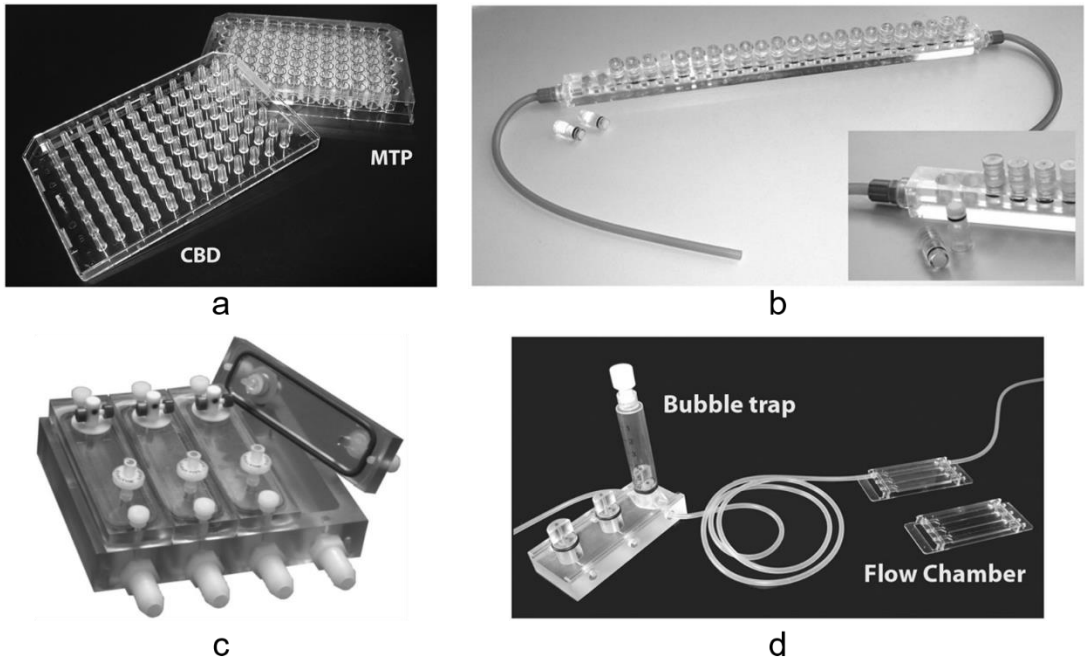


**Figure 1.4** Biofilm formation devices. Adapted from (106), reprinted with permission. (a) The microtiter plate (MTP) system and the calgary biofilm device (CBD). (b) The Modified Robbins Device (MRD). In MRD, coupons are inserted into the liquid stream. The coupons are mounted on small pistons that can be removed for inspection (see the inserted figure). (c) The drip flow biofilm reactor. The commercial version of the drip flow biofilm reactor contains four chambers each accommodating a microscope slide. Biosurface Technologies Corporation © Bryan Warwood. Reuse not permitted. (d) Flow chamber system. It consists of a bubble trap to capture small air bubbles in the medium. (a) (b) and (d) © Claus Sternberg.

### 1.4.4 Data Quantification

Even though biofilms can be imaged with subcellular resolution, data quantification, in specific, single bacterial cell segmentation is still challenging. The heterogeneity of

biofilms not only makes it difficult to image with microscopes but also impact the quality of the acquired images. For example, different local environmental conditions within biofilms can affect the expression of the fluorescence proteins and lead to non-uniform fluorescence signals across the biofilm. When the excitation and emission light penetrate through thick and dense biofilms, both of them can be refracted and/or scattered by the biomass. This issue will attenuate the fluorescence signal and also increase the background noise. Those abovementioned problems will result in low image quality, such as non-uniform fluorescence intensity and low SBRs. Image segmentation, specifically, single-cell segmentation from dense biofilm images thus becomes a critical challenge.

Image processing approaches based on the watershed technique and intensity thresholding have been developed over the years for single-cell segmentation in bacterial biofilms (131, 133, 134, 170). However, these algorithms often require manual optimization of many user-selected parameters, their applicability are thus limited. Moreover, when cell densities are high, when SBRs are low, and when cellular fluorescence intensities are not uniform across the cytosol or the cell surface, watershed- and thresholding-based image processing methods can't produce ideal segmentation results even with optimized parameters.

Deep learning, a machine-learning technique, specifically neural networks, have been widely applied to the quantitative analysis of biological images, including image identification, image segmentation and object tracking (171-175). Several methods, such as DeepCell (174), CDeep3M (176), U-Net (177, 178), CellProfiler (179, 180) and Mask R-CNN (181) software libraries, have been developed and successfully applied to a variety

of data types. Among these methods, U-Net is the milestone in the field of single-cell segmentation (177, 178). Many promising results were obtained with the application of U-Net for cell segmentation. For example, accurate identification of cell contours with U-Net was applied to explore mechanisms of cell size control in fission yeast (182).

Combining deep learning with mathematical post-processing algorithms, we developed an automatic workflow named Bacterial Cell Morphometry 3D (*BCM3D*) (183) to accurately segment and classify single bacterial cells in 3D dense biofilm images. The *BCM3D* workflow outperforms state-of-the-art bacterial cell segmentation approaches This work has been published (183). Details of *BCM3D* are described in Chapter 4.

## 1.5 Bacterial Cells Tracking

In addition to image biofilms with cellular/subcellular resolution and precise single cell segmentation, simultaneous multiplexed tracking of individual cells is also required to understand how biofilm growth and its functional capabilities arise from the collective actions and interactions among individual cells. However, multi-cell tracking in dense biofilms is challenging due to the following factors. First, bacterial cells of the same species have almost identical morphometry. Second, bacterial cells are closely packed within dense biofilm. Third, individual cells possess dynamic features, such as wiggling and moving, which can make cells disappear from the imaging window among frames of images collected at different time points. To minimize the impact of these issues on the tracking accuracy, conventional tracking approaches often requires high frame rate imaging (134,

184) or multicolor labeling (185) imaging. High frame rate imaging makes the sample exposure to light with high frequency. Multicolor imaging causes additional light exposure to the sample. They can both result in increased photodamage, especially for long-term time-lapse imaging. Due to the large size (e.g. 50 by 50 μm) of the field of view (FOV) that is required to image biofilms, high frame rate might be not experimentally achievable. An additional challenge following cell tracking is to determine the cell lineage.

To address the challenges associated with multi-cell tracking in crowded biofilms, we developed a bacterial cell tracking algorithm that leverages correlations among single-cell observables, i.e. cell positions, orientations, shapes, volumes and fluorescent intensities. The cell lineage is also determined by using single-cell observables, i.e. cell positions and cell volumes. This work is described in Chapter 5 and has not been published yet.

## 1.6 Single Cell Dynamics of *Shigella flexneri* Biofilms

*Shigella flexneri* is an intracellular bacterial pathogen that invades epithelial cells in the colonic mucosa and leads to bloody diarrhea (36, 186-188). The surviving and spreading of *S. flexneri* is challenged by several environmental conditions within the epithelial lining of the gut, such as host production of antimicrobial peptides, proteases, and bile salts (189). The amphipathic structure of bile salts provides detergent-like properties and results in antimicrobial activity (190, 191). Previous studies revealed that the interaction between *Shigella* species and its environment is regulated by bile salts (33).

Pope *et al.* first found that the adhesion of *S. flexneri* and *S. dysenteriae* to HeLa cells are enhanced by the presence of the secondary bile salt deoxycholate (DOC) (192). Recently, it is reported that *Shigella* spp. form the biofilms when exposure to a mixture of DOC and cholic acid (CA) (38).

The intra- and inter- cell spread of *S. flexneri* to host cells is a hot topic. The spread of *S. flexneri* is driven by actin-based motility (31, 37). *IcsA*, an outer membrane protein, is the major determinant of the actin-based motility (31, 32, 37). In addition to its role in actin-based motility, *IcsA* also acts as a host cell adhesion (31, 193). Very recently, Koseoglu *et al*. reported that *IcsA* promotes biofilm formation of *S. flexneri* in the presence of bile salts (36). Little is known about how *IcsA* contributes to the spread *S. flexneri* while also facilitates its biofilm formation. A better understanding of single cell behaviors in *S. flexneri* will help answer this question.

None of the above-mentioned studies on *S. flexneri* biofilms were performed *in vivo* with single cell resolution. Those studies only provide information of *S. flexneri* biofilms at an ensemble level, such as the total biomass and the thickness. The single cell behaviors in *S. flexneri* biofilms are still unclear. Understanding the individual cell behavior in *S. flexneri* biofilms could help develop strategies for eliminating this pathogenic strain and thus prevent its spread. In this dissertation, the workflow that enables non-invasive study of live biofilms from the single cell level is applied to investigate the dynamics events in *S. flexneri* biofilms. This work is described in Chapter 5 and has not been published yet.

## 1.7 Outline

The majority of this dissertation focuses on addressing the challenges in biofilm study by developing integrated experimental and computational technologies that enable non-invasive imaging of bacterial biofilms with subcellular resolution, accurate automatic single-cell segmentation for the experimentally acquired images, and simultaneous tracking of thousands of cells inside 3D biofilms. Chapter 2 describes how the imaging platform, LLSM is built. For the purpose of long-term imaging of live biofilms with LLSM and precise control of the growth condition for biofilms, a flow chamber, in which biofilm can grow while imaging, is required. Chapter 3 describes how the flow chamber system which is compatible with the LLSM is designed. Chapter 4 presents the automatic workflow *BCM3D* we developed for single bacterial cell segmentation from the 3D images acquired with LLSM. Based on the accurate segmentation results provided by *BCM3D*, we developed a multi-cell tracking algorithm by utilizing correlations among single-cell observables, including cell positions, orientations, shapes, volumes and fluorescent intensities. The tracking algorithm is presented in Chapter 5. The non-invasive imaging method, LLSM, the single-cell segmentation workflow, *BCM3D* and the tracking approaches were applied to study the single cell dynamics in *S. flexneri* biofilms. The results are presented in Chapter 5. Finally, the overall significance and future directions of the work are summarized in Chapter 6.

The work presented in this dissertation enables the real-time measurements of single cell behaviors in 3D dense bacterial biofilms. Then, the correlation between the spatial trajectory of each cell and the cell's gene expression and behavioral phenotype can

be established. Such information provides an integrated understanding of how bacteria coordinate gene expression and social behaviors spatially and temporally. A fundamental understanding of biofilm biology will help develop new strategies for harnessing the emergent functional capabilities of microbial populations and for removing pathogenic biofilms.

# Chapter 2: Instruments

## 2.1 Introduction

According to the scales of interest in characterizing biofilms, different technologies that can provide different scales of information should be selected to design the experiment. For example, mass spectrometry (MS) can help us to understand biofilm proteomics at the molecular level (74, 194, 195). Transcriptomics approaches, including RNAseq, microarrays, and reverse transcription quantitative PCR (RT-qPCR), are useful to explore global and localized gene expression within biofilms from the gene/enzyme level (74, 196-203). Imaging techniques, such as phase contrast and confocal microscopy, combined with flow chamber systems, provide the way to understand the structure and dynamics of biofilm at the cellular level (74, 105-131).

Phase contrast imaging systems use refraction and interference caused by structures in the specimen to create high-contrast, high-resolution images without staining (105, 110, 204). Phase contrast microscopy is useful for viewing live specimens and structures such as endospores and organelles (105, 110). Phase contrast microscopy can provide a clear differentiation of semi-transparent microorganisms with transmitted light, but the depth of view is limited to a few microns. This caveat makes it not suitable to image thick 3D biofilms. Therefore, phase contrast microscopy, the oldest and simplest type of microscope, is often used for preliminary test or as an auxiliary equipment for other advanced imaging systems.

Advances in imaging technology enables obtaining 3D images of biofilms in real time. The most widely used approach for 3D biofilm imaging is confocal scanning laser microscopy (CSLM). The first 3D images of biofilms were obtained by CSLM

approximately 25 years ago (107). CSLM is not suitable to image live biofilm for long periods of time due to the high phototoxicity to the specimen and the high photobleaching rate of fluorophores used for labeling.

In recent years, light sheet-based fluorescence excitation and imaging approaches have been developed to overcome the drawbacks of confocal-based microscopy. Here, fluorescence excitation is engineered into a thin sheet. The emission from the sample is imaged onto a camera by a lens perpendicular to the excitation light sheet (**Figure 1.2**). It is basically simple widefield imaging, but optical sectioning is accomplished with the thin light sheet to illuminate a single plane. Constructing three-dimensional images only need scanning the sample in the perpendicular dimension. Since the illuminated volume is roughly equal to the detected volume, photodamage is minimized (205, 206). The most classical approach to generate a light sheet is compressing a Gaussian beam profile by a cylindrical lens. In this case, the lateral resolution $R_l$ of the technique (i.e. parallel to the light sheet) is simply diffraction limited, which is known as Abbe's diffraction limit (207):

$$R_l = \frac{\lambda}{2*NA} \tag{2.1}$$

where λ is the wavelength of the light, NA is the numerical aperture and equals to $n{\cdot}\sin\theta$, $n$ is the refractive index of the medium the lens is in, and $\theta$ is the maximum half-angle of the cone of light entering the lens.

The axial resolution is determined by the thickness of the light sheet and the numerical aperture of the detecting lens (207):

$$R_{a\_ex} = 2 * \omega_0 \tag{2.2}$$

where $R_{a\_ex}$ is the axial resolution of the excitation path, $\omega_0$ is the beam waist.

$$R_{a\_det} = 1.78 * \frac{n*\lambda_{em}}{NA_{det}^2} \tag{2.3}$$

where $R_{a\_det}$ is the axial resolution of the detection path (207), n is the refractive index of the media, $\lambda_{em}$ is the emission wavelength, and $NA_{det}$ is the numerical aperture of the of the detection objective.

To improve the resolution of light sheet-based microscopes to the subcellular scale, many optical configurations have been developed to create thinner light sheet. Among these, lattice light sheet microscopy (LLSM) (137, 138) and field synthesis variants thereof (139), axially-swept light sheet microscopy (ASLM) (140, 141), and single-objective oblique plane light sheet microscopes (142-145) now combine subcellular resolution with fast temporal resolution and lower phototoxicity than confocal microscopy modalities. Specifically, these advanced light sheet-based microscopy approaches can operate at illumination intensities that are below the levels of cellular phototoxicity, even for notoriously light sensitive specimens, and reduce fluorophore photobleaching by 20-50 times compared to confocal microscopy, while maintaining comparable spatial and temporal resolution and SBRs (137, 138). The work described in this dissertation utilizes a home-built LLSM.

## 2.2 Phase contrast microscopy

Phase contrast microscopy has been widely used for decades, with Fritz Zernike first describing the method in 1934 (208). A major advantage of phase contrast microscopy is that it permits imaging of structural properties of live cells and does not require fluorescent labeling. Phase contrast microscopy has a major disadvantage, the inability to capture 3D images. Despite being limited by this caveat, phase contrast microscopy combined with flow chamber systems is still a direct, fast and easily-setup method to observe biofilm development from a macroscopic perspective. Therefore, before imaging bacterial biofilms with LLMS, biofilms are first cultured in a home-made flow channel and imaged on a phase contrast microscope. The purpose for these experiments includes checking the effect of the laser intensity, the components of the flow media and the flow rate of the media on the growth of biofilms, and obtaining preliminary data to estimate the growth rate of biofilms. This information is then used to optimize the experimental condition for imaging biofilms in 3D with cellular/subcellular resolution on LLMS.

### 2.2.1 Optical Path of the Phase Contrast Microscope

The phase contrast microscope used in this dissertation is part of a home-designed single-molecular microscope (**Figure 2.1**). For the phase contrast optical path, a red light-emitting diode (LED) is used as the illumination light source. The LED is installed on the illumination tower above the inverted microscope stage of the single-molecular microscope. The illumination red light is first collimated by a set of lenses. Then the illumination light

passes through an annulus ring, and result in a ring of light. It is then focused by a condenser lens onto the sample plane. The light passing through the sample will be scattered by the biological material and phase shifted by -90°. The light passing through the area surrounding the biological material will not be affected. The light then travels down through the objective lens and the tube lens. A flip mirror is installed at the focal plane of the tube lens. It allows switching the light travelling between the fluorescence emission pathway and the phase contrast pathway. The flip mirror is electronically controlled, which enables automation during imaging acquisition when switching between optical paths is required. When the mirror is flipped up, the light will travel through the phase contrast optical pathway. After the flip mirror, the light then passes through a 4f system. A phase ring is installed in the Fourier plane between the two 4f lenses (**Figure 2.1**). The light that has not been scattered by the sample will pass through the ring, and be phase shifted by +90°, while most of the scattered light will not pass through the ring and will not be affected. Finally, the camera detector (Aptina MT9P031) is positioned at the image plane. The destructive interference between the background and scattered light caused by the total phase shift of 180° will result in the sample appearing darker than the light background, when viewed on the camera.

The fluorescent channels will be only used to check the effect of laser intensity on the growth of biofilms and the intensity of the fluorescence signal for the fluorescently labelled biofilm sample, but not to image biofilms. The configuration of our microscope enables us to shine 405, 488, 514 and 561 nm lasers on the biofilm sample. The details of the fluorescent optical paths are omitted here.

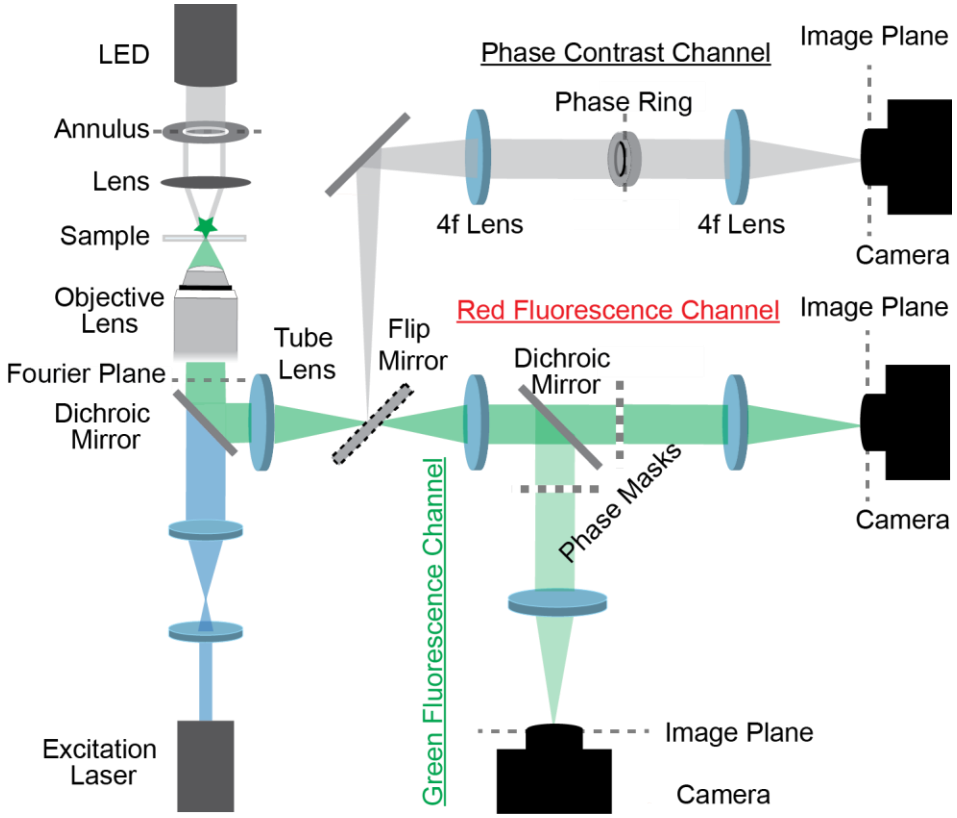


**Figure 2.1** Optical path of single-molecule microscope containing a phase contrast channel. Adapted from (209). Reprinted with permission. The red LED is used as the illumination light source for the phase contrast optical path. A motorized 'flip-mirror' is used to switch between the fluorescence (red) and phase contrast (grey) optical pathways. A dichroic mirror splits the fluorescence pathway into a 'red' and 'green' fluorescence channels. The excitation lasers, LED, 'flip-mirror' and camera detectors are controlled remotely with a program written in Matlab.

### 2.2.2 Synchronization of the Phase Contrast Microscope

LED and camera:

When the LED receives a high-level digital signal, it turns on. Then, the API controlling the camera is called to allow the camera to begin collecting images. After finishing saving images, a low-level digital signal is sent to the LED to turn it off. Iteration of these two steps allows one to acquire time-lapse data. Time gap between iterations can be set as required.

Translational stages, LED and camera:

Desired position information is sent to the translational stages by calling their APIs. After the translational stages move to the desired position, the LED is turned on by a high-level digital signal. Then, the API controlling the camera is called to let the camera begin collecting images. After finishing saving images, a low-level digital signal is sent to the LED to turn it off. Iteration of these three steps allows to acquire time-lapse data. Time gap can be set as required.

Laser, LED and camera:

Laser illumination is controlled by the mechanical shutter in the optical path. The shutter is open by a high-level digital signal, which means the laser illuminates on the sample. After illuminating the laser for the time the user defined, the laser will be blocked by turning off the shutter with a low-level digital signal. Then, the LED is turned on by a high-level digital signal. Following that, the API controlling the camera is called to let the

camera begins collecting images. After finishing saving images, a low-level digital signal is sent to LED to turn it off. Iteration of these three steps allows to acquire time-lapse data. Time gap can be set as required.

### 2.2.3 Data Acquisition of the Phase Contrast Microscope

A home-made microscope has several benefits compared to commercial ones. For example, there is no requirement for external maintenance, therefore a custom microscope can save the cost in long term. The most attractive advantage is the full flexibility in terms of its design and use. For example, the home-written data acquisition program provides the ability to adjust the procedure for data collection to satisfy specific experimental requirements. We wrote the program to control the phase contrast microscope by ourselves.

The data acquisition program is developed with Matlab and a NI DAQ card (NI PCIe-6351, X Series). The functionalities of the data acquisition program includes collecting time-lapse data at a fixed field of view (Sequence), collecting time-lapse data at multiple regions of the sample at different z position (Z Scan plus Grid Scan), collecting time-lapse data for sample exposure to laser (scan with laser on) (**Figure 2.2**). Each functionality is designed for specific experiments. Collecting time-lapse data in a fixed field of view is for general experiments to observe the growth of a bacterial biofilm. Collecting time-lapse data at multiple regions of the sample at different z positions can provide spatial information of biofilm growth. Collecting time-lapse data for sample

exposure to laser are especially useful for designing experiments to check the impact of light on the growth of biofilms.

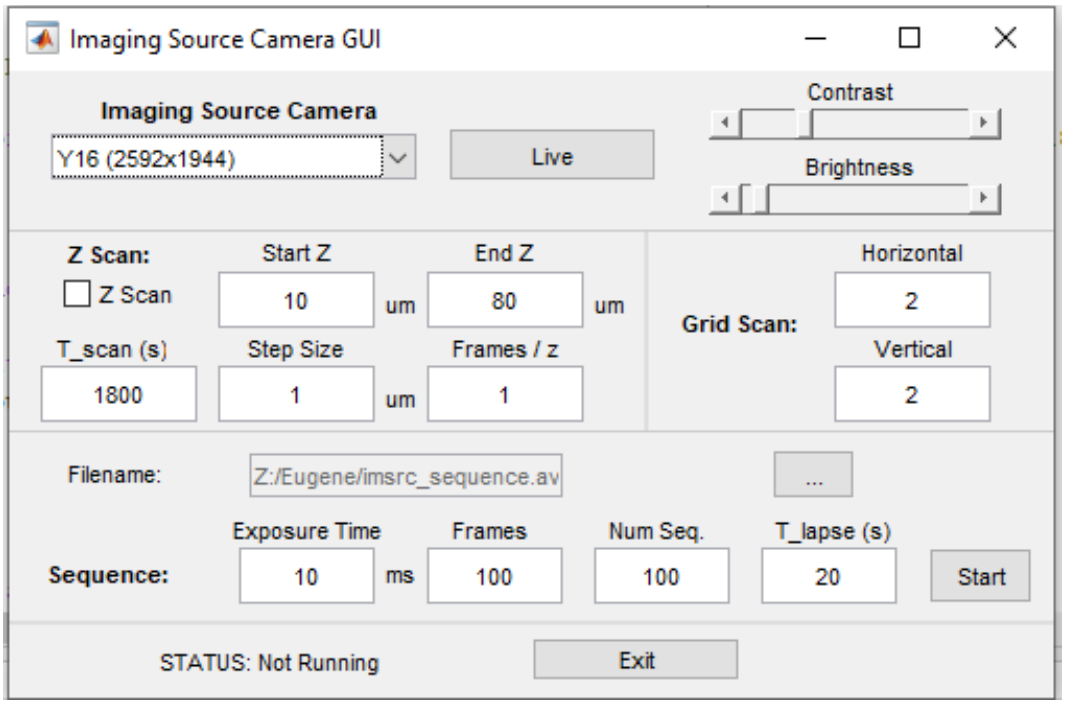


**Figure 2.2** The graphical user interface (GUI) of the data acquisition program for the phase contrast microscope. **Imaging Source Camera**: set the size of the image. Live: online monitor the sample. **Z scan**: collecting images by scanning the sample in the z direction. Frames/z is used to set the number of frames collected at each z position. T_scan is used to set the time between z scans. **Grid scan**: collecting images by scanning the sample in the x and y direction. Horizontal and Vertical determines how many field of views will be imaged in x and y direction, respectively. **Sequence**: collecting time-lapse data at a fixed field of view. Exposure time sets the exposure time for all data acquisition mode. Frames sets how many frames of image will be collected at one time point. Num_seq sets how many time points data will be collected. T_lapse is used to set the time between time points.

## 2.3 Lattice Light Sheet Microscopy (LLSM)

Betzig lab developed LLSM in 2014 (137). Chen *et al*. in Betzig lab reported the detailed design of LLSM (137). In this section, I will briefly introduce several basic concepts in LLSM, such as Bessel beam (non-diffracting beam), 2D optical lattice, the generation of lattice light sheet, device basics and synchronization.

### 2.3.1 Bessel Beam

Assuming a beam propagates in the y direction with an unchanged profile in the xz plane, it is defined as a non-diffracting beam. A Bessel beam is a non-diffracting beam whose intensity profile in its cross-section can be described by the circularly symmetric Bessel function (**Figure 2.3**) (137, 210-214). Bessel beams are good candidates to create non-diffracting light sheet.

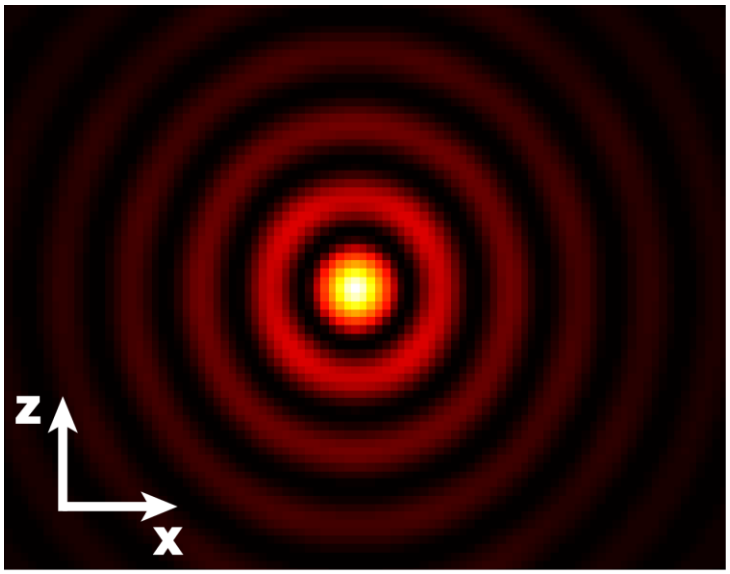


**Figure 2.3** The intensity profile of the cross-section (xz plane) of a simulated Bessel beam propagating in y direction.

### 2.3.2 Two-dimensional (2D) Optical Lattice

A 2D optical lattice is a non-diffracting beam whose intensity profile in the cross section has the symmetry of a 2D *Bravias lattice* (137, 215, 216). 2D optical lattices are also good candidates to create non-diffracting light sheet. But, they cannot be directly used, because they propagate in the whole 3D space (137).

### 2.3.3 Generating the Desired Lattice Light Sheet

Ideal Bessel beams and 2D optical lattices are good candidates to create thin, non-diffracting light sheets, however, there are obstacles to use them in light sheet microscopy. For example, the way to generate ideal Bessel beams and 2D optical lattices is by confining the incident light beam to an infinitesimally thin ring at the rear pupil of a lens (137). Obviously, it is not possible to make an infinitesimally thin ring in reality. In practice, the infinitesimally thin ring is replaced with an annulus that has a particular width. In this case, the output beam is not an ideal Bessel beam or 2D optical lattice, but it still keeps the diffracting feature over a distance determined by the width of the annulus (137).

In LLSM, the lattice light sheet pattern is generated by using a binary ferroelectric spatial light modulator (SLM). The SLM pattern is finally imaged at the sample to create the thin light sheet because it is positioned in a conjugated plane to the front focal plane of the excitation objective lens. An annular mask with appropriate width is positioned conjugate to the rear pupil plane of the excitation objective lens. The annular mask is to confine the beam and filter out undesired diffracted light. Chen *et al*. reported three different ways to derive desired lattice light sheets and provided the procedure to generate

the corresponding SLM patterns (137). They simulated the optical path from the SLM to the imaging plane is in Matlab (137). By simulation, the wavelength of the beam, the size of the annulus and the SLM pattern can be easily adjusted. The combination of the annulus and the binary SLM patterns can generate the light sheet with desired properties, such as the length and thickness of the light sheet, and the overall resolution in z (137). Here are two examples of generating lattice light sheet by following their procedure. **Figure 2.4** shows the procedure to simulate a hexagonal lattice pattern by starting with an ideal 2D optical lattice. **Figure 2.5** shows the procedure to simulate a square lattice pattern by positioning a linear array of Bessel-Gauss Beams.

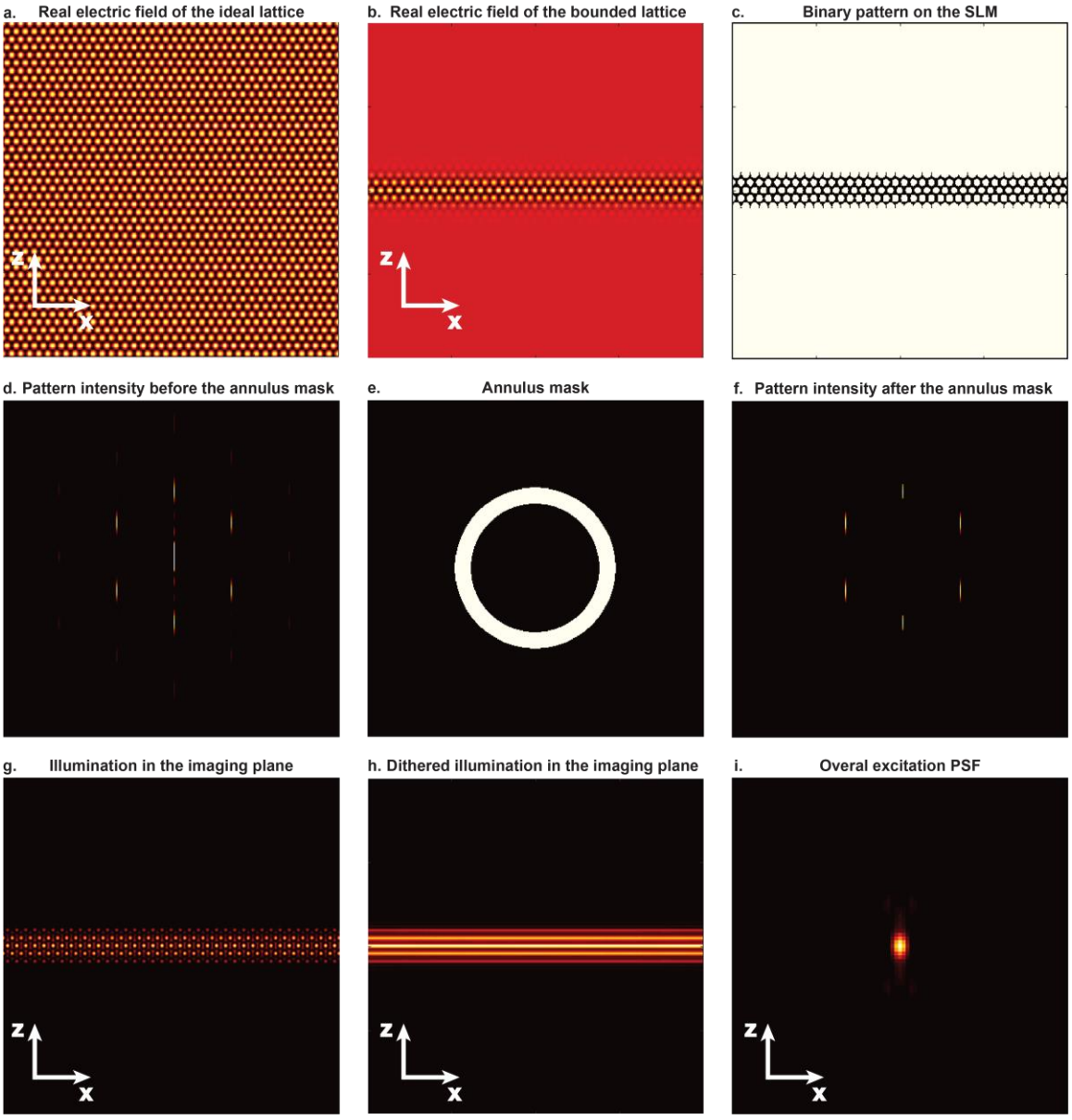


**Figure 2.4** Steps in the simulation for the generation of the SLM pattern for a desired lattice light sheet. Adapted from (137), reprinted with permission from AAAS. (a) Intensity profile of the ideal 2D optical lattice which will be used to generate the desired lattice light sheet. (b) Bounded ideal 2D optical lattice shown in panel a. (c) SLM pattern obtained by binarizing the bounded ideal 2D optical lattice shown in panel b. (d) Illumination pattern before shooting on the annulus mask. It is obtained by the Fourier transform of the diffraction pattern produced by the SLM. (e) Simulated annulus mask. The inner and outer

NA of the annulus mask is 0.44 and 0.55, respectively. (f) Beam pattern immediately after or on the annulus mask. (g) Intensity profile of the cross-section of the lattice light sheet without dithering. (h) Intensity profile of the cross-section of the lattice light sheet dithered in the x direction. (i) Overall PSF of LLSM under dithering running mode.

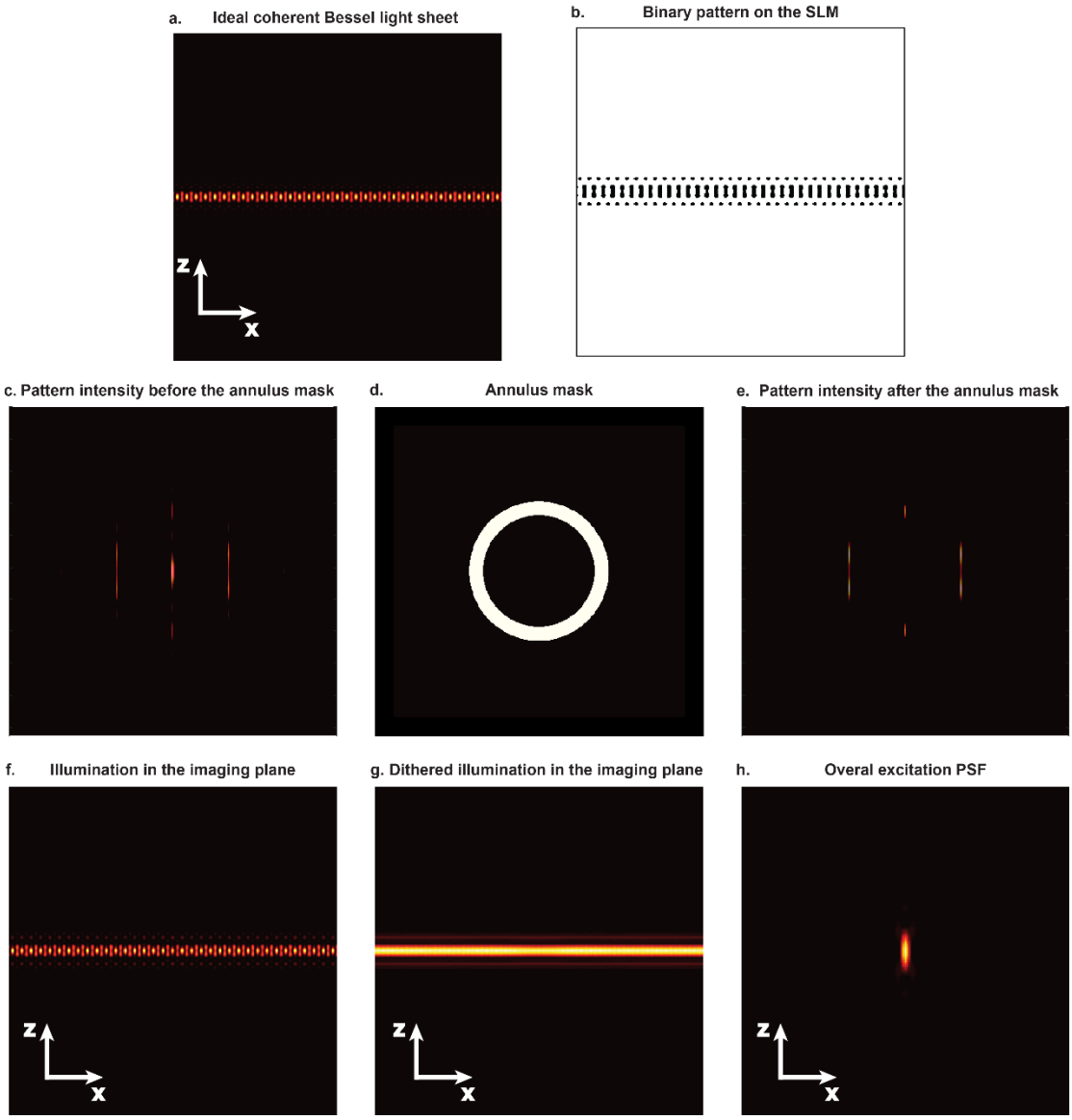


**Figure 2.5** Steps in the simulation for the generation of the SLM pattern for a desired lattice light sheet. Adapted from (137), reprinted with permission from AAAS. (a) The intensity of the ideal coherent Bessel light sheet. (b) SLM pattern obtained by binarizing the ideal coherent Bessel light sheet shown in panel a. (c) Illumination pattern before shooting on the annulus mask. It is obtained by the Fourier transform of the diffraction pattern produced by the SLM. (d) Simulated annulus mask. The inner and outer NA of the annulus mask is 0.44 and 0.55, respectively. (e) Beam pattern immediately after or on the annulus mask. (f) Intensity profile of the cross-section of the lattice light sheet without

dithering. (g) Intensity profile of the cross-section of the lattice light sheet dithered in the x direction. (h) Overall PSF of LLSM under dithering running mode.

### 2.3.4 Detailed Designs of LLMS

**Lattice light sheet illumination path:**

LLSM is designed by Betzig lab (137). We adapted the original design by utilizing a new type SLM, different types of translation stages for the sample platform, different way to hold the sample platform and different way to position the main camera. The optical system of LLMS is shown in **Figure 2.6**. The microscope contains four lasers with different wavelengths in the excitation pathway. A 488 nm laser (1000 mW, Genesis, MX488-1000 STM), a 560 nm laser (1000 mW, MPB Communications, 2RU-VFL-P-1000-560-B1R), and a 641 nm laser (1000 mW, MPB Communications, 2RU-VFL-P-1000-647-B1R) is used for excitation of fluorescent emitters, while a 405 nm laser (250mW, Coherent OBIS, OBIS 405nm LX) is used to activate photo-activatable fluorescent emitters, such as PAmCherry1 (activation with 405 nm laser and subsequent excitation with 561 nm laser). The configuration described above provides the capability for multi-color imaging.

The beam is first expanded to by two lenses (50 mm FL/25.4 mm diameter, Thorlabs, 200 mm FL/25.4 mm diameter Thorlabs). The diameter of the resulting beam is about 4.0 mm. All excitation laser lines are then combined into the same excitation pathway using a set of dichroic mirrors. The beam then passes through an acousto-optic tunable filter (AA Quanta Tech, Optoelectronic AOTF AOTFnC-400.650-TN). A flip mirror is

installed behind the AOTF, which could switch the beam from lattice light sheet channel (flip up) to epi fluorescence channel (flip down). Following the flip mirror in the lattice light sheet channel, a pair of cylindrical lens (25 mm FL/12.5 mm diameter, Edmund NT68-160 and 250 mm FL/25.4 mm diameter, Thorlabs, ACY254-250-A) are positioned to expand the beam to expand the beam in x dimension. The expanded beam then shoots on the lattice light sheet pattern on the SLM. The SLM contains 2048 x 1536 ferroelectric-liquid-crystal pixels (Forth Dimension, QXGA-3DM). In front of the SLM, there is a polarizing beam splitter cube (Newport, 10FC16PB.3) and a half-wave-plate (Bolder Vision Optik, BVO AHWP3) to change the phase of the beam (217). The diffracted light from the SLM is then focused by a 500 mm focal length lens (500 mm FL/40 mm diameter, Edmund 49-283) onto an annular mask (Photo Sciences Inc.). The beam is then shrunk by 0.75 times with relay lenses (80 mm FL/12.5 mm diameter, Edmund NT47-670, 60 mm FL/12.5 mm diameter, Edmund NT47-668). After demagnification, the beam is conjugated to a fast scanning system contains two 3 mm galvos (Cambridge Technology, 6215H) and two achromatic relay lenses (25 mm FL/12.5 mm diameter, Edmund NT47-662) in a 4f arrangement. The fast scanning system enables scanning along the x and z directions on the sample. Following this, the beam pattern is then magnified by 3.2 times with relay lenses (125 mm FL/25 mm diameter, Edmund NT49-361, 400 mm FL/25 mm diameter, Edmund 47-650). The beam pattern finally illuminates the back focal plane of the excitation objective (Special Optics, 0.65 NA, 3.74 mm WD). The SLM conjugates to the focal plane of the excitation objective lens. The annular mask conjugates to galvo mirrors, and the back pupil of the excitation objective.

The lattice light sheet is finally generated after the beam pattern travels through the excitation objective lens. The detection objective lens (Nikon, CFI Apo LWD 25XW, 1.1 NA, 2 mm WD) is mounted orthogonal to the excitation objective. The focal plane of the detection objective overlaps with the excitation plane. The detection objective is positioned on a piezo stage (Physik Instrumente, P-621.1CD). Keeping the focal plane of the detection objective coincident with the lattice light sheet illumination in the z-galvo scanning image acquisition mode is achieved with this piezo stage. The fluorescence signal then passes through a 500 mm tube lens (500 mm FL/25 mm diameter, Edmund 47-651). It is then expanded by a 4f system. After travelling through an emission filter (FF01-446/523/600/677-25, Semrock). It is finally collected by a scientific Complimentary Metal-Oxide Semiconductor (sCMOS) camera (Hamamatsu, Orca Flash 4.0 v2 sCMOS). To help the alignment of the optical path, inspection cameras (Imaging Source, DMK 33UP1300), are also installed at suitable positions.

**Epi illumination path:**

When the flip mirror behind the AOTF is flipped down, the beam will pass through the epi illumination path. The beam is expanded by a factor of 3.75 with two lenses (20 mm FL/12.24 mm diameter, Thorlabs C240TME-A, 75 mm FL/12.5 mm diameter Edmund 47-661). Then, it passes through a 150 FL/12.5 mm diameter lens. Following this lens, a 90/10 beam splitter is installed. 90% of the beam passes through the beam splitter and then an oil immersion objective (Olympus LUMPLFLN 40XW). The focal plane of this

objective is coincident with lattice light sheet illumination objective and the detection objective. The excitation objective of the epi illumination path is installed on a xyz translation stage (Newport, 462-XZ-M), which provides both the convenience for alignment and the flexibility for scanning large fields of view. A long pass filter (FF01-496/LP-25, Semrock) and a lens (100mm FL 25mm diameter Edmund NT47-641) are installed in the reflected path of the 90/10 beam splitter. Following this lens, an inspection camera (Imaging Source, DMK 33UP1300) is installed in planes conjugate to the sample plane, which will help the alignment for the epi illumination path.

The sample platform comprises a piezo stage (Mad City Labs, NanoOP100HS) which is mounted on a xyz micro-stage (Mad City Labs, MCL-MMP3). The piezo stage can position the sample with nanometer precision in the sample scanning image acquisition mode. The micro-stage has two functionalities. First, it is used as a coarse stage to find good field of views for imaging. Second, it is used to acquire tiles of datasets for objects that are larger than one field of view.

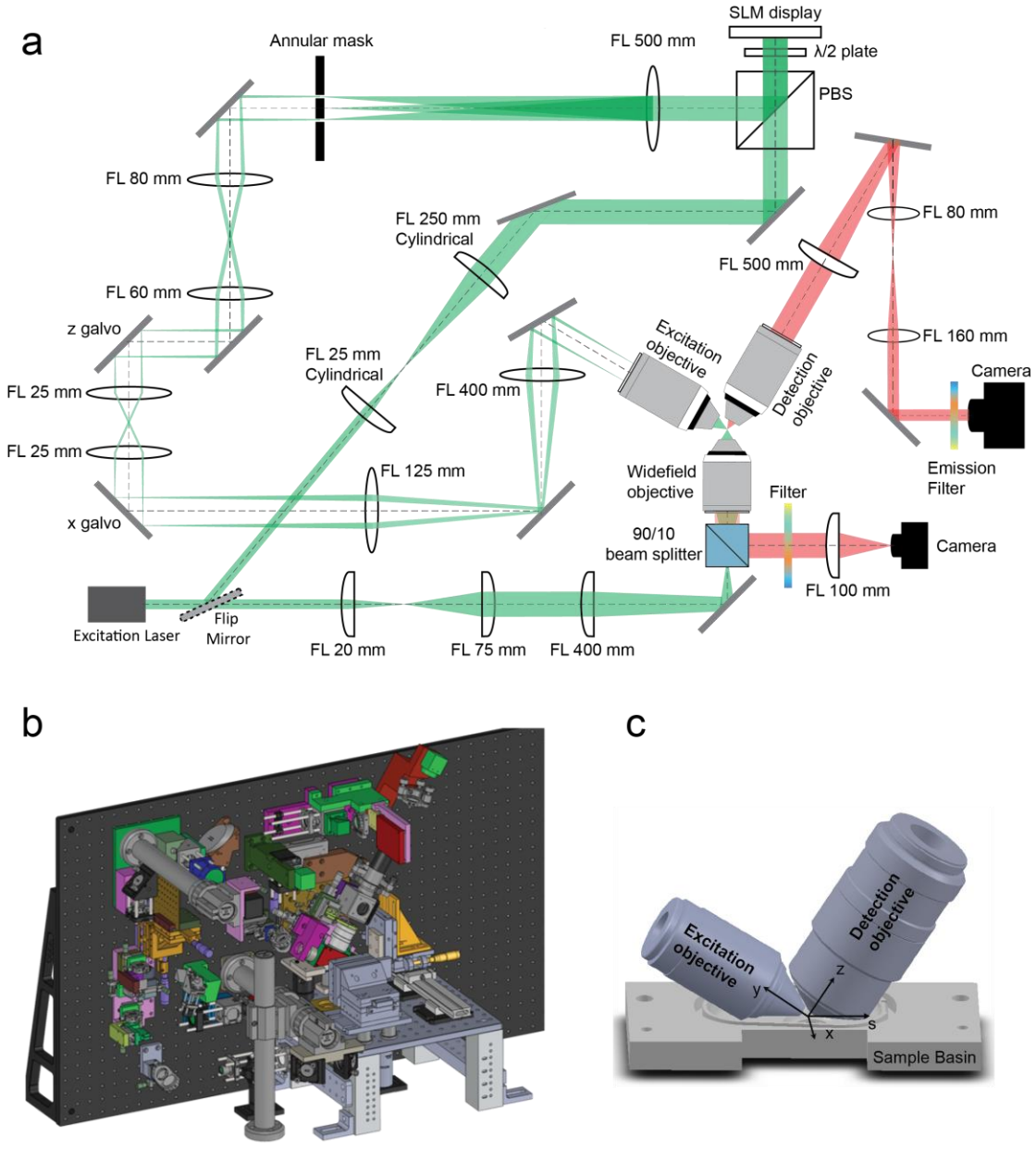


**Figure 2.6** (a) Optical path of LLSM. Adapted from (137) , reprinted with permission from AAAS. FL represents focal length. PBS indicates polarization beam splitter. (b) 3D model (SolidWorks 2018, Dassault Systèmes) of LLSM. A 24 x 48 inch breadboard is vertically mounted on an optical table. The sample platform, including the piezo stage and a 3D translational stage are installed on a home designed tower mounted on the optical table. (c) Model showing the orthogonally mounted excitation and detection objectives.

They are dipped in a basin filled with media or water. The light sheet propagates in the y dimension and is dithered in the x dimension. The s direction represents the sample scanning direction.

### 2.3.5 Synchronization of LLMS

To acquire images with LLMS, the actions of following devices must be synchronized: SLM, AOTF, x-galvo, z-galvo, sample piezo stage, detection objective piezo stage and camera.

#### 2.3.5.1 Devices Basics

**SLM**

The SLM is conjugate to the sample plane, so that the lattice pattern on the SLM is imaged within the sample plane. The lattice patterns are saved as binary images (**Figure 2.7**, inserted picture) and displayed on SLM. A user-defined "Running Order" stored in SLM controls how to display images of lattice patterns. The "Running Order" is made by utilizing the software MetroCon (V3.3, Forth Dimension). The running order is composed by binary images and time sequences. The binary images are what to display and the time sequences determine how long an image should be displayed. When an image is displayed on SLM, the incident light will be reflected with its polarization state changed by the pixel arrays of the image (Forth Dimension, manual for QXGA-3DM). And finally, the light can leave the system (**Figure 2.7**, green path). Indeed, the ferroelectric SLM device displays an image as both positive and negative images to make each pixel stay in each state with

the same time (137). Comparing to the exposure time for image acquisition with the magnitude of ms, the invert time with the magnitude of μs is ignorable. Due to these facts and in order to simplify the discussion about the synchronization of the microscope, only the term 'image' will be used to represent the positive and negative images displayed on the SLM in the following context.

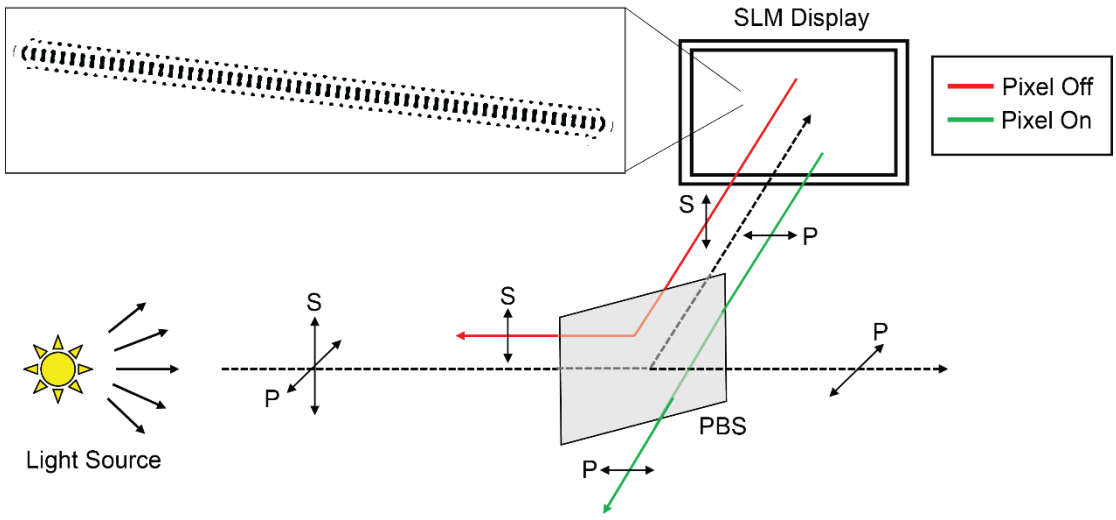


**Figure 2.7** The working mechanism of SLM. Adapted from the manual of SLM (Forth Dimension, QXGA-3DM). PBS, polarization beam splitter. The inserted picture is the binary picture displayed on the SLM display. When the pixel on the SLM is on, the polarization of the light (green path) reflected by these pixels will be changed. And then the reflected light will leave the system and pass through the optical path of the LLSM. However, when the pixel is off, the polarization of the reflected light (red path) will not change and then the light will stay in the system, but not pass through the optical path of the LLSM.

When different patterns need to be displayed on the SLM during imaging, the SLM requires the time to reload images. For example, in the experiment of dual color imaging, different lattice light sheet patterns for different channels, such as 488 and 560 nm, might be required to be displayed in sequence on the SLM. When reloading images, SLM cannot be used for imaging. Since the reloading time is relatively long, it must be taken into account when imaging. However, there is no way to directly know the state of the SLM after it starts running. The single digital output hardware line (LED Enable) from the SLM is the only information that can be used to externally infer its state (137). The LED Enable is set to high when the SLM is in the state of displaying an image (**Figure 2.8**). The LED Enable is set to low when the SLM is reloading images to display.

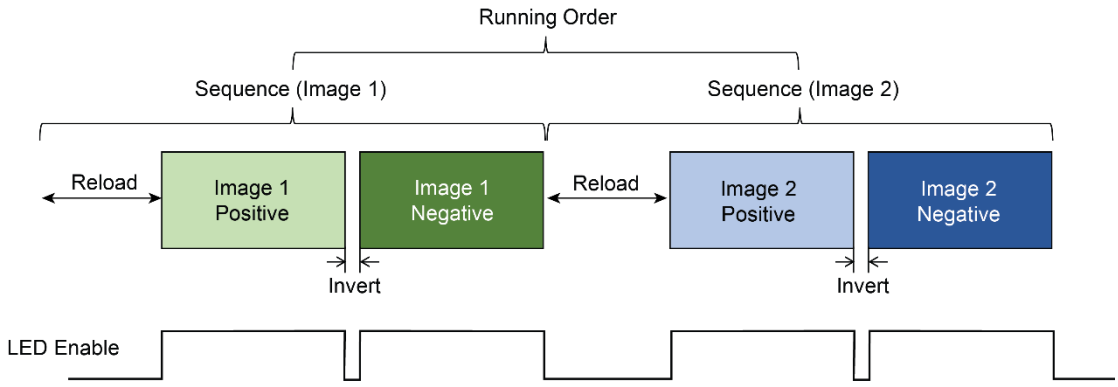


**Figure 2.8** The SLM running order and the LED Enable line. Adapted from (137) , reprinted with permission from AAAS. When the SLM is displaying an image, the LED Enable line will set high, otherwise low.

### AOTF

AOTF is the device that can modulate a laser beam by using the acousto-optic interaction (218-221). In the design of LLSM, AOTF is used to switch among different laser channels and set required illumination powers. AOTF runs in external trigger mode. It is synchronized to the LED Enable signal of the SLM. When the SLM is displaying images, AOTF will turn on to let the light pass through. When the SLM is in other states, such as reloading images, AOTF will turn off to block the light.

### x-galvo and z-galvo

The galvo system consists of a galvanometer-based scanning motor with an optical mirror mounted on the shaft. The incident light shoots on the optical mirror. The high-speed scanning of the reflected light is accomplished by quickly flipping the shaft. The x-galvo is responsible for generating a uniform light sheet by dithering the Bessel beam arrays in the x direction (**Figure 2.9**). Usually, scanning the sample is achieved by moving the sample across this uniform light sheet. But, the position of the sample must be fixed for some experiments. In this case, the scanning is achieved by moving the uniform light sheet across the sample with the z-galvo.

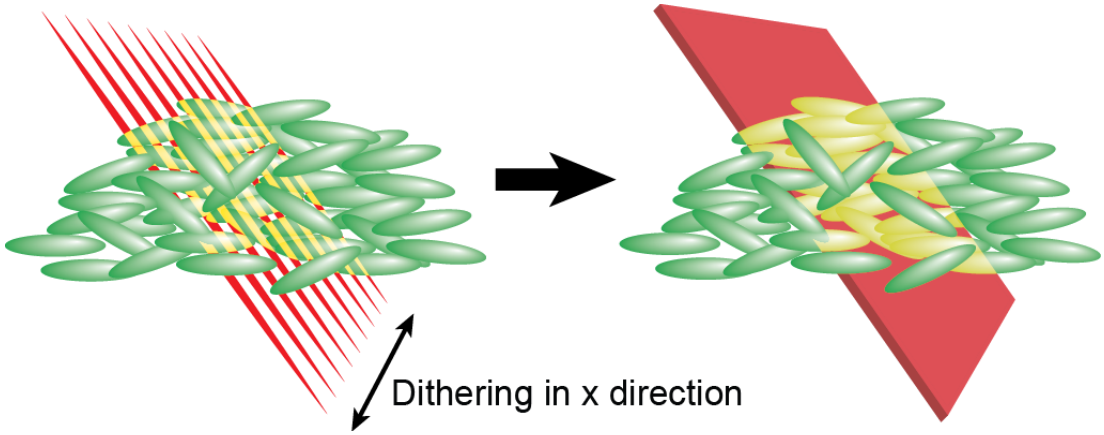


**Figure 2.9** Generation of the uniform light sheet by dithering the Bessel-Gauss beam arrays in the x direction with the x-galvo.

**Sample piezo stage and objective piezo stage**

The piezo stages have the range of motion as 100 µm. The resolution of the piezo stage is 0.2 nm. The piezo stage is controlled with the analog voltage signal, which is configured as 0-10 V corresponding to 0-100 µm. The sample piezo stage is in charge of shifting the sample along the sample scanning direction. The objective piezo stage is responsible for moving the detection objective along its optical axis.

### 2.3.5.2 Synchronization

#### SLM - the time source for LLSM

Once the SLM starts running, it should not be stopped during the experiment. Stopping the SLM running and then restarting it will require reloading the running order, which will take several seconds to finish. This is not acceptable for high speed image acquisition. That also means external controlling SLM is not available for high speed applications. That is why SLM runs by itself and all other devices are synchronized to it (137).

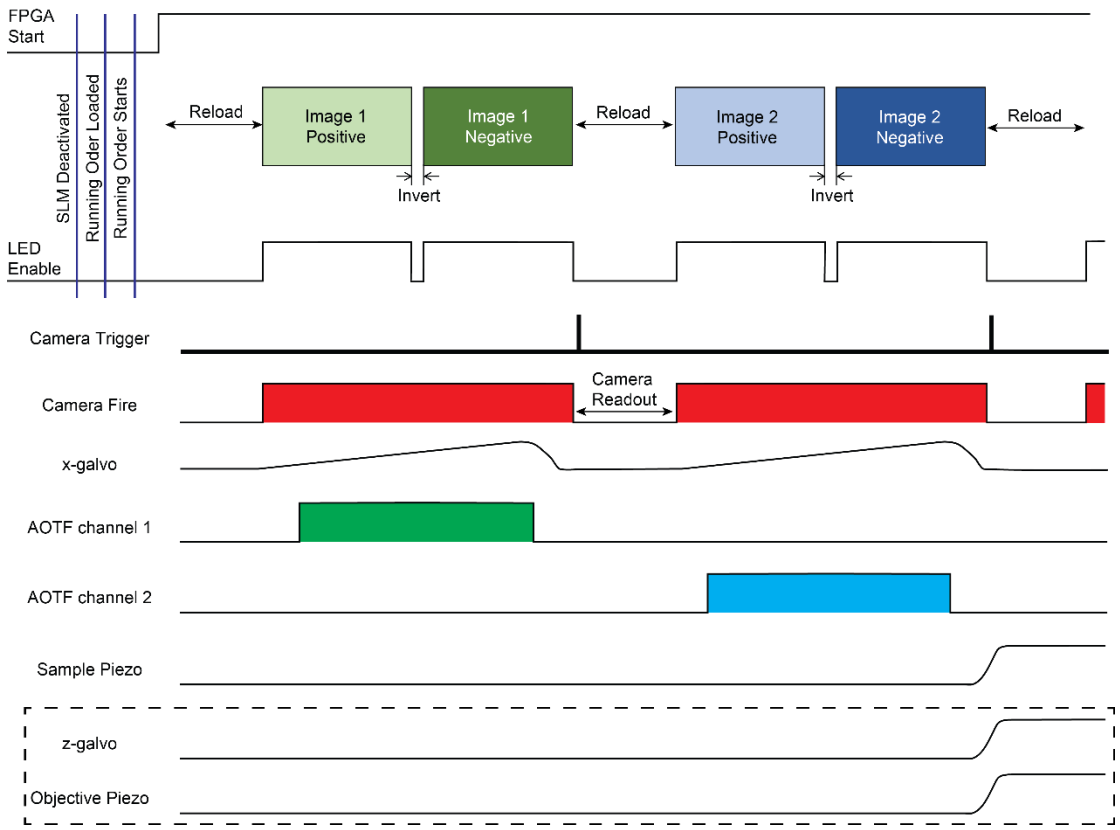


**Figure 2.10** SLM synchronization during the image acquisition in two colors with the dithered mode. Adapted from (137), reprinted with permission from AAAS.

Controlling signals for all devices are synchronized to the SLM LED Enable line. After acquiring images from each channel, scanning the sample can be achieved by either moving the sample with the sample piezo or moving the excitation illumination plane with z-galvo and detection objective piezo (as shown in the dash rectangular).

To use the SLM as the time source, the first step is to obtain the state of the SLM by reading the LED Enable line. However, this approach can only tell when SLM starts and ends displaying images, but not which image is currently being displayed. Since images stored in the user-defined running order are known before SLM starts running, the currently displayed image can be inferred by counting the number of LED Enable pulses from a particular starting time point (137) (**Figure 2.10**). And then, the SLM pattern, the AOTF frequency, power and blanking, the camera exposure, the x-galvo, the z-galvo, the sample piezo and the objective piezo can be all synchronized according to the SLM state.

Signals to control all devices are generated and sent by a Field Programmable Gate Arrays (FPGA) card (PCIe-7852R, National Instruments). Based on preloaded timing information, the FPGA card triggers the camera to make sure that the camera only collects image when the SLM is displaying the lattice light sheet pattern (137). According to this timing information, the FPGA card also generates signals to synchronize the x-galvo, z-galvo, objective-piezo, sample-piezo, AOTF frequency and AOTF power (**Figure 2.10**). All devices in LLSM are synchronized to the internal running clock of the SLM.

### 2.3.6 Calibration and Data Acquisition

#### 2.3.6.1 Data acquisition Setups and Running Modes

The data acquisition program was developed with Laboratory Virtual Instrument Engineering Workbench (LabVIEW, National Instruments). The LLMS has several different running modes with different setups. Running modes used to image bacterial biofilms in this thesis include Continuous Scan, Z-stack, X-Z PSF, Autofocus bead and Script Running.

**Continuous Scan:**

Continuously imaging the selected field of view. This mode is often used for calibration and searching for a region of interest.

**Z-stack:**

Scanning the sample to acquire 3D image stacks. There are two scanning types, Sample piezo scan and Z-galvo piezo scan. Sample piezo scan means the excitation light sheet is fixed and scanning is achieved by translating the specimen with a piezo stage. Z-galvo piezo scan means the sample is fixed and scanning is achieved by translating the excitation light sheet with the z-galvo. Moving the illumination plane will make it out of the focal plane of the detection objective. To compensate for the out-of-focus, the detection objective is shifted with a piezo stage along its optical axis.

**Autofocus bead:**

This running mode is used to precisely set the focal plane of the detection objective to be coincident with lattice light sheet illumination pattern with a fluorescence bead as the probe. It is a combination of Z-galvo scan and piezo (for the detection objective) scan.

**X-Z PSF:**

This running mode obtains a mapping of the xz Point Spread Function (PSF). It is accomplished by putting a single fluorescent bead in focus, locking the Z piezo for the detection objective and then moving the laser beam around using the X and Z galvos. The beam profile is finally mapped out. This running mode is used to check the quality of the selected lattice pattern on the sample plane.

**Script Running:**

Automatically collect multiple datasets at different time points and different regions of the specimen with a LabVIEW script. This running mode is particularly useful for the following two scenarios. First, collecting long term time-lapse data of biofilms. Second, imaging objects that are larger than the max field of view of the microscope by small tiles.

### 2.3.6.2 Calibration of LLMS

The microscope needs to be calibrated before image acquisition for each experiment. The calibration includes three steps: optimizing the lattice light sheet illumination pattern, autofocusing and correcting the spherical aberration induced by refractive index mismatch between the media in the sample basin and the objective lens.

**Optimize the lattice light sheet illumination pattern:**

The purpose of this calibration step is to put the illumination pattern to the center of the camera chip and make the pattern as thin as possible. In order to observe the illumination pattern, the sample basin is filled with fluorescein (0.02 mg/mL). The single Bessel beam is selected and the microscope runs in the 'continuous mode' with an imaging field of view of 128 by 128 pixels. The cross section of the illumination pattern in the xy plane is imaged on the camera (**Figure 2.11a**). Two regions are selected on each end of the pattern and the intensity profile along the x dimension is calculated (**Figure 2.11b**). Sharp and narrow intensity profiles are obtained by gently adjusting the position of the detection objective (**Figure 2.11a**), which means the thinnest illumination pattern. Adjusting the position of the excitation objective can move the entire pattern along the y direction. Adjusting the angle of a mirror at the back pupil of the excitation objective can move the pattern along the y direction and also change the pattern's orientation. Based on these operations, we can finally make two peaks overlapping at x = 64 (**Figure 2.11b**), which means the illumination pattern is even and locates at the center of the camera chip.

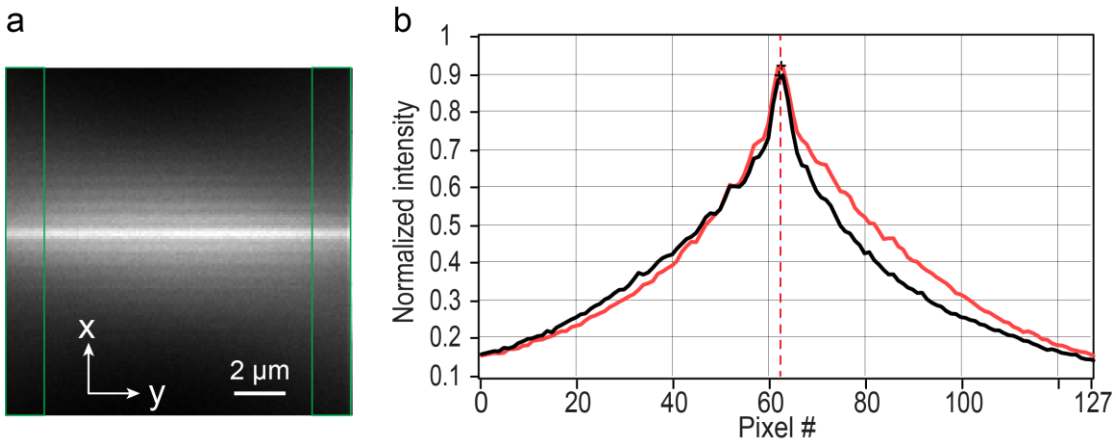


**Figure 2.11** (a) An image of 128 by 128 pixels for calibration the light sheet pattern. (b) The intensity profile of the light sheet pattern in the two selected regions along the x dimension. When two peaks of each curve are sharp and overlaps at pixel 64 (indicated by the red dash line), the light sheet is in the best condition.

**Autofocus:**

To precisely set the focal plane of the detection objective to be coincident with the lattice light sheet illumination pattern, autofocus calibration is run. 200 nm fluorescence beads coated on round glass coverslip (diameter: 5 mm, Warner Instruments) are used as the sample. The autofocus-bead running mode is selected for the microscope. The autofocus includes two steps. First, the sample, fluorescent bead, is fixed and scanned by moving the light sheet illumination along the optical axis of the detection objective for a range of 8 um in 100 steps. This is accomplished by scanning with the z-galvo. Then, the peak intensity of the bead's image is calculated and plotted along the scanning dimension (**Figure 2.12**). The precise position of the center of the fluorescent bead is read from the

curve of the intensity profile. And the light sheet illumination is positioned to the central plane of the fluorescent bead. Second, the sample is fixed and scanned by moving the detection objective along its optical axis with the light sheet illumination also fixed. The range of the scanning is 10 um in 100 steps. Then, the peak intensity of the bead's image is calculated and plotted along the scanning dimension (**Figure 2.12**). The precise position of the focal plane of the detection objective is read out from this figure. Finally, the offset between the position of the illumination plane and the focal plane of the detection objective can be calculated. The offset is added to the position of light sheet illumination plane to make it precisely coincident with the focal plane of the detection objective.

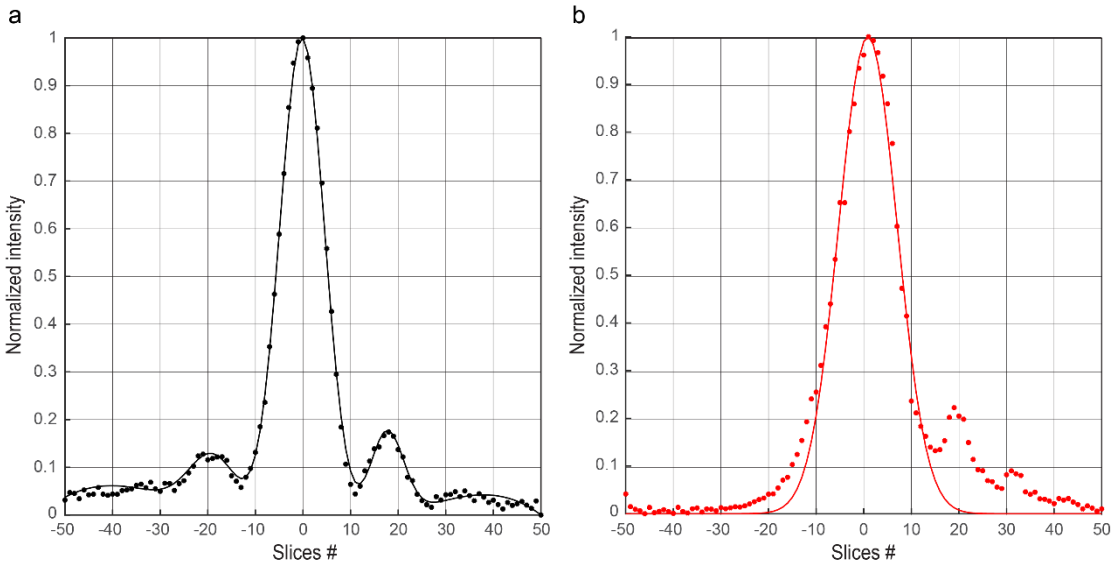


**Figure 2.12** (a) The peak intensity profile of a fluorescent bead under z-galvo scanning. The displacement between adjacent slices is 0.08 µm. The maximum value appears at slice 0 which the original position of the light sheet. (b) The peak intensity profile of a fluorescent bead under piezo scanning. The maximum value appears at slice 1. Therefore, an offset of 0.08 µm will be added to the position of the light sheet illumination plane.

**Correct the spherical aberration:**

To keep biofilms alive when directly imaging them with LLSM, the sample basin must be filled with different growth media, such as LB, TSB, M9 and etc., for different bacterial strains. The refractive index of the growth media are different from water, while that of the objective lens matches with water. Spherical aberrations are induced by the mismatch of refractive index between the growth media and the objective lens. The detection PSF is substantially deformed by the refractive index mismatch (**Figure 2.13 b**). To achieve maximum image quality, this aberration must be corrected. The collar on the

detection objective allows for adjustment of the positioning of the central lens group within the objective and provides a way to correct the refractive index mismatch aberration. By adjusting the position of the collar and observing the change of the detection PSF, the aberration can be corrected (**Figure 2.13c**). Herein, it is worth to notice that when the refractive mismatch is too large, even setting the collar to its limit position cannot completely eliminate the aberration. In this case, the collar will be set at the position that gives the best detection PSF.

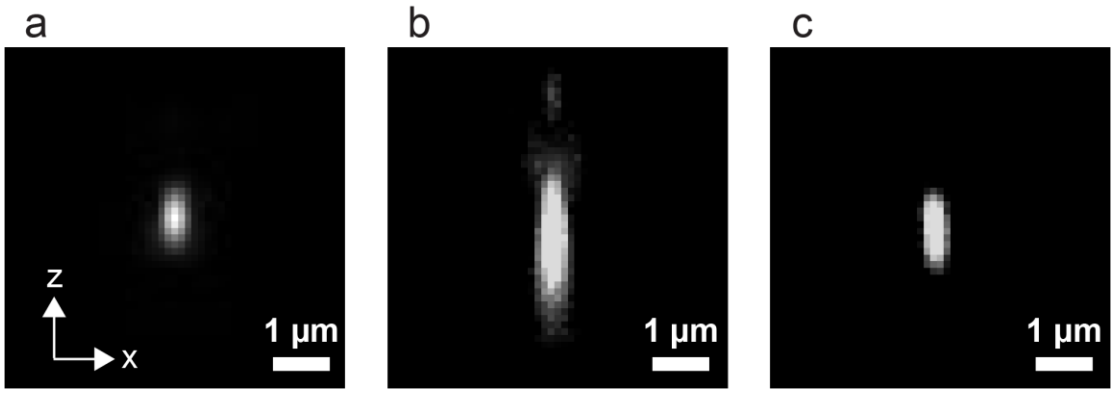


**Figure 2.13** (a) Ideal xz PSF acquired with a fluorescent bead in water. (b) xz PSF with aberration caused by the mismatch of refractive index between the growth media and the objective lens. (c) xz PSF after correction. The xz PSF is chosen as the example, because the aberration affects the axial PSF more substantially than the lateral PSF.

In this step, since the positioning of the central lens group within the detection objective is adjusted, the position of the focal plane might change. Therefore, autofocus is required, again. By iterating autofocus and spherical aberration correction several times, the LLSM achieves its best imaging condition and can be applied to acquire images.

### 2.3.7 Sample Preparation and Imaging

Bacterial strains imaged in this thesis include, *Escherichia coli* K12, *Myxococcus xanthus* LS3908, *Shewanella oneidensis* MR-1 and *Shigella flexneri*.

#### 2.3.7.1 Imaging with Phase Contrast Microscope

As the preliminary experiment, all bacterial strains imaged with the phase contrast microscope follows the similar procedure. Herein, I will use *S. flexneri* as an example to introduce the procedure. Wild type *S. flexneri* was cultured at 37 degrees overnight in TSB medium. Overnight cultures were diluted 100 times into the same culture medium and grown to an optical density at 600 nm (OD600) of 0.6 – 1.0 and then diluted by an additional factor of 10. The diluted cell culture was then inoculated into the flow channel (**Figure 2.14**). Cells were allowed to settle to the bottom of the flow channel and adhere to the coverslip for 1 hour. Then, the flow channel was connected to a syringe filled with TSB medium. A syringe pump (Harvard 22 55-2222 Syringe Pump) is used to control the flow rate of the medium. The flow rate could be set in the range from μL/hour to L/hour according to experimental requirements. Setting the appropriate flow rate is required for biofilm growth in the channel. We found the flow rate in the range from 0.4 to 1.0 ml/hour is suitable for *S. flexneri* biofilm growth in our flow channel. Finally, the flow channel is fixed on the sample holder and then imaged with the phase contrast microscope at room temperature. The exposure time is 30 ms. Images are acquired every 5 minutes for several days.

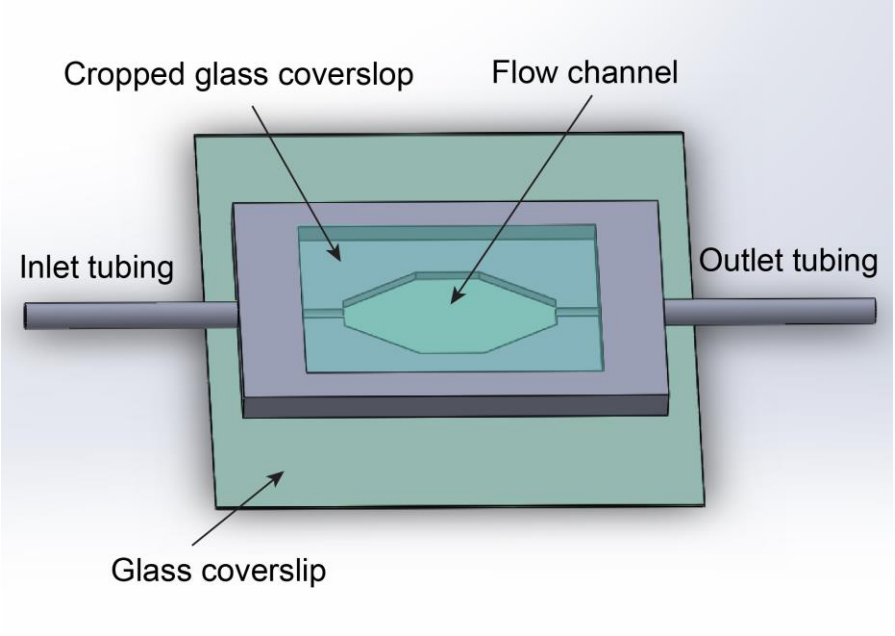


**Figure 2.14** Flow chamber system for phase contrast microscope. The main body of the flow chamber is 3D printed and then glued on a 25 by 25 mm glass coverslip (VWR Inc.). The top of the flow channel is sealed with a piece of cropped glass coverslip. The dimension of the flow channel is length: 10 mm, width: 5 mm and height: 0.5 mm. The media flow is driven into the channel with a stainless-steel tubing (McMaster). The inner diameter of the inlet and outlet tubing is about 0.4 mm. Biofilms will develop in the flow channel on the bottom coverslip and be imaged from the bottom.

### 2.3.7.2 Imaging with LLSM

Herein, I will use *Shewanella oneidensis* MR-1 strain as an example to introduce the main procedure for imaging with LLSM. Procedure for imaging other strains will be introduced in detail in corresponding chapters.

*S. oneidensis* MR-1 GFP strain was cultured in LB media with 50 μg/ml kanamycin at 30 degrees Celsius. Overnight cell cultures were diluted by 100 times and then grown to an OD 600 of about 0.6. The overnight-grown cultures were then diluted by an additional factor of 10. Round glass coverslips with the diameter of 5 mm were put into a 24-well plate (Falcon) and 400 μL of the diluted cell culture were added to the well. Cells were allowed to settle and adhere to the coverslip for 1 hour. Then, the sample was set onto the sample arm and put into the sample-basin on LLSM, which was filled with 10% LB medium. The sample was imaged at room temperature with 488 nm light sheet produced by a time-averaged (dithered), square lattice pattern (137). 3D image stacks of 400 planes were acquired with an exposure time of 50ms and a step size of 200 nm.

### 2.3.8 Raw Data Processing

The imaging plane has an angle of 31.5 degrees in respect to the horizontal plane of the sample coverslip, and therefore an offset exists between frames when collecting images by scanning the sample horizontally (**Figure 2.15**). The first step for data processing is to remove that offset by de-skewing each frame (**Figure 2.15**). The following

step is to subtract the background, which is estimated by averaging intensity values of dark areas (devoid of cells) in the field of view. The de-skewed and background subtracted data are then deconvolved using the Richardson-Lucy algorithm (137, 138) with experimentally measured PSFs as the deconvolution kernel. The numbers of iteration for this deconvolution algorithm need to be optimized. Larger numbers of iterations could introduce artifacts to the final results, while insufficient iterations will not output the resulting image with the highest contrast. Finally, the reconstructed 3D images are rendered using the 3D Viewer plugin in Fiji (222). The deconvovled results can give a sense of the biomass of the biofilm and will be used as input data for the single cell segmentation algorithms.

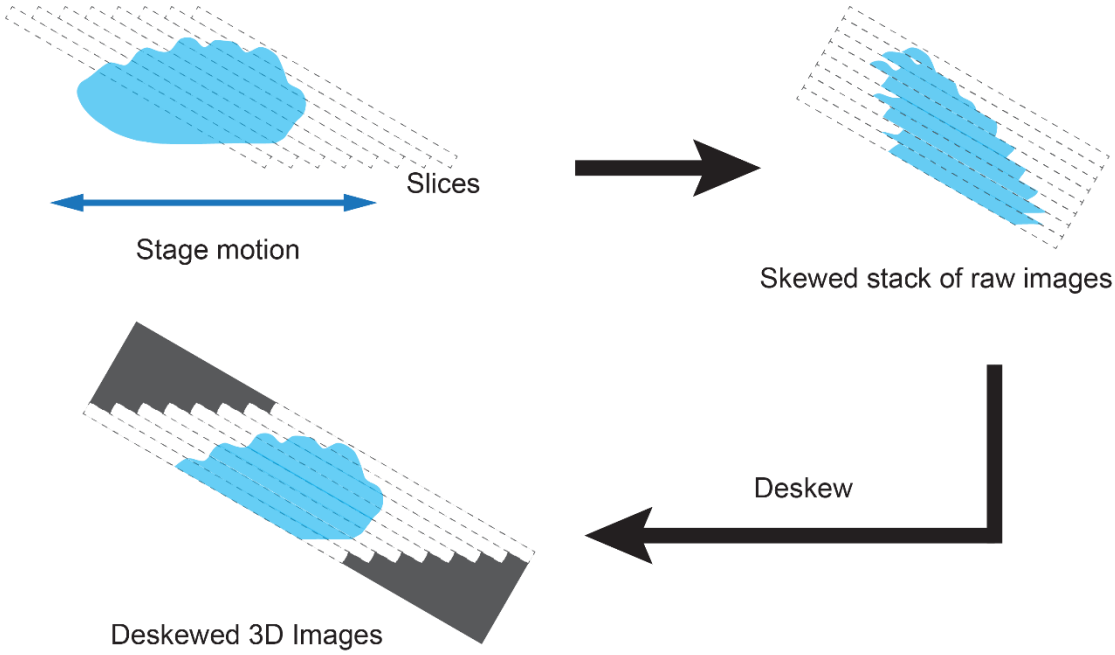


**Figure 2.15** Deskew the raw data. Offsets are added into each frame of images to compensate the skewed image stack caused by the tilted detection objective lens.

# Chapter 3: Development of a flow chamber system for imaging bacterial biofilms with LLSM

## 3.1 Abstract

Lattice light sheet microscopy (LLSM) enables spatial and temporal measurements of live bacterial biofilms with subcellular resolution. However, this potential has not yet been implemented due to the lack of a compatible sample platform for culturing as well as imaging biofilms. The perpendicular angle between the excitation and detection objective lens of LLSM and the limited space at the imaging plane disable the application of conventional flow channels. In this work, we designed a novel flow channel system that allows imaging biofilms in vivo with LLSM. The performance of the flow channel is evaluated by comparing the lattice pattern and point spread function (PSF) inside and outside the channel. Negligible influence on the imaging performance of LLSM was demonstrated.

## 3.2 Introduction

Biofilms are microbial communities of microorganisms aggregated on a surface. Cells in biofilms are embedded in an extracellular polymeric substance (EPS), which provides a protective and stable growth environment. Biofilm formation is harmful in many scenarios. For example, the formation of biofilms in industrial equipment can cause damage and loss of productivity. Further, biofilms growth on medical devices can result in infection. On the other hand, biofilms also have great potential for creating economic benefits, such as bioremediating hazardous wastes and biofiltering wastewater (12, 17, 19-26). They are also potential renewable energy sources when building microbial fuel cells (MFCs) (12, 17, 19-26).

The potential threats and benefits of biofilms have encouraged researchers to study them with the goal to manipulate their growth to enhance prevention methods as well as their beneficial applications. To conduct these studies, various types of approaches for growing and inspecting biofilms have been developed. The devices for biofilm formation can be categorized into two types, static and dynamic with continuous flow. Polystyrene microtiter plates and Calgary biofilm devices are examples of static assays (156, 157) in which the biofilm can be quantified by measuring all biomass formed either on the surfaces of the wells or the pegs of the coverlid (156-158). Robbins device, drip flow biofilm reactors and rotary biofilm reactors allow biofilms to grow under different hydrodynamic conditions (159-162). Biofilms grow on coupons inserted into the liquid stream within these devices. The coupons are mounted on small pistons and can be any material the

researchers want to test. To inspect the biofilms, the coupons must be taken off from the piston and moved out from the devices.

None of the above-mentioned biofilm formation devices are ideal to study biofilms *in situ*. To solve this problem, flow chamber systems have been developed for real-time monitoring of live biofilms (163-169). In the design of these devices, the substratum for biofilm growth is set at the bottom of the chamber. The growth media flows from one side of the chamber, across the substratum, and then out of the chamber. There are two different types of flow chamber systems, open type and closed type (106). With the open type, biofilms can be observed either from the open top by immerging the detection device, such as the objective lens of a microscope, into the growth media or from the bottom when the substratum is transparent. With the close type, biofilms can be only observed from the bottom through a detection window where the substratum is positioned. Thus, it requires the substratum to be transparent. Each type of the flow chamber system has its own pros and cons. The open type allows direct and easy access to the biofilm. But, when detecting from the open top, it cannot be used for long-term imaging, such as several days, since biofilms can develop on the objective lens. This issue will not only disable the microscope for imaging but also raise the danger of spreading pathogenic bacteria, such as *P. aeruginosa* and *S. flexneri*. Another more critical issue is that the open type is vulnerable to contaminations (106, 166). While the close type provides a sterilized environment for biofilm development, its application is limited by the requirement that the substratum must be transparent.

To accomplish real-time monitoring of the dynamics of biofilms, in addition to the flow chamber systems, advanced imaging approaches are also required. The two most widely used imaging methods to study biofilms are phase contrast microscopy and confocal scanning laser microscopy (CSLM) (74, 105, 107, 110, 111, 113, 117, 118, 122, 127, 132). Studies on effects of different influencing factors, such as hydrodynamic conditions, chemical reagents and proteins of interest, on biofilm formation and the *in situ* gene expression in live biofilms have been carried out by the combination of flow chamber systems with these microscopic techniques (163-165).

The most attractive advantage of phase contrast microscope is the convenience for sample preparation i.e. no labeling is required. However, it is disadvantaged by the non-availability for 3D imaging. CSLM, as a fluorescence-based microscope, requires the sample to be fluorescently labelled. It allows 3D imaging of biofilms. However, due to its working principle that the reconstruction of a 3D structure is accomplished by scanning the sample with a single point (the confocal volume), the out-of-focus regions will be repeatedly illuminated. Thus, CLSM can easily induce photodamage to the specimen (phototoxicity) and fast photobleaching to the fluorophores used for labeling (133-135). Light sheet microscopy (LSM) solves this problem by sectioning the sample with the illumination of a single plane. Among different types of LSM (4, 137-142, 144, 145, 148), lattice light sheet microscopy (LLSM) provides the desirable optical sectioning. Under the dithering mode, the lateral resolution of LLSM is 230 nm and the axial resolution is ~370 nm, assuming green fluorescent protein (GFP) excitation and emission (137, 138). The excellent spatial resolution and low phototoxicity make LLSM a promising imaging

approach to unravel single cell behaviors in dense 3D biofilms *in situ*. However, due to the lack of a compatible flow chamber system, LLSM has not been applied to on-line monitoring of biofilms yet.

It is challenging to design a flow chamber that can match the imaging platform of LLSM due to the following facts. First, to isolate the environment for biofilm growth from the water-filled basin where two objective lenses are immerged (**Figure 3.1**), the flow chamber must be a closed system. Otherwise, biofilms could develop on the objective lens during long term experiments and thus block both the excitation and emission light. Second, considering the geometry of the excitation and detection optical path, the closed flow chamber must allow imaging biofilms from the top. Conventional close type flow chamber systems don't have this availability, since they only allow imaging from the detection window at the bottom. When imaging from the top, both excitation and emission light will pass through the ceiling of the chamber, thus the refractive index of the material of the ceiling must match that of the solution in the basin. Conventional flow chamber systems made with plastic or glass can't satisfy this requirement. Third, the distance between the excitation and detection objectives at the imaging plane is less than 10 mm (**Figure 3.1**). The confined space limits the flexibility to adjust the design of the flow chamber.

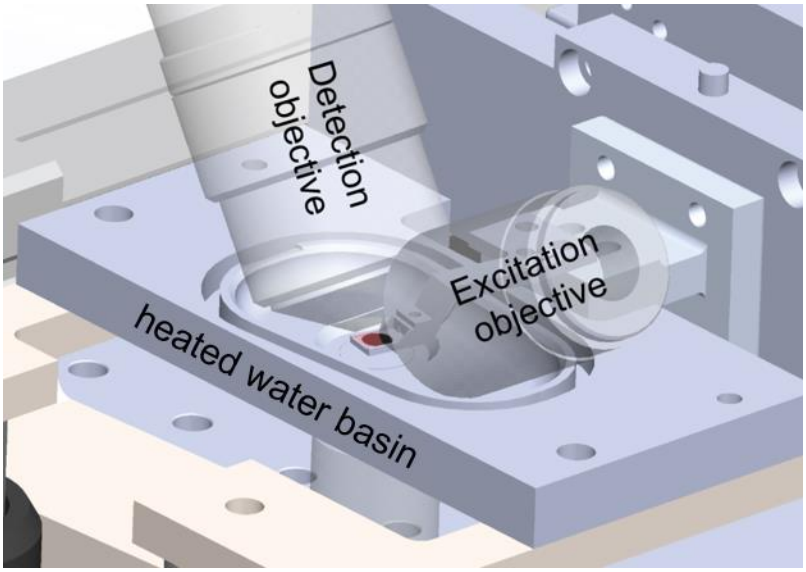


**Figure 3.1** Excitation and detection objectives, and the sample basin of LLSM. The basin is filled with water and also has a heating system to control the temperature.

In this work, we designed a novel flow chamber system that is compatible with the imaging platform of LLSM. In addition to overcoming all above-mentioned barriers, the flow chamber also enables growing biofilms on any materials of interest and allows precise control of the growth conditions. We evaluated the performance of the flow channel by comparing the lattice pattern and the point spread function (PSF) inside and outside the chamber. Negligible influence on the lattice pattern and the PSF was observed, which indicates that the flow chamber would not impact the imaging quality of LLSM. This flow chamber system allows real-time monitoring of biofilms with LLSM, one state-of-the-art microscopy that can image bacterial cells with subcellular resolution. As the general sample holder for LLSM, its application is not limited to studying biofilms. In fact, it

expands the application of LLSM to perform studies when precise *in situ* control of the environmental conditions for the sample is desired.

## 3.3 Methods

The flow chamber is composed of five parts, the main body of the flow chamber without a ceiling, the inlet and outlet tubing, the substrate for biofilm formation, and the thin film to seal the flow chamber. Each part is separately made and then assembled.

### 3.3.1 Design of the Main Body of the Flow Chamber

The model of the flow chamber is designed with SolidWorks 2018 (Dassault Systèmes) (**Figure 3.2**). The width of the flow chamber is 4.70 mm, which can fit the space between the excitation and detection objectives of LLSM. A detection window with a length of 5.00 mm is made on the ceiling of the chamber. The substrate platform is set between the inlet and the outlet (**Figure 3.2b**). It divides the chamber into two parts. The substrate for biofilm formation is positioned on this platform. This design allows the growth media to flow though the inlet, across the substrate for biofilm growth, to the bottom half of the chamber and then to the outlet. There are several reasons why we put the outlet at the same side as the inlet. First, after calibrating the microscope, it's not recommended to move the two objectives, therefore, the flow chamber must be carefully inserted into the narrow space between the two objective lenses and the basin. However, in order to collect waste media from the chamber, a long tube needs to be connected to the outlet. If the outlet tubing is at the end of the chamber, it will be very inconvenient to set

the chamber to the imaging position, because the long tubing must pass through the narrow space between the two objective lenses and the basin first prior to placing the chamber. Second, if the outlet tubing is installed at the end of the chamber, a small hole that can fit its size must be drilled at the end. Then, the metal part of the outlet tubing will be inserted into this small hole. Since the diameter of the hole is only about 0.5 mm, the length of the end of the chamber is about 3 mm while the length of the outlet tubing is about 200 mm, it is almost impossible to firmly fix the outlet tubing with this construction. The long flexible outlet tubing can easily make the chamber leaky. When the outlet tubing is at the same side as the inlet tubing, it can be tightly fixed by being bounded to the lifted arm of the flow chamber with parafilm (**Figure 3.2b**). And there will be no potential problem of leaking.

The main body of the flow chamber is first 3D-printed with plastic material for testing. The final design is 3D-printed with stainless steel (Xometry Inc.). The flow chamber made with stainless steel can be autoclaved, thus easy for cleaning and reusing.

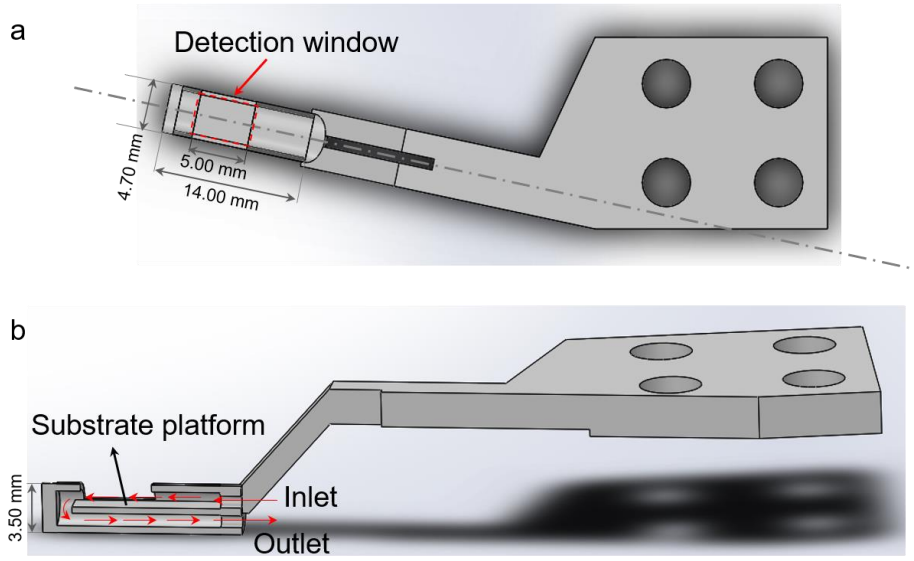


**Figure 3.2** Top and side view of the main body of the flow chamber. (a) The top view. (b) Crop the flow chamber along the dash line and view from the side.

### 3.3.2 Making the Ceiling for the Flow Chamber

The first material we used to make the ceiling for the flow chamber was Teflon fluorinated ethylene propylene (FEP) films (DuPont). However, the large difference between its refractive index and water (FEP: 1.344, water: 1.333) causes large aberration to the lattice light sheet pattern. Then, we decided to make the film by ourselves with the polymer (MY-133-V-2000-BP30, MY Polymers Ltd.) which has the same refractive index as water. The glue (LOCA-133-BP30) to adherent the ceiling to the main body of the flow chamber comes from the same vendor.

The thickness of the polymer film we made was about 50 μm. We first cropped a 6-by-6 cm square window on a piece of Teflon film with the thickness of 50 μm (**Figure 3.3a**). The volume of polymer to make a 50 μm film with this area is about 180 μL. The square Teflon film window was put onto a piece of glass and then 180 μL polymer solution is dropped at the center of the window (**Figure 3.3a**). Then, another piece of glass was put on the top of the Teflon film and the polymer. We pressed the two pieces of glasses to make the polymer expand and evenly fill the square Teflon film window (**Figure 3.3b**). The whole setup was then firmly fixed by two clamps. Finally, we put the setup under UV and waited two hours for polymerization (**Figure 3.3b**).

In real experiments, the growth media to fill the flow chamber might have a different refractive index from water. In this scenario, to achieve the best imaging quality, it is recommended to make the film with a polymer that has the same or similar refractive index as the growth media.

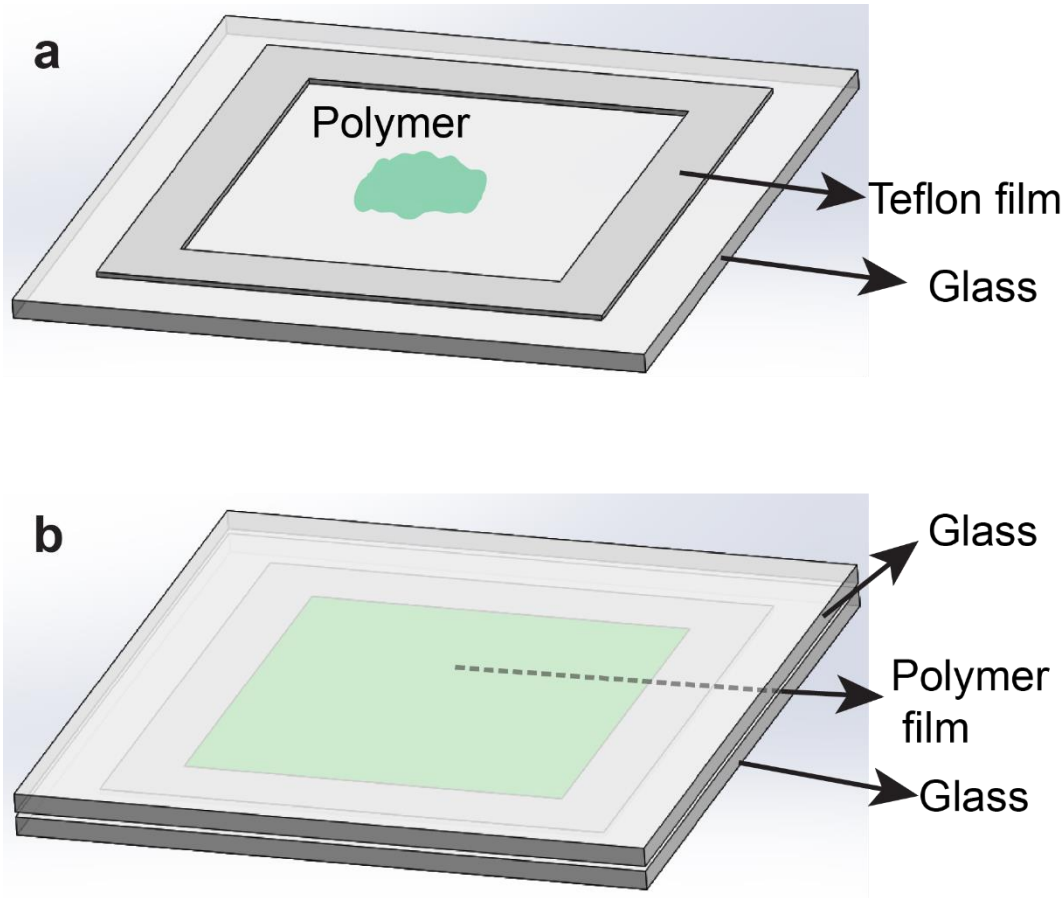


**Figure 3.3** (a) A 6-by-6 cm square window made by cropping a piece of Teflon film with the thickness of 50 µm is put on to a piece of 12-by-12 cm glass. Then, 180 µL polymer (MY-133-V-2000-BP30, MY POLYMERS) is dropped at the center of the window. (b) Another piece of glass is put on the top of the Teflon film and the polymer. Then, the two pieces of glass are tightened by two clamps and exposed to UV for 2 hours to cure the polymer. After that, the polymer will polymerize to form a film with the thickness of about 50 µm.

### 3.3.3 Making the Inlet and Outlet Tubing

The inlet and outlet tubing (**Figure 3.4a**) are made by connecting stainless-steel tubing (diameter: ~0.40 mm, length: 4 cm, 316 Stainless Steel Tubing, McMaster) to Tygon Microbore tubing (inner diameter: 0.51 mm, outer diameter: 1.52 mm, Cole-Parmer). The connection is sealed with heat-shrink tubing. The head of the stainless-steel tubing was bent to match the angle between the lifted arm and the flow channel. The bent head is inserted into the inlet or the outlet of the channel. The other end of the inlet tubing was connected to a 21-gauge syringe needle and then to a syringe, the pool of growth media. The flow rate is controlled by a syringe pump (Harvard 22 55-2222 Syringe Pump) and can be adjusted from the magnitude of μL/hour to L/hour.

### 3.3.3 Assembling the Flow Chamber

Step 1. Autoclave the inlet and outlet tubing. Sterilize the main body of the flow chamber by autoclaving if it is made with stainless steel or by immerging into 70% ethanol for 15 mins if it is made with plastic materials.

Step 2. Cut a piece of the polymer film with the length of 7.00 mm and the width of 12.00 mm. The width closely matches the perimeter of the flow chamber. Sterilize it by immerging into 70% ethanol for 15 mins.

Step 3. Smear a little silicone outside the bent head of the stainless-steel tubing of the inlet and outlet tubing, then insert them into the inlet and outlet of the flow chamber, respectively (**Figure 3.4b**). The added silicone is helpful for sealing. Add silicone between

the lifted arm and the stainless-steel tubing for both the inlet and outlet tubing, then band them together with parafilm (Bemis) (**Figure 3.4c**).

Step 4. Smear the glue outside the flow channel and on the substrate platform inside the channel (**Figure 3.4d**). Wait for 1 hour to let the glue polymerize.

Step 5. Crop the substrate, such as glass coverslip, for biofilm formation to fit the size of the detection window. Then, carefully put it onto the substrate platform (**Figure 3.4e**).

Step 6. Carefully seal the flow channel with the sterilized polymer film. Band each end of the channel with parafilm to help sealing (**Figure 3.4f**).

Step 7. Leave the whole setup overnight, then the flow channel is ready for use.

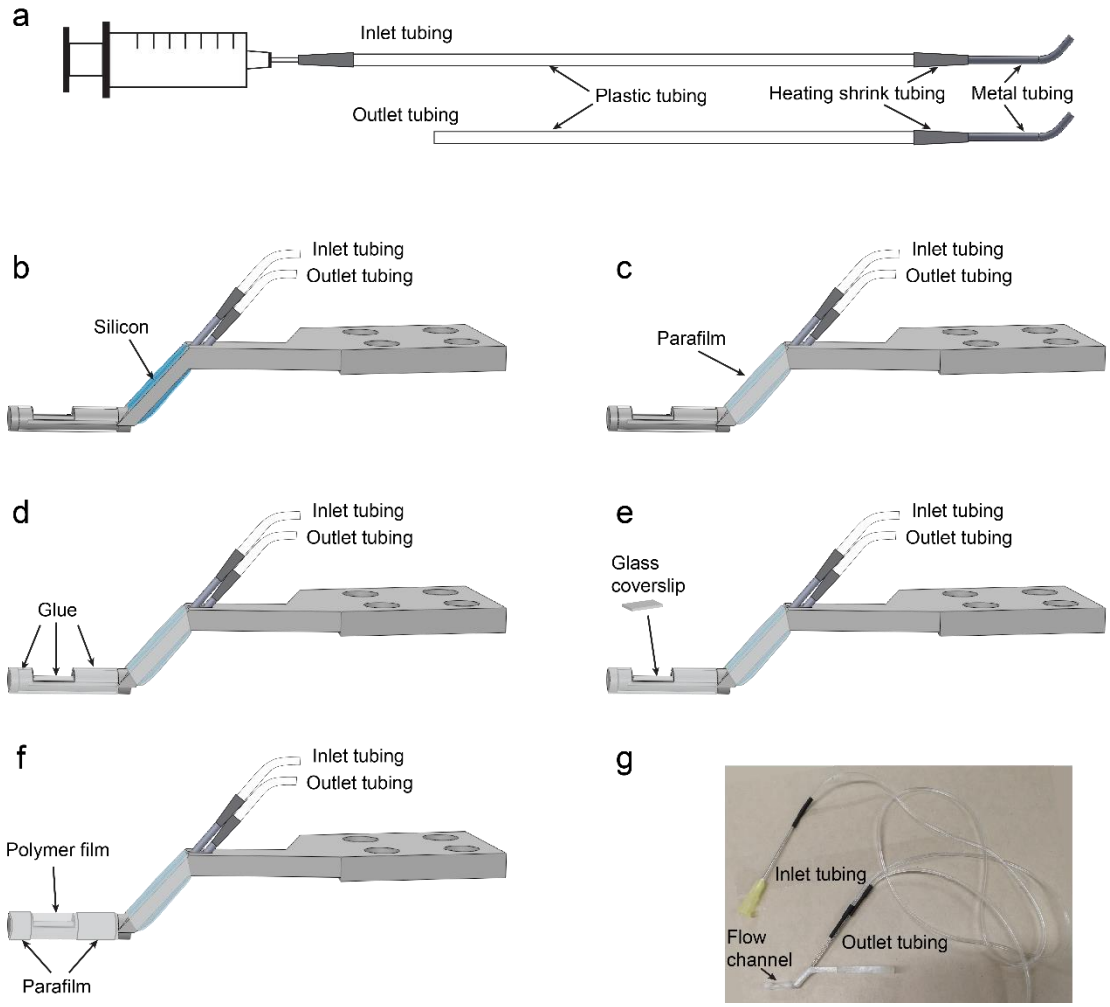


**Figure 3.4** Assembly of the flow chamber system. (a) The inlet and outlet tubing. The heads of the inlet and outlet are made with stainless steel tubing (diameter: ~0.40 mm, length: ~4 cm). They are bent to match the angle between the lifted arm and the flow channel. The metal tubing is then connected to the plastic tubing (inner diameter: 0.51 mm, outer diameter: 1.52 mm). A syringe needle is connected to the other end of the inlet tubing. All connections are sealed with heat-shrink tubing. (b) Insert the inlet and outlet tubing into the inlet and outlet of the flow channel, respectively. Add silicon to fix them. (c) Band the inlet tubing, outlet tubing and the lifted arm together with parafilm. (d) Smear the glue outside the flow channel and on the substrate platform inside the channel. (e) Put the cropped glass coverslip onto the substrate platform inside the channel. (f) Seal the flow channel with the sterilized polymer film. Band each end of the channel with parafilm to

help sealing. (g) An assembled flow chamber system.

### 3.3.4 Samples to Check the Performance of the Flow Chamber

488 nm laser excitable fluorescent beads (diameter: 200 nm, FluoSpheres®, Thermo Fisher) were used as the sample to check the influence of the flow chamber on the lattice light sheet pattern. The beads were coated on glass coverslip (VWR VistaVision) cropped to fit the size of the detection window. The coverslip was positioned on the substrate platform of the flow chamber. The sample basin of LLMS and the whole flow system were filled with DI water.

## 3.4 Results

We first tested how fast the flow rate the flow chamber can tolerate. The flow chamber system is filled with DI water. We set the flow rate to be 200 µL/hour, 1 ml/hour, 5 mL/hour, 10 mL/hour, 15 mL/hour and 20 mL/hour, and let the flow system run 1 hour for each flow rate. Under these tested flow rate, the flow chamber worked well and no leaking was observed. To test the extreme condition, we ran the flow chamber with the flow rate of 20 mL/hour for 5 hours; no leaking was observed.

Considering that the excitation and emission light will both pass through the ceiling of the flow chamber, we then checked the influence of the ceiling on the lattice light sheet pattern. The square lattice pattern in the xz plane at the sample plane were measured (**Figure 3.5 b, c** and **d**). The pattern within the flow chamber sealed with the polymer film

(**Figure 3.5c**) is about the same as that without the chamber (**Figure 3.5b**). However, the flow chamber sealed with Teflon film (**Figure 3.5d**) causes obvious aberration to the lattice pattern.

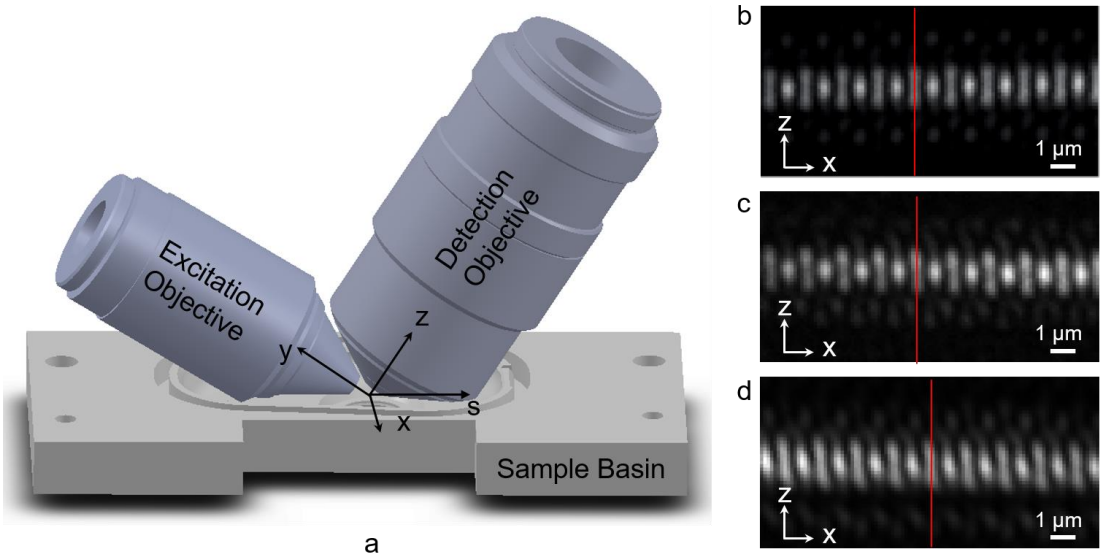


**Figure 3.5** The lattice light sheet pattern in the xz plane. (a) Geometry of the excitation objective, detection objective and the sample basin. (b) Without the flow chamber. (c) Inside the flow chamber. (d) Inside the flow chamber sealed with Teflon. The red lines indicate where the intensity profile will be plotted.

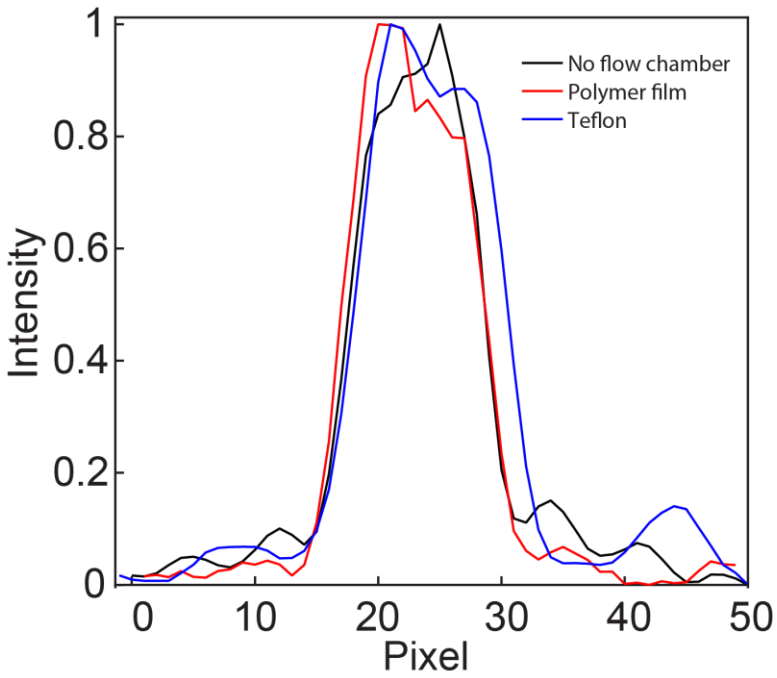


**Figure 3.6** The intensity profile plotted along the red lines shown in **Figure 3.5 b**, **c** and **d**. The intensities are normalized to their maximum values.

We then plotted the intensity profile (**Figure 3.6**) along the red lines shown in Figure 3.5 b, c and d. The width of the peak in each curve indicates the thickness of the illumination light sheet. The width of the peaks (**Figure 3.6** red curve) of the lattice pattern inside the flow chamber sealed with polymer film is about the same as that without the chamber (**Figure 3.6** black curve). However, the width of the peaks (**Figure 3.6** blue curve) of the lattice pattern inside the flow chamber sealed with Teflon film is about 4 pixels wider than that without the chamber. Since the pixel size in the LLSM is about 100 nm, the thickness of the light sheet inside the Teflon film chamber is about 400 nm thicker than without the chamber. In addition, there is one strong side peak at each side of the main peak in the curve of the Teflon film chamber. The side peaks represent the side lobe of the

light sheet illumination. The side lobe excitation will lower the signal to noise ratio, thus resulting in low quality images.

We finally evaluated the influence of the flow chamber on the PSF of the microscope (Figure 3.7). The full width at half maximum (FWHM) of the PSF outside the chamber in x and z directions are 326 and 670 nm, respectively. The FWHM of the PSF inside the chamber in x and z directions are 333 and 660 nm, respectively. The PSF of the microscope inside and outside the flow chamber are almost the same (Figure 3.7). Therefore, we conclude that the flow chamber sealed with the customized polymer film will not impact the image quality of our LLSM.

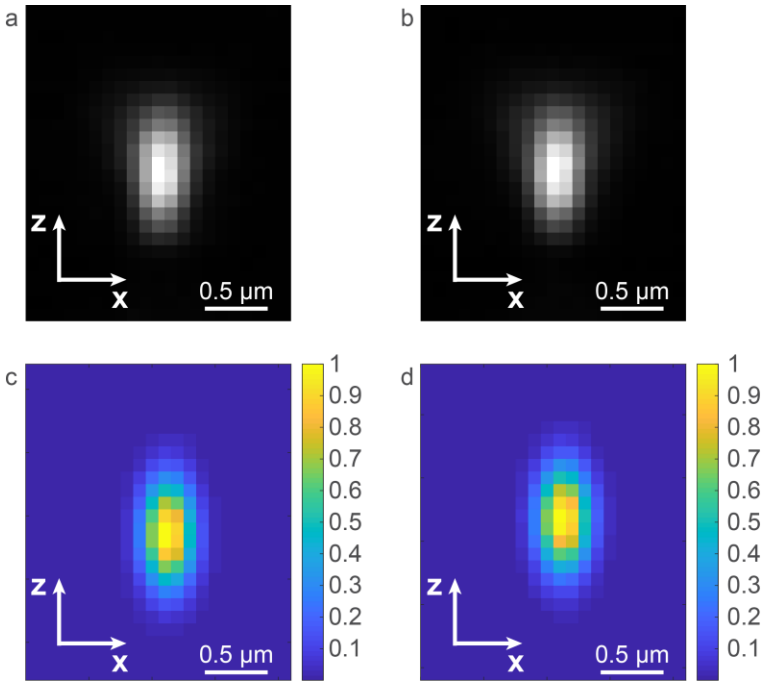


**Figure 3.7** xz PSF of the microscope. (a) Outside the flow chamber. (b) Inside the flow chamber. (c) and (d) are the 2D Gaussian fitting for (a) and (b), respectively.

## 3.5 Conclusions

LLSM has potential for real-time monitoring of 3D biofilms due to its excellent spatial resolution with fast temporal resolution and low phototoxicity. However, its application in the study of biofilms has not been fully exploited, due to the lack of a flow chamber system that is compatible with the imaging platform of LLSM. In this work, we designed a flow chamber system to fill this gap. Besides matching the imaging platform of LLSM, the flow chamber allows the study of biofilm on any desired materials. The flow chamber is sealed with a customized polymer film that matches the refractive index of water. We evaluated the influence of the flow chamber on the performance of the microscope, e.g. the image quality, by comparing the lattice pattern and PSF measured with and without the chamber. The influences are demonstrated to be negligible.

The flow chamber system provides an isolated environment for the sample with controllable conditions, including flow rate, nutrients and temperature. This is particularly important for imaging pathogenic bacterial strains, such as *S. flexneri*, with LLSM. As the general sample holder for LLSM, its application is not limited to monitoring the development of biofilms. Indeed, it paves the way for real-time monitoring of the dynamic process of any biological systems of interest when imaging with LLSM is desirable. In addition, the flow chamber system enables researchers to alternate the growth condition for the sample *in situ* during imaging. Thus, it expands the application of LLSM to perform studies that require this capability.

# Chapter 4: Non-Invasive Single-Cell Morphometry in Living Bacterial Biofilms

This chapter is adapted from the published paper (183).

## 4.1 Abstract

Fluorescence microscopy enables spatial and temporal measurements of live cells and cellular communities. However, this potential has not yet been fully realized for investigations of individual cell behaviors and phenotypic changes in dense, three-dimensional (3D) bacterial biofilms. Accurate cell detection and cellular shape measurement in densely packed biofilms are challenging because of the limited resolution and low signal to background ratios (SBRs) in fluorescence microscopy images. In this work, we present Bacterial Cell Morphometry 3D (*BCM3D*), an image analysis workflow that combines deep learning with mathematical image analysis to accurately segment and classify single bacterial cells in 3D fluorescence images. In *BCM3D*, deep convolutional neural networks (CNNs) are trained using simulated biofilm images with experimentally realistic SBRs, cell densities, labeling methods, and cell shapes. We systematically evaluate the segmentation accuracy of *BCM3D* using both simulated and experimental images. Compared to state-of-the-art bacterial cell segmentation approaches, *BCM3D* consistently achieves higher segmentation accuracy and further enables automated morphometric cell classifications in multi-population biofilms.

## 4.2 Introduction

Biofilms are multicellular communities of microorganisms that grow on biotic or abiotic surfaces (3, 223-225). In addition to cellular biomass, biofilms also contain an extracellular matrix (ECM) which is composed of polysaccharides, DNA, and proteins. Individual cells in biofilms interact with other cells, the ECM, or with the substrate surface, and the sum total of these interactions provide bacterial biofilms with emergent functional capabilities beyond those of individual cells. For example, biofilms are orders of magnitude more tolerant towards physical, chemical, and biological stressors, including antibiotic treatments and immune system clearance (3, 223, 226-229). Understanding how such capabilities emerge from the coordination of individual cell behaviors requires imaging technologies capable of resolving and simultaneous tracking of individual bacterial cells in 3D biofilms.

Live cell-compatible imaging technologies, such as optical microscopy, can reveal the spatial and temporal context that affects cellular behaviors. However, conventional imaging modalities are not able to resolve individual cells within thick 3D biofilms over extended periods of time. For example, the diffraction-limited lateral *x*,*y*-resolution (~230 nm) of a confocal fluorescence microscope is barely sufficient to resolve bacterial cells positioned next to each other on flat glass coverslips. Even worse, the diffraction-limited axial *z*-resolution (570 nm) is comparable to the size of a single bacterial cell, so that densely-packed cells become unresolvable in the axial *z*-dimension (230, 231). Notable exceptions include loose biofilms (low cell density), spherical cell shapes (232, 233), and mutant *Vibrio cholera* biofilms, in which cell-cell spacing is increased through the

overproduction of ECM materials (234-236). While single-cell resolved images have been obtained in such special situations, conventional optical microscopy modalities are not generally capable to accurately resolve and quantitatively track individual cells in dense 3D biofilms.

While super-resolution derivatives of confocal microscopy, known as Image Scanning Microscopy (237), can improve spatial resolution, a perhaps more important limitation for long-term live-cell imaging is photodamage to the specimen (phototoxicity) and to the fluorophores used for labeling (photobleaching) (137, 138, 238). In confocal microscopy-based approaches, undesired out-of-focus fluorescence emission is filtered out by confocal pinholes to yield optically-sectioned images with high contrast, i.e. high signal-to-background ratios (SBRs). However, repeated illumination of out-of-focus regions during laser scanning and high light intensities at the focal volume result in rapid photobleaching of fluorophores and unacceptable phototoxicity for light sensitive specimens (137, 138, 238). In fact, confocal fluorescence microscopy (as well as its super-resolution derivatives) uses illumination light intensities that are two to three orders of magnitude higher than the light intensities under which life has evolved (137). The high rates of phototoxicity and photobleaching make confocal-based microscopy unsuitable for high frame-rate time-lapse imaging of living specimens over many hours and days (235, 236, 238-240).

In recent years, light sheet-based fluorescence excitation and imaging approaches have been developed to overcome the drawbacks of confocal microscopy. Among these, lattice light sheet microscopy (LLSM) (137, 138) and field synthesis variants thereof (139), axially-swept light sheet microscopy (ASLM) (140, 141), dual-view light sheet microscopy

(241, 242), and single-objective oblique plane light sheet microscopy (142-145, 148, 243) now combine excellent 3D spatial resolution with fast temporal resolution and low phototoxicity at levels that cannot be matched by confocal microscopy. Specifically, light sheet-based microscopy approaches can operate at illumination intensities that are below the levels of cellular phototoxicity, even for notoriously light sensitive specimens, and reduce fluorophore photobleaching by 20-50 times compared to confocal microscopy, while maintaining comparable spatial resolution and contrast/SBR (137, 148).

An additional challenge in high-resolution biofilm imaging is data quantification. Even if sufficient resolution and high SBRs can be achieved to visually discern, i.e. qualitatively resolve individual cells, robust computational algorithms are still needed for automated cell segmentation and quantitative cell tracking. Towards this goal, image processing approaches based on the watershed technique and intensity thresholding have been developed over the years for single-cell segmentation in bacterial biofilms (234-236, 240). The broad applicability of watershed- and threshold-based image processing algorithms is however limited, because these algorithms require manual optimization of many user-selected parameters. Even with optimal parameters, watershed- and threshold-based image processing methods often produce sub-optimal segmentation results, especially when cell densities are high, when SBRs are low, and when cellular fluorescence intensities are not uniform across the cytosol or the cell surface. To overcome the drawbacks of traditional mathematical image processing approaches, automated solutions based on supervised training of deep convolutional neural networks (CNNs) have been used in recent years with great success for a wide range of problems in biomedical image analysis (244).

Here, we present Bacterial Cell Morphometry 3D (*BCM3D*) (245), a generally applicable workflow for single-cell segmentation and shape determination in high-resolution 3D images of bacterial biofilms. *BCM3D* uses CNNs, *in silico*-trained with computationally simulated biofilm images, in combination with mathematical image analysis to achieve accurate single cell segmentation in 3D. The CNNs employed in *BCM3D* are based on the 3D U-Net architecture and training strategy, which has achieved excellent performance in biomedical data analysis benchmark tests (244). The mathematical image analysis modules of *BCM3D* enable post-processing of the CNN results to further improve the segmentation accuracy. We establish that experimental bacterial biofilms images, acquired by lattice light sheet microscopy, can be successfully segmented using CNNs trained with computationally simulated biofilm images, for which the ground-truth voxel-level annotation maps are known accurately and precisely. By systematically evaluating the performance of *BCM3D* for a range of SBRs, cell densities, and cell shapes, we find that voxel-level segmentation accuracies of >80%, as well as cell counting accuracies of >90%, can be robustly achieved. *BCM3D* consistently outperforms previously reported image segmentation approaches that rely exclusively on conventional image processing approaches. *BCM3D* also achieves higher segmentation accuracy on experimental 3D biofilm data than *Cellpose* (246), a state-of-the-art, CNN-based, generalist algorithm for cell segmentation and the algorithm used by Hartmann *et al.*(236), a specialized algorithm designed for bacterial cell segmentation based on traditional mathematical image processing. We expect that *BCM3D*, and CNN-based single-cell segmentation approaches in general, combined with non-invasive light sheet-based fluorescence microscopy will enable accurate cell tracking over time in dense 3D biofilms.

This capability will launch a new era for bacterial biofilm research, in which the emergent properties of microbial populations can be studied in terms of the fully-resolved behavioral phenotypes of individual cells.

## 4.3 Materials and Methods

### 4.3.1 Imaging of Bacterial Biofilms with LLSM

Fluorescence images of bacterial biofilms were acquired on a home-built lattice light sheet microscope (LLSM). LLSM enables specimen illumination with a thin light sheet derived from 2D optical lattice (247, 248). Here, a continuous illumination light sheet was produced by a time-averaged (dithered), square lattice pattern (137), and the illumination intensity at the sample was <1 W/cm$^2$. The submicrometer thickness of the excitation light sheet is maintained over long propagation distances (~30 μm), which enables optical sectioning, and thus high resolution, high contrast imaging of 3D specimens comparable to confocal microscopy. However, fluorophore excitation by a 2D light sheet reduces phototoxicity, because each excitation photon has multiple opportunities to be absorbed by fluorophores in the excitation plane and produce in-focus fluorescence. Widefield fluorescence images corresponding to each illuminated specimen plane are recorded on a sCMOS detector (Hamamatsu ORCA Flash v2). In this work, 3D biofilm images were acquired by translating the specimen through the light sheet in 200 nm steps using a piezo nanopositioning stage (Physik Instrumente, P-621.1CD). The data acquisition program is written in LabVIEW 2013 (National Instruments)

*E.coli* K12 Biofilm Imaging: Ampicillin resistant *E.coli* K12, constitutively expressing GFP (249), were cultured at 37 degrees overnight in LB medium with 100 μg/ml ampicillin. Overnight cultures were diluted 100 times into the same culture medium, grown to an optical density at 600 nm (OD600) of 0.6 – 1.0, and then diluted by an additional factor of 10. Round glass coverslips with the diameter of 5 mm were put into a 24-well plate (Falcon) and 400 μL of cell culture was added to the well. Cells were allowed to settle to the bottom of the well and adhere to the coverslip for 1 hour. The round coverslips were then mounted onto a sample holder and placed into the LLSM sample-basin filled with M9 medium. GFP fluorescence was excited using 488 nm light sheet excitation. Biofilm growth was imaged at room temperature every 30 min for a total of 20 time points. At each time point, a single 3D image stack contained 400 images, each acquired with a 15 ms exposure time to avoid motion blur.

*M. xanthus* Biofilm Imaging: Strain LS3908 expressing tdTomato under the control of the IPTG-inducible promoter (250) and DK1622 (WT) were cultured in the nutrient rich CYE media at 30 degrees Celsius until it reached an OD600 of 0.6 - 1.0. Media was supplemented with 1 mM IPTG for tdTomato expressing cells. Chitosan (Thermo Fisher)-coated 5 mm round glass coverslips were prepared by incubating coverslips with 1% (w/v) chitosan (1.5 % glacial acetic acid (v/v)) at room temperature for 1 hour. Coverslips were then rinsed with water and placed into a 24-well plate (Falcon) with 350-400 μL of undiluted cell culture. WT cells were stained directly in the 24 well plate with 5 ng/ml FM4-64 (Thermo Fisher) dye. Cells were allowed to settle and adhere to the coverslip for 2 hours. After the settling period, the coverslip was gently rinsed with CYE media to flush away unattached cells. The rinsed coverslip was then mounted onto a sample holder and

placed into the LLSM sample-basin filled with MC7 starvation buffer. tdTomato and FM 4-64 fluorescence was excited using 561 nm light sheet excitation. The 3D image stack contained 400 2D images. Each 2D slice was acquired with an exposure time of 30 ms.

Mixed Strain Biofilm Imaging: Ampicillin resistant *E.coli* K12, constitutively expressing GFP (249), and ampicillin resistant *E.coli* K12, expressing mScarlet (pBAD vector, arabinose induce) were cultured separately at 37 degrees overnight in LB medium with 100 μg/ml ampicillin. Overnight cultures were diluted 100 times into the same culture medium, grown to an optical density at 600 nm (OD600) of 0.6 – 1.0, and then diluted to an OD of 0.1. After dilution, the two strains were mixed together. Round glass coverslips with the diameter of 5 mm were put into a 24-well plate (Falcon) and 500 μL of cell culture was added to the well. Cells were allowed to settle to the bottom of the well and adhere to the coverslip for 1 hour. The cell culture medium was then removed and replaced by 500 uL M9 medium containing 0.2% (w/v) arabinose. The co-culture was incubated at 30 degrees overnight. 10 mins before imaging, the co-culture was stained with 5 ng/ml FM4-64 (Thermo Fisher) dye. 3D image stacks of 20 planes with 5 ms exposure time per frame were acquired using 488 nm excitation.

### 4.3.2 Raw Data Processing

Raw 3D images were background subtracted and then deskewed and deconvolved as described previously (137, 138). The background was estimated by averaging intensity values of dark areas (devoid of cells) in the field of view. Deconvolution was performed using the Richardson-Lucy algorithm with 10 iterations using experimentally measured

point spread functions (PSFs) as the deconvolution kernel. The experimentally measured PSFs were obtained separately for each color channel using fluorescent beads (200 nm FluoSpheres®, Thermo Fisher) coated on a coverslip (251). 3D images were rendered using the 3D Viewer plugin in Fiji (222) or ChimeraX (252).

### 4.3.3 Generation of Simulated Biofilm Images

To generate data for training of CNNs, we computationally simulated fluorescence images of 3D biofilms, for which spatial arrangements among individual cells are known precisely and accurately. Growth and division of individual rod-shaped cells in a population were simulated using CellModeller, an individual-based computational model of biofilm growth (**Figure 4.1a**) (253). In individual-based biofilm growth models, cells are the basic modeling units. Each cell is characterized by a set of parameters, including its 3D position, volume, and spatial orientation. All the cells in the simulated biofilm are then allowed to evolve in time according to predefined biological, chemical, and mechanical rules. For example, cells grow at a defined rate and then divide after reaching a certain volume threshold. Cellular collisions that are due to cell growth are alleviated by imposing a minimum distance criterion between cells at each time point. For our simulations, we chose cell diameter and cell length ($d$, $l$) parameters consistent with a given bacterial species, namely (1 μm, 3 μm) for *E. coli* (254), (0.7 μm, 6 μm) for *M. xanthus* (255), and (1 μm, 1 μm) for spherically symmetric *S.aureus* (256). While the cell volume can be readily adjusted in CellModeller, the cellular volume density, which is determined by the intercellular spacing, is not directly adjustable. We therefore adjusted the cellular volume

density after each simulation by scaling the cellular positions (cell centroids) and thus the intercellular distances by a constant factor, while leaving cell sizes, shapes, and orientations unchanged. This post-processing procedure enabled simulation of the exact same 3D cell arrangements at adjustable cell volume densities.

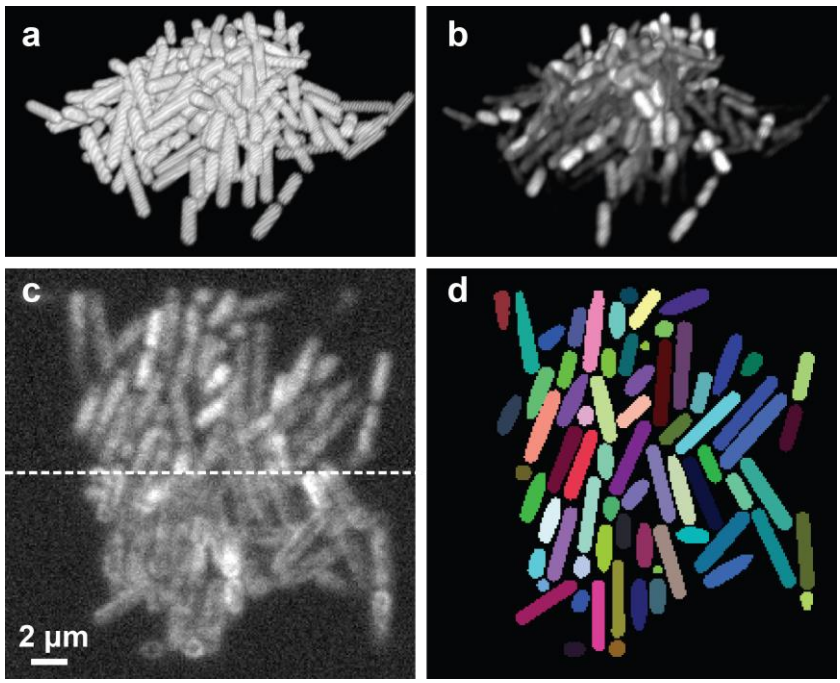


**Figure 4.1** Simulation of fluorescent biofilms images and annotation maps. (a) Cell arrangements obtained by CellModeller. (b) Simulated 3D fluorescence image based on the cell arrangements in a. (c) XY slice through the 3D simulated fluorescence image in b (upper panel shows cells expressing cytosolic fluorescent proteins, lower panel shows cells stained with membrane-intercalating dyes). (d) Ground truth cell arrangements giving rise to the image shown in c. Voxels are displayed as black (background), or in different colors (indicating different cells).

We fluorescently labeled simulated cell volumes and surfaces according to two commonly used labeling strategies in fluorescence microscopy. To simulate expression of

intracellular fluorescent proteins, the fluorescence emitters were placed at random positions within the cell volume. To simulate membrane staining, the fluorescence emitters were placed at random positions on the cell surface. Each cell contained between 500 - 1000 fluorophores to simulate expression level variations between cells, which is often observed in experimental images. Once the fluorophore spatial distributions were determined, a 3D fluorescence image (**Figure 4.1b**) was computationally generated. Each fluorophore was treated as an isotropic point emitter, so that it would produce a diffraction-limited point-spread-function (PSF) on the detector. Experimentally measured 3D PSF shapes (see Raw Data Processing) were used as the convolution kernel. Next, the fluorescence signal intensity was scaled by multiplying the image by a constant factor and then a constant background intensity was added to the image at ~200 photons per pixel, as measured in experimental data. This procedure enabled independent adjustments of the fluorescence signal and background to obtain signal-to-background ratios (SBRs) consistent with experimental data. In a final step, we introduced Poisson-distributed counting noise, based on the summed background and signal intensities, as well as Gaussian-distributed camera read-out noise (experimentally calibrated for our detector at 3.04 photons per pixel on average) (257). This resulting image data (**Figure 4.1c**) was then processed in the same manner as experimental data (see Raw Data Processing). In contrast to experimental data, generation of the corresponding voxel-level annotation maps is fast and error free, because the underlying ground truth cell arrangements are known *a priori* (**Figure 4.1d**).

Differential labeling: To mimic imaging of reporter gene expression in a subset of cells, we simulated biofilm images, in which all cells were stained at the cell surface (e.g.

with a membrane intercalating fluorescent dye) and a subset of cells additionally contained intracellular fluorophores (e.g. through the expression of an intracellular fluorescent protein) (**Figure 4.2a** and **b**). The mixing ratios between membrane-labelled, and membrane and interior labelled cells were 10:90, 30:70, 50:50, 70:30 and 90:10. Ten different cell arrangements containing ~300 cells were simulated for each ratio. To train the CNNs (see next section), six datasets were used, all with a 50:50 mixing ratio.

Mixed cell shapes: To mimic imaging of cells with different morphologies, we simulated biofilms containing spherical and rod-shaped cells **(Figure 4.2c** and **d**). Cell arrangements were first simulated using rod shaped cells and then a fraction of rod-shaped cells is replaced with spherical cells. The size of the rod-shaped cells is that of *E. coli* (~3 × 1 μm, length by diameter). The size of the spherical cells is that of *S. aureus* (~1 μm in diameter) (258). Both cell types were labelled by intracellular fluorophores, as described above. The mixing ratios between rod-shaped and spherical cells were 10:90, 30:70, 50:50, 70:30 and 90:10. Ten different cell arrangements containing ~300 cells were simulated for each ratio. To train the CNNs (see next section), we picked one image from each mixing ratio for a total of five images.

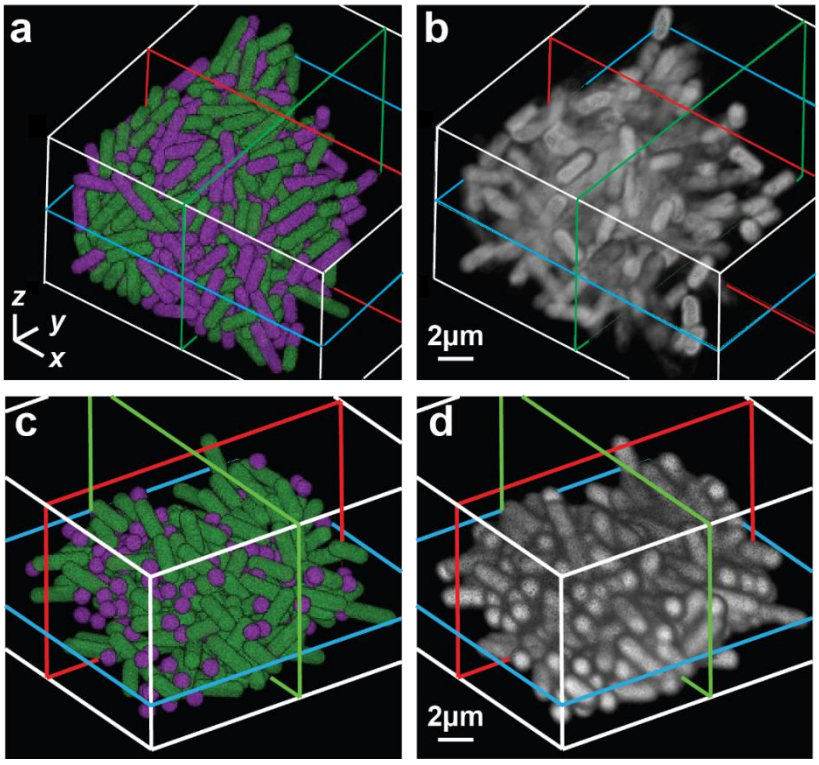


**Figure 4.2** Simulation of mixed labeling and mixed cell shape biofilms. (a) Cell arrangements (green indicates membrane labeled cells, magenta indicates membrane labeled cells that simultaneously express interior fluorescence protein). (b) Fluorescence image based on the cell arrangements in (a) as displayed by the volume viewer plugin of Fiji (259). (c) Cell arrangements (green indicates rod-shaped cells, magenta indicates spherical shaped cells). (d) Fluorescence image based on the cell arrangements in (c) as displayed by the volume viewer plugin of Fiji (259).

### 4.3.4 Training the Convolutional Neural Networks

We trained 3D U-Net CNNs for voxel-level classification tasks (260) within the NiftyNet platform (261) (network architecture depth 4, convolution kernel size 3, ReLU activation function, 32 initial feature maps, and random dropout of 0.5 during training). To

achieve robust performance, we trained these networks using five to ten simulated biofilm images with randomly selected cell densities and signal-to-background ratios (see Generation of simulated biofilm images). The same raw data processing steps used for experimental data (see Raw Data Processing) were also applied to simulated data. 3D deconvolved simulated data and their corresponding voxel-level annotations were used to train the CNNs. Each image used for training contained ~9 million voxels. We trained CNNs by classifying each voxel as 'background', 'cell interior' or as 'cell boundary' based on the underlying cell arrangements. For mixed-species biofilms, two additional classes, 'cell interior' and 'cell boundary' of the second species, were used. This type of annotation scheme has been shown to increase separation of bacterial cells in 2D (174). For data augmentation, we applied NiftyNet's built-in scaling, rotation, and elastic deformation functions. Instead of the original cross-entropy loss function combined with uniform sampling, we used the Dice loss function and 'balanced sampler', so that every label has the same probability of occurrence in training. All networks were trained for 2000 to 3600 iterations with a learning rate of 0.0001. Using these parameters, it took approximately 24 hours to train the CNNs on a NVIDIA Tesla V100 GPU with 16 GB memory.

### 4.3.5 Thresholding of CNN-produced Confidence Maps

Voxel-level classification by CNNs generates different confidence maps (one confidence map for each annotation class). The confidence values range between 0 and 1 and represent the confidence of assigning individual voxels to a given class. After thresholding the 'cell interior' confidence map to obtain a binary image (**Figure 4.3 a-c**),

connected voxel clusters can be isolated and identified as single cell objects using 3D connected component labeling (262). A conservative size-exclusion filter was applied: small objects with a volume ~10 times less than the expected cell size were considered background noise and filtered out using an area open operator (262). Since the cell-interior volumes do not contain the cell boundaries, we dilated each object by 1-2 voxels to increase the cell volumes using standard morphological dilation (262). The threshold value to segment individual cell objects based on the 'cell interior' confidence map was determined by plotting the overall voxel-level segmentation accuracy , quantified as the Intersection-over-Union value (IoU value, aka Jaccard index (263)) versus the confidence value thresholds (**Figure 4.3**). Optimal voxel-level segmentation accuracies were consistently obtained using confidence thresholds between 0.88 and 0.94. Throughout this work, we used 0.94 for cells labeled with intracellular fluorophores and 0.88 for cells labeled with membrane-localized fluorophores.

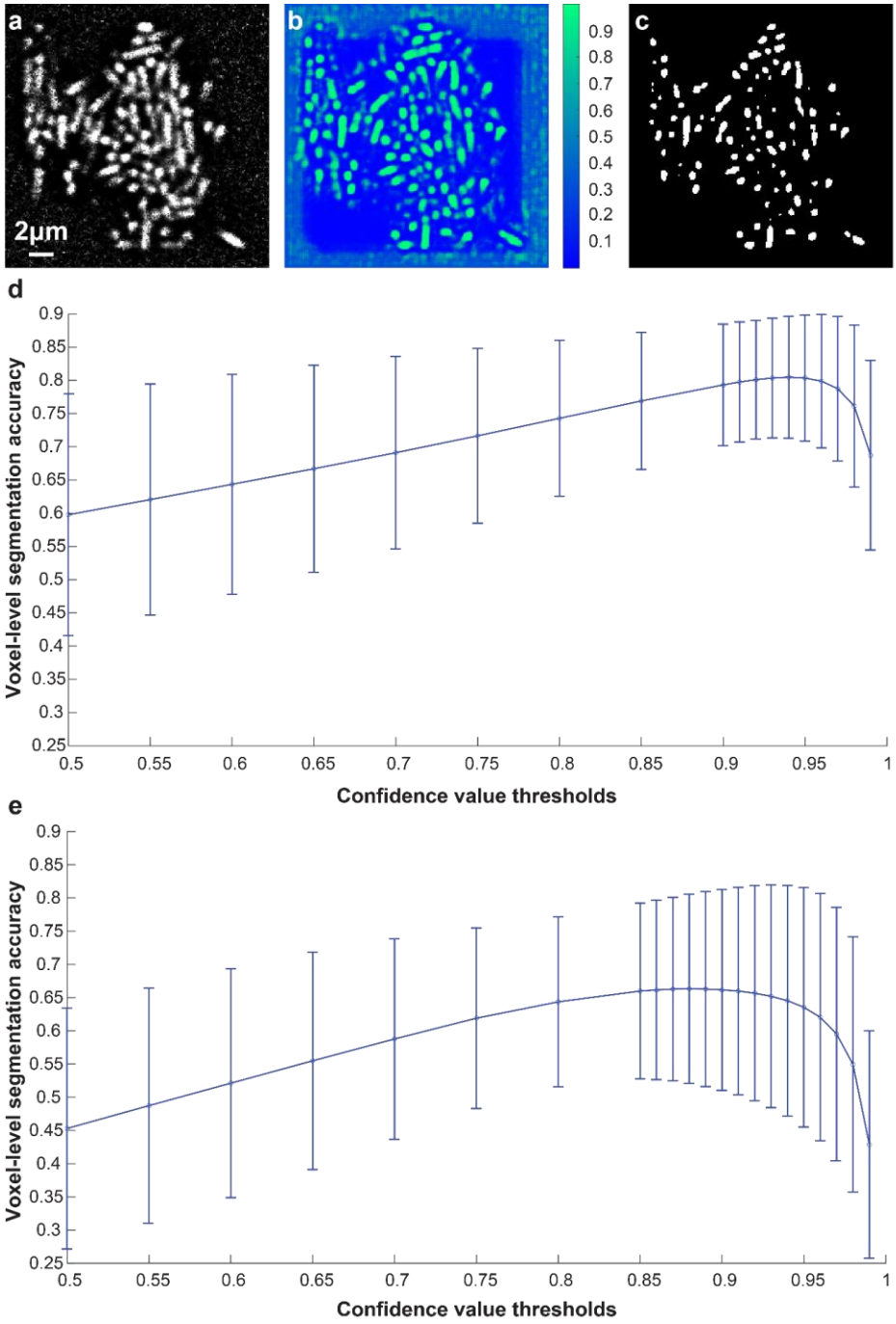


**Figure 4.3** Binary segmentation result produced by thresholding the 'cell interior' confidence map at a high value (0.88-0.94). (a) Deconvolved fluorescence image. (b) 'Cell interior' confidence map. (c) Binary segmentation result (confidence threshold = 0.94). (d and e) Voxel-level segmentation accuracy (y axis) versus the confidence value thresholds (*x* axis) for cells labeled with cytosolic fluorophores (d) and cells labeled with membrane-

localized fluorophores (e). Each curve is plotted by averaging 500 different datasets. Error bars represent ± one standard deviation.

### 4.3.6 Post-processing of U-Net Result using a Refined LCuts Algorithm

Thresholding of the 'cell interior' confidence map produces a binary segmentation result (background = 0, cell interior =1), where groups of connected, non-zero voxels identify individual cells in most cases (**Figure 4.3**). However, when cells are touching, they are often not segmented as individuals, but remain part of the same voxel cluster (undersegmentation). On the other hand, a single cell may be erroneously split into smaller subcellular objects (oversegmentation). Finally, in datasets with low SBR, connected voxel clusters may be detected that do not correspond to cells and thus produce false positive objects (**Figure 4.4a**). To address these errors and improve the segmentation accuracy further, we included additional mathematical image analysis steps to post-process the CNN results and reduce undersegmentation and oversegmentation errors.

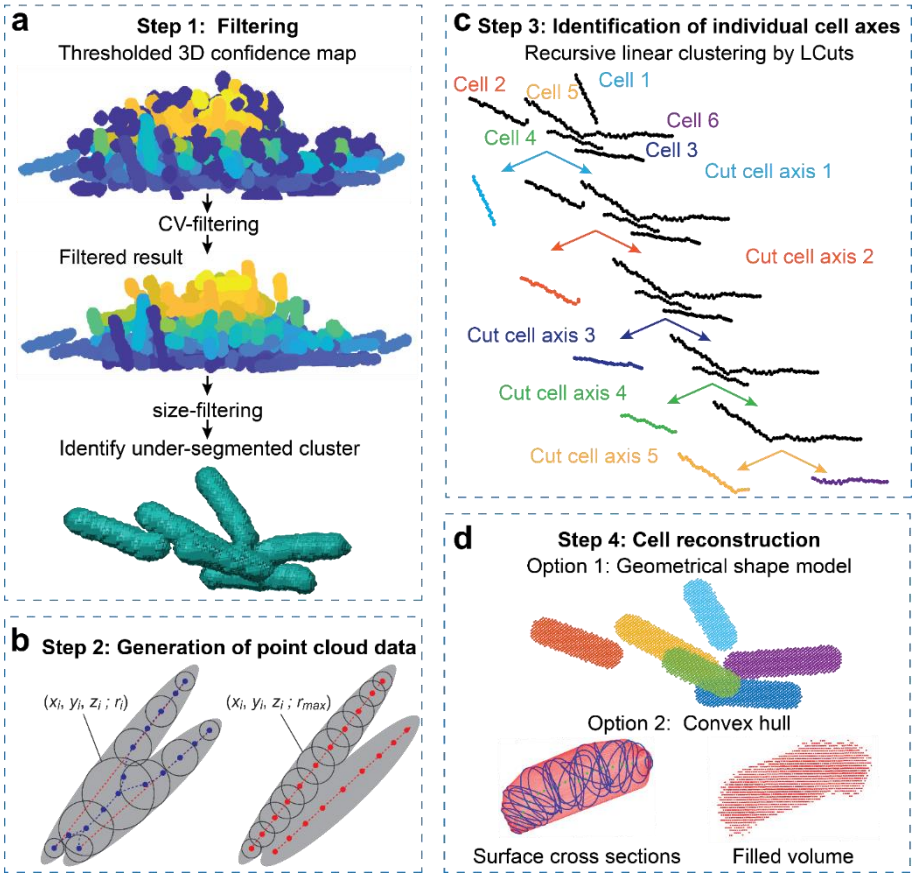


**Figure 4.4** Post-processing of CNN-produced confidence maps using a refined *LCuts* processing pipeline. (a) False positive objects are detected and removed by CV- and size-filtering. Under-segmented clusters that are larger than single cells are selected for further splitting. (b) Illustration of modified medial axis (red dashed lines) extraction to generate point cloud data from fused clusters of rod-shaped cells using the method of inscribed spheres. When cells are touching, the traditional medial axis extraction process fails to align with the actual cell central axis (left). To overcome this drawback, we limited the size of the inscribed spheres based on prior knowledge of bacterial cell diameters (right). (c) The set of inscribed sphere centers are then treated as a fully-connected, undirected graph in 3D with two node features: location and direction (see text and **Figure 4.5** for details). The graph (blue nodes) is then iteratively cut into smaller graphs (red nodes) until the stopping criteria are reached (see text for details). (d) Post-processed graphs represented in different color denoting different cells. The 3D surface of individual cells can be

determined using a geometrical cell shape model (e.g. a spherocylinder for rod shaped bacteria) or by calculating the convex hull around the inscribed spheres found in step 2.

Step 1. Filtering: False positive objects are identified by evaluating the coefficient of variation (264, 265) for each connected voxel cluster *i*:

$$CV_i = \frac{\sigma_i}{\mu_i}$$

where $\sigma_i$ and $\mu_i$ denote the standard deviation and the mean of the intensity taken over all voxels contained in connected voxel cluster *i*. If the coefficient of variation is larger than $\rho$, then the current object will be classified as a false positive object and removed from the confidence map by setting all its voxels to zero. The removed objects will then no longer be counted when evaluating the cell counting accuracy. The value of $\rho$ is selected based on the coefficient of variation of the background. For the datasets analyzed here, this sample coefficient of variation was determined to be $\rho$ = 1.1. After CV-filtering, objects smaller than 25% of the expected bacterial cell size are also removed by setting its voxels to zero. The remaining connected voxel clusters are then considered for further processing (**Figure 4.4a**).

Step 2. Identification of point coordinates along central bacterial cell axes: To identify and delineate individual cells in the connected voxel clusters identified in the previous step, we implemented medial axis extraction using the method of inscribed spheres(266), with the constraint that the sphere radii do not exceed the expected diameter of a single bacterial cell (e.g. $d$ = 0.8 µm) (**Figure 4.4b** left). The set of $N$ inscribed spheres are tangent to the object's surface and parameterized by $(x_i, y_i, z_i; r_i<d/2)$ for $i = 1, \ldots, N$. Determination of the $(x_i, y_i, z_i; r_i)$ coordinates is achieved using the Euclidean distance

transform of the objects' boundary(267), so that the points with coordinates $(x_i, y_i, z_i)$ reliably trace out the central cell axes of individual bacterial cells (**Figure 4.4b** right).

Step 3. Identification of individual cell axes: To separate different linear segments after cell axis extraction (**Figure 4.4c**), we used a refined version of the linear cuts (*LCuts*) algorithm(268, 269). *LCuts* is a graph-based data clustering method designed to detect linearly oriented groups of points with certain properties. The fundamental elements of a weighted mathematical graph are nodes, edges, and edge weights. Here, the points with coordinates $(x_i, y_i, z_i)$ represent the graph nodes. Edges are the connections among nodes. Edges are assigned weights, for example, to reflect the confidence that two nodes belong to the same group. *LCuts* achieves grouping by assigning weights to edges in the fully connected graph to reflect the similarity between two nodes. The features of each node include its location and direction, where the location of each node is simply its Cartesian coordinates. The direction of each node is found by first determining its 5-hop neighborhood, removing nodes at large relative angles, and evaluating the major direction of the outlier removed neighborhood (**Figure 4.5**).

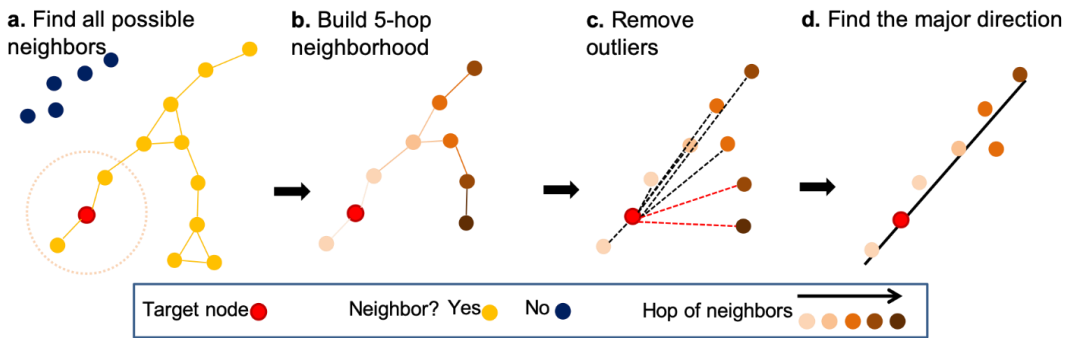


**Figure 4.5** Determination of node direction in an outlier-removed neighborhood (268). (a) A neighborhood of the target node (in red) is a sub-graph, where all adjacent nodes (in yellow) are connected via edges to the target node. Here, if the distance of two nodes is

less than a chosen value (indicated by the dashed circle), these nodes are adjacent to each other. The blue dots are not part of the neighborhood. (b) A hop is defined as the number of edges that one has to traverse from one node to the other node in the graph. Here, the 5-hop neighborhood of the target node is shown. (c) The directional vectors are found from the target node to all the other nodes within in the 5-hop neighborhood (dashed lines). The nodes are classified as outliers if they have large relative angles compared to all the other directional vectors (red dashed lines). (d) Finally, the direction feature of the current node is evaluated as the major direction of the outlier removed neighborhood using principle component analysis.

The algorithm to separate the nodes into different groups is a recursive graph cutting method (268). Graph cuts (*e.g.* nCut (270)) disconnect the edges between two groups of nodes when the combined weights of these edges are minimized. The weights, between node *i* and node *j*, are calculated as follows:

$$w_{ij} = w_D \cdot w_T \tag{4.1}$$

where

$$w_D = \begin{cases} e^{-D_{ij}^2/\sigma_D^2} & \text{if } D_{ij}^2 \le r \\ 0 & \text{if } D_{ij}^2 > r \end{cases} \tag{4.2}$$

$$w_T = e^{-\left(\cos(\theta_{ij})-1\right)^2/\sigma_T^2} \tag{4.3}$$

$w_D$ weighs the distance between two nodes and $w_T$ weighs difference between node directions. $D_{ij}$ is the Euclidean distance between node *i* and node *j*, and r is set to eliminate edges between two far away nodes. $\theta_{ij}$ is the relative angle between the directions of nodes *i* and *j*. $\sigma_D$ and $\sigma_T$ are adjustable parameters that control the rate of exponential

decay. *LCuts* continues to separate groups of nodes until each group satisfies a stopping criterion. The stopping criterion is biologically inspired based on the expected length $L$ of a single bacterial cell and a group's linearity after each recursion. *LCuts* yields linearly oriented groups of points that trace out the central axes of individual cells (**Figure 4.4c**). Importantly, cell separation is achieved without having to specify the number of cells in the biofilm in advance. Furthermore, to limit the need for optimization of postprocessing routines, the four adjustable parameters used in *LCuts*, namely cell diameter $d$, the cell length $L$, and the decay parameters $\sigma_D$ and $\sigma_T$ are chosen based on *a priori* knowledge about the bacterial cells under investigation. We found that the performance of *LCuts* is not sensitive to the particular values of $d$, $L$, $\sigma_D$ and $\sigma_T$ as long as they are consistent with the imaged bacterial cell sizes and shapes (**Figure 4.6**). Identification of single cells provided by *LCuts* alleviates under-segmentation errors of the CNN-based segmentation.

Step 4. Cell reconstruction: The final output of linear clustering can provide length, location and orientation of each cell. Based on these linear clusters, the cellular architecture of the biofilms can be reconstructed by placing geometrical models of cells in space as shown in **Figure 4.4d**. For fast computation, spherocylinders are used as the geometrical model using a radius consistent with the known sizes of bacterial cells. To further refine the cell surfaces to better align with the CNN-segmented volumes, we enclosed the inscribed spheres found in Step 2 in a convex hull (**Figure 4.4d**).

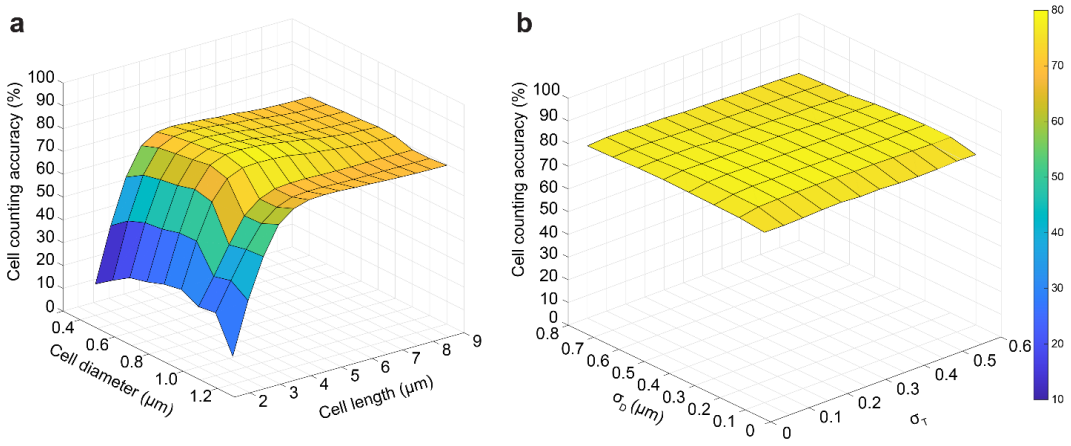


**Figure 4.6** Validation of parameter selection for *LCuts* postprocessing by grid search. Shown is the cell counting accuracy averaged over 20 randomly chosen, simulated datasets of low SBR and/or high cell density, for which post-processing is required. (a) Average cell counting accuracy as a function of cell diameter $d \in [0.4, 1.2]$ µm and cell length $L \in [2, 9]$ µm at a fixed $\sigma_D = 0.5$ µm and $\sigma_T = 0.2$. (b) Average cell counting accuracy as a function of $\sigma_D \in [0.1, 0.8]$ µm, and $\sigma_T \in [0.05, 0.6]$ with fixed $(d, L)$=(0.8, 4.5) µm. The cell counting accuracy is largely unaffected by variations in $d$, $L$, $\sigma_D$ and $\sigma_T$ and robustly remains above 70% for biologically reasonable parameter values, such as $d \sim 0.8$ µm, cell length $L \sim 6$ µm, for *E.coli*-like cell shapes. We also choose $\sigma_D = d/2$ and $\sigma_T = 0.2$, so that edges between nodes separated by more than a cells radius or with relative angles >30° are weighted down.

### 4.3.7 Performance Evaluation

We quantified segmentation accuracy both at the cell-level (object counting) and at the voxel-level (cell shape estimation). To quantify the cell-level segmentation accuracy, we designated segmented objects as true positive (*TP*) if their voxel overlap with the ground truth or the manual annotation resulted in an IoU value larger than a particular IoU matching threshold. This criterion ensures one-to-one matching. A threshold of 0.5 is

typically chosen when reporting single cell counting accuracy values (246, 271). We follow this convention here. If the segmented cell object could not be matched to a ground truth/manually annotated cell volume, then it was counted as a false positive (*FP*) and the IoU value of that segmented object was set to zero. If a ground truth/manually annotated cell volume was not identified in the image, then it was counted as false negative (*FN*). The cell (object) counting accuracy was then defined as $TP/(TP+FP+FN)$. The average IoU value over all segmented objects in the image quantifies the voxel-level segmentation accuracy, i.e. the accuracy of cell shape estimation.

To evaluate the accuracy of cell segmentation on experimental data, three researchers separately traced the cell contours on experimental 2D slices by using freehand selections in Fiji ROI Manger (259). Because human annotation is very time consuming (about 50 hours for a complete 3D dataset containing ~300 cells in a 22 x 32 x 12 $um^3$ volume), one to three single 2D slices were selected for each dataset. One exception is the 3D *M. xanthus*, for which the cell outlines in all available x, y and z slices were traced manually (**Figure 4.7a**). For straight, rod-shaped cells, the centroids of the resulting 2D cell contours all fall within the cell interior volume. To group together the contours belonging to the same cells, the centroid of each contour was projected along the x, y and z dimension. If the projected centroid was enclosed by any other contour in a different slice, then the centroid of that contour was projected onto the plane of the initial contour. Two contours were labeled as related if they contained each other's projected centroids (**Figure 4.7b**). This process is repeated for all possible contour pairs and their relationship is recorded in an adjacency matrix. Next, related contours were assigned to individual cells (**Figure 4.7c**). To separate incorrectly grouped contours, we additionally identified clusters

of centroids using the DBSCAN point clustering algorithm (272) (**Figure 4.7d**). In a final step, we manually removed incorrectly traced contours (**Figure 4.7e**). Cells are reconstructed by creating convex hulls with the grouped contours (**Figure 4.7f** and **g**). This procedure determined the approximate positions, shapes, and orientations of individual cells in the 3D biofilm.

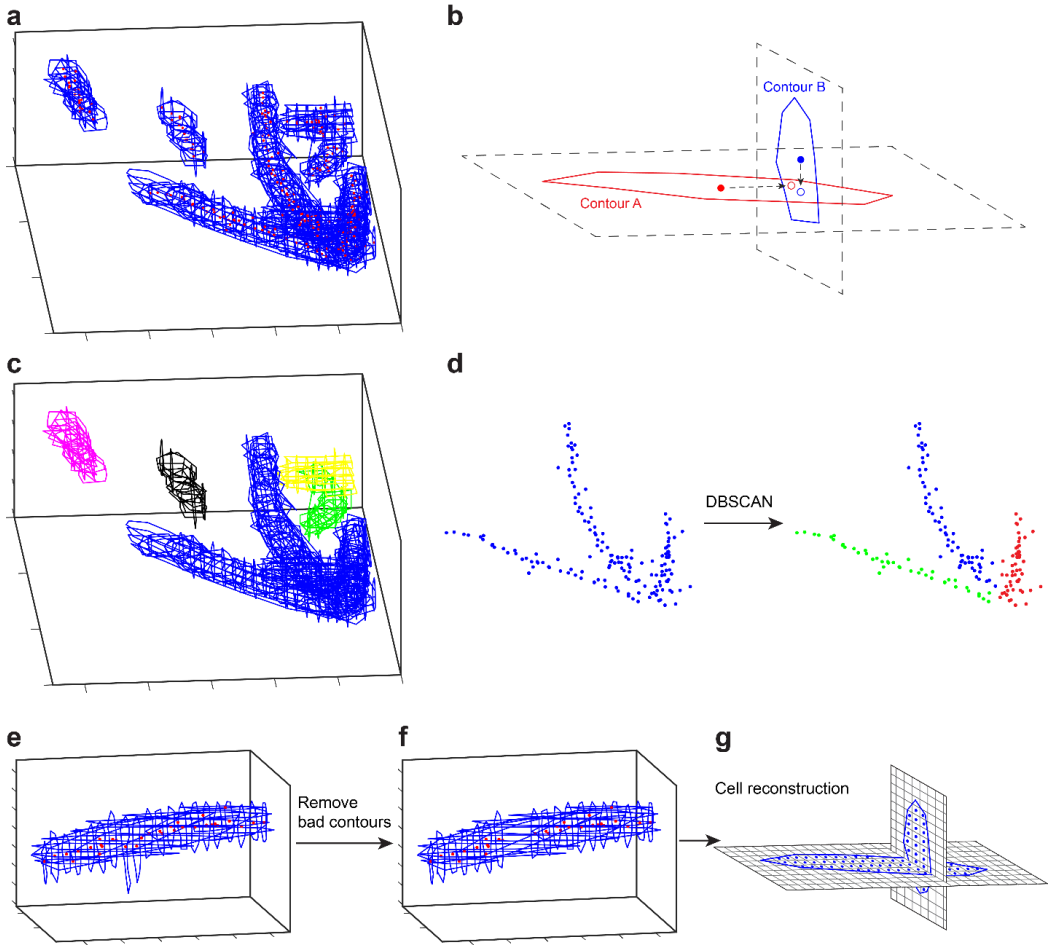


**Figure 4.7** Manually trace cell outline. (a) Cell outlines in all available x, y and z slices were traced manually. (b) Find the contours belonging to the same cell. The centroid of each contour was projected along the x, y and z dimension. If the projected centroid was enclosed by any other contour in a different slice, then the centroid of that contour was

projected onto the plane of the initial contour. Two contours were labeled as related if they contained each other's projected centroids. This process is repeated for all possible contour pairs and their relationship is recorded in an adjacency matrix. (c) The related contours are grouped as cells. Different colors represent different cells. (d) Segment big clusters that contain more than one cell by grouping the centroids of the contours. This step will run manually and iteratively to segment all single cells from the big cluster. (e) Manually check all contours for each cell. (f) Remove the bad contours, such as unreasonably large ones. (g) A convex hull is built based on the contours for each cell. The convex hull is then used as the mask to extract cell volume from the raw data.

To estimate the SBRs of both simulated and experimental images, we manually selected and determined the intensities of approximately ten 'signal' and ten 'background' regions in the images. We computed the SBR as the mean signal intensity divided by the mean background intensity. To estimate the local density of a biofilm, we partitioned the image into several 3D tiles of size 64 by 64 by 8 voxels. We then estimated the local density as the total cell volume contained in each tile divided by the tile volume. We calculated the mean density of the 10 densest tiles to define the 'local density' metric reported for each dataset in the paper. To estimate the cell density in an experimentally acquired biofilm image, the same calculations were performed on either 3D manual annotations (if available) or binary masks obtained by CNN-processing.

## 4.4 Results and Discussion

### 4.4.1 Cell Segmentation by Thresholding CNN Confidence Maps

CNNs have been shown to perform well on pixel-level classification tasks for both 2D and 3D data (273, 274). Bacterial biofilms, however, present a unique challenge in this context. The cell shapes to be segmented are densely packed and barely resolvable even with the highest resolution optical microscopes. Additionally, living biofilms in fluorescence microscopes can only be imaged with low laser intensities to ameliorate phototoxicity and photobleaching concerns. Unfortunately, low intensity fluorescence excitation also reduces the SBR in the acquired images. So far, it remains unclear to what extent single-cell segmentation approaches can accurately identify and delineate cell shapes in bacterial biofilm images obtained under low intensity illumination conditions. To address this question, we implemented an *in silico* CNN training strategy (Chapter 4.3 Materials and Methods) and systematically evaluated its voxel-level classification (cell morphometry) and cell counting accuracies using simulated biofilm images with varying cell densities and SBRs similar to those encountered in experimental data.

We compared two commonly used cell labeling approaches, namely genetic labeling through the expression of cell-internal fluorescent proteins (**Figure 4.8a-c**) and staining of the cell membranes using fluorescent dyes (**Figure 4.8d-f**). For both labeling approaches, voxel-level segmentation and cell counting accuracies, obtained by thresholding CNN confidence maps (Chapter 4.3 Materials and Methods), depend mostly on cell density, whereas the SBR plays a less important role. For cell-internal labeling, SBRs of >1.7 and cell densities of <60% consistently produce voxel-level classification

accuracies of >80% and cell counting accuracies of >95%. On the other hand, SBRs of <1.7 and cell densities of >60% lead to lower segmentation accuracies. While lower segmentation accuracies are expected for higher cell densities and lower SBRs, the sharp drop-offs observed here may indicate a fundamental performance limitation of the CNNs employed. Still, the voxel-level classification and cell counting accuracies consistently surpass previous approaches for bacterial cell segmentation for commonly encountered cell densities and SBRs. Specifically, the cell counting accuracies obtained by Hartmann *et al.* (236), *Seg3D* (275), and Yan *et al.* (234) quickly drop to zero as a function of increasing IoU matching threshold (a quantitative measure of cell shape similarity relative to the ground truth, Chapter 4.3 Materials and Methods), indicating that cell shapes are not accurately estimated by conventional image processing approaches (**Figure 4.8g-i**). We also evaluated the segmentation accuracy of *Cellpose*, a recently developed, CNN-based cellular segmentation algorithm (246). The segmentation accuracy of *Cellpose* is comparable or superior to the best-performing conventional image processing approaches – a considerable achievement given that *Cellpose* was trained primarily on images of eukaryotic cells. However, being a pre-trained generalist model, the segmentation accuracy of *Cellpose* is lower than the accuracy achieved by the specialist *in silico*-trained CNNs of *BCM3D*, which were trained specifically for 3D bacterial biofilm segmentation. Overall, the cell counting accuracies obtained by *BCM3D* are higher than other methods and remain higher even for IoU matching thresholds larger than 0.5, indicating that cell shapes are more accurately estimated by the *in silico*-trained CNNs.

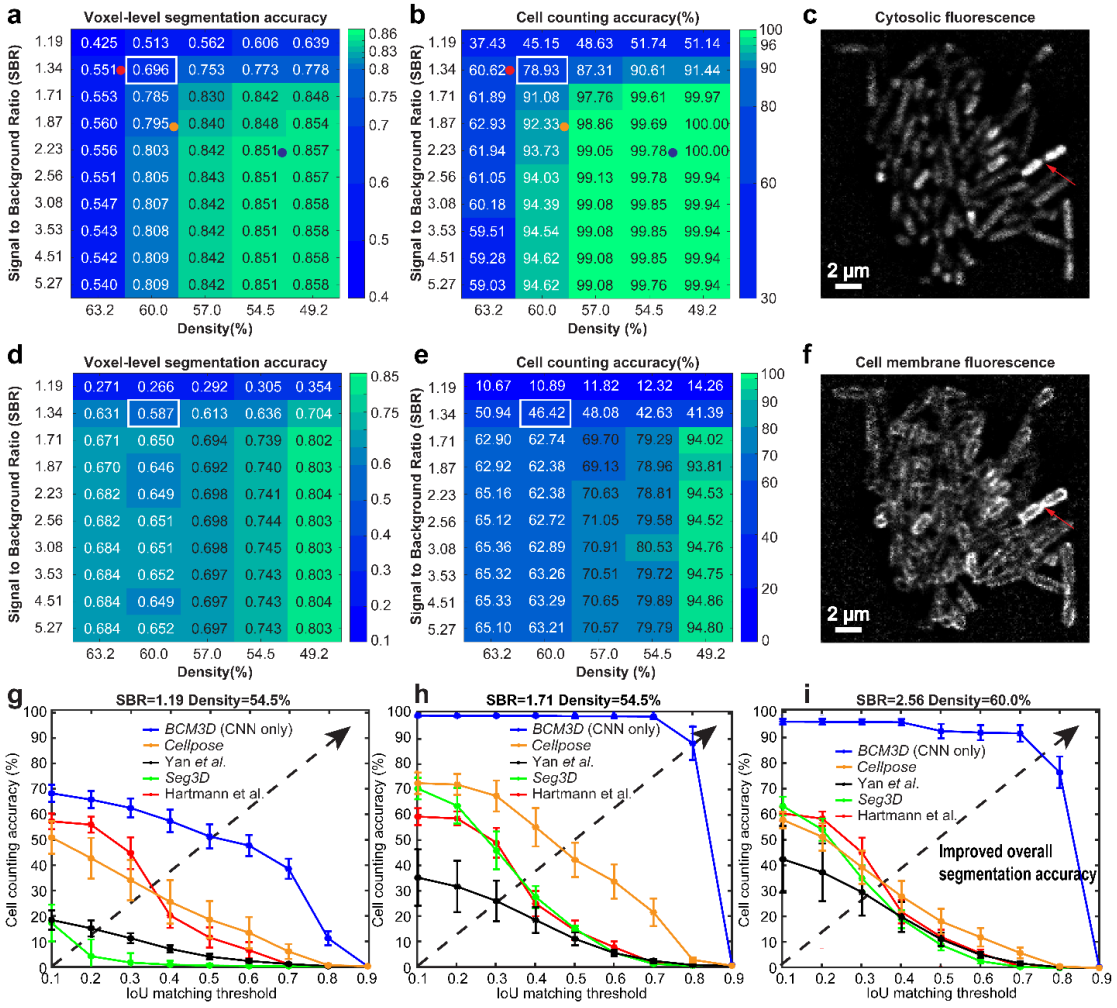


**Figure 4.8** Performance of *BCM3D* using *in silico*-trained CNNs only on previously unseen simulated biofilm images. (a) The voxel-level segmentation accuracy quantifies whether each voxel has been assigned to the correct class ('cell interior', cell boundary', or 'background'). Solid circles represent the maximum local density and average SBRs encountered in experimental datasets (red, orange and blue: *E. coli* expressing GFP). (b) The cell counting accuracy (using an IoU matching threshold of 0.5 for each segmented object, Chapter 4.3 Materials and Methods) averaged over n=10 replicate datasets for cells labeled with cytosolic fluorophores. (c) Example image of cells labeled with cytosolic fluorophores (Cell density = 60.0%, SBR = 1.34, indicated by white rectangle in panels a and b. Similar images were generated $N$ = 10 times with different cell arrangements.) (d) Voxel-level segmentation accuracy and (e) cell counting accuracy averaged over N=10

replicate datasets for cells labeled with membrane-localized fluorophores. (f) Example image of cells labeled with membrane-localized fluorophores (Cell density = 60.0%, SBR = 1.34, indicated by white rectangles in panels d and e. Similar images were generated $N$ = 10 times with different cell arrangements.). The red arrows indicate a close cell-to-cell contact point. (g), (h) and (i) Comparison of segmentation accuracies achieved by conventional segmentation approaches (Hartmann *et al.*, *Seg3D*, Yan *et al.*), *Cellpose*, and *BCM3D* (only using *in silico*-trained CNNs). Three simulated datasets (cytosolic fluorophores) with different SBRs and cell densities are shown. Segmentation accuracy is parameterized in terms of cell counting accuracy ($y$ axis) and IoU matching threshold ($x$ axis, a measure of cell shape estimation accuracy). Each data point is the average of $N$ = 10 independent biofilm images. Data are presented as mean values ± one standard deviation indicated by error bars. Curves approaching the upper right-hand corner indicate higher overall segmentation accuracy, as indicated by the dashed arrows.

The accuracies of single-cell shape estimation and cell counting are predominantly affected by cell density. The variation is more prominent for membrane-stained cells, because *inter*-cellular fluorescence intensity minima are less pronounced when cell membranes are labeled and cells physically contact each other (red arrow in **Figure 4.3c** and **f**). By contrast, intracellular fluorophores produce the highest intensities at the cell center, so that the gaps between cells are more readily resolvable. Also noteworthy is the sharp drop-off in segmentation accuracies for SBRs of <1.7 for all cases. In such low SBR regimes, fluorescence signals of the cells become too difficult to be distinguished from the background. As a result, the CNNs falsely identify random noisy patterns in the background as cells. Additionally, thresholding of the CNN confidence maps often yields connected voxel clusters that contain multiple bacterial cells. False identification and

incomplete delineation of cells cause the pronounced decrease in segmentation accuracy for SBRs of <1.7.

### 4.4.2 Post-processing of CNN confidence maps

To better identify individual cells in low SBR and high cell density datasets, we developed a graph-based post-processing module (Chapter 4.3 Materials and Methods) that takes advantage of the fact that bacterial cell shapes are highly conserved for a given species. Briefly, we transformed the CNN 'cell interior' confidence maps into 3D point cloud data that trace out the central axes of individual cells. This transformation was achieved by medial axis extraction using size-constrained inscribed spheres (266) (**Figure 4.4**). Single-cell axes are then identified as linearly clustered data points by *LCuts* – a graph-based data clustering method designed to detect linearly oriented groups of points (268). The so-identified single-cell axes are then mapped back onto the original segmentation volumes to obtain estimates of the 3D positions, shapes, and orientations of the now separated cells.

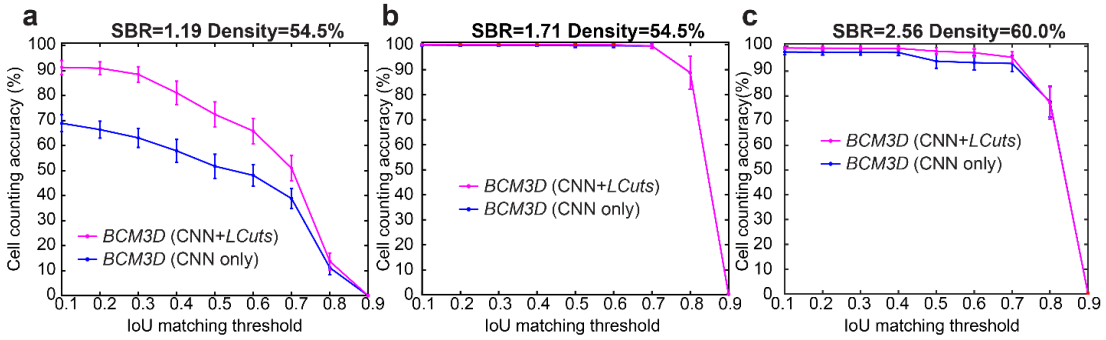


**Figure 4.9** Segmentation accuracies achieved for biofilm images with different SBR and cell densities. (a), (b), and (c) represent results for datasets with SBR 1.19, Density 54.5%, SBR 1.71, Density 54.5% and SBR 2.56, Density 54.5%, respectively. Each curve is plotted by averaging 10 different datasets. Error bars represent ± one standard deviation.

Post-processing with *LCuts* takes advantage of *a priori* knowledge about expected bacterial cell sizes (**Figure 4.9**) by removing erroneously segmented volumes that are significantly smaller than the expected value and by splitting incompletely segmented volumes representing fused cells. Improvements in cell counting accuracy of up to 15% and 36% are observed for cells labeled with cytosolic fluorophores (**Figure 4.10a-c**) and membrane-localized fluorophores (**Figure 4.10d-f**), respectively. The more substantial improvement for membrane-stained cells is due to fact that CNNs trained on membrane-stained cells are more prone to erroneously identifying speckled background noise as fluorescence signals in low SBR images. In addition, membrane-intercalating fluorophores of two adjacent cells are in close proximity, making it difficult to resolve fluorescence signals from two separate cells due to spatial signal overlap (see the red arrow, **Figure 4.8c** and **f**). *LCuts* thus provides an important benefit in improving the cell counting accuracy to an extent not achieved by currently available thresholding- or watershed-based post-processing algorithms (**Figure 4.11**).

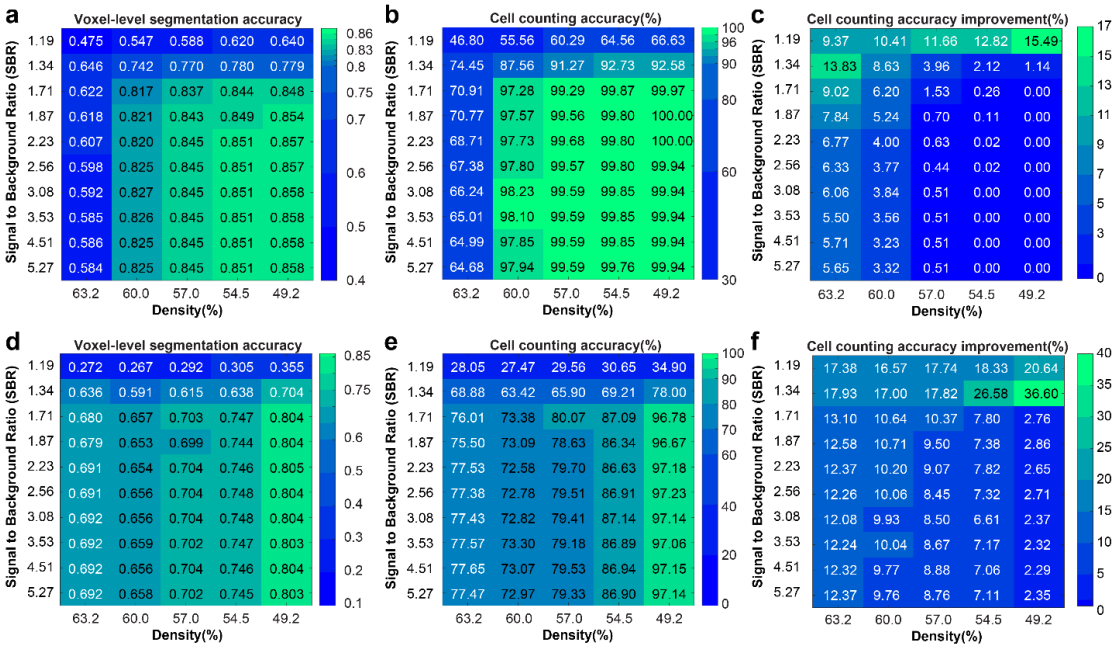


**Figure 4.10** Performance of *BCM3D* (*in silico*-trained CNNs *and* additional post-processing by *LCuts*) on previously unseen simulated data. (a) Voxel-level segmentation accuracy and (b) cell counting accuracy (using an IoU matching threshold of 0.5 for each segmented object) averaged over $N$=10 replicate datasets for cells labeled with cytosolic fluorophores. (c) Improvement relative to *silico*-trained convolutional neural networks without post-processing. (d) Voxel-level segmentation accuracy and (e) cell counting accuracy averaged over $N$=10 replicate datasets for cells labeled with membrane-localized fluorophores. (f) Improvements relative to *silico*-trained convolutional neural networks without post-processing.

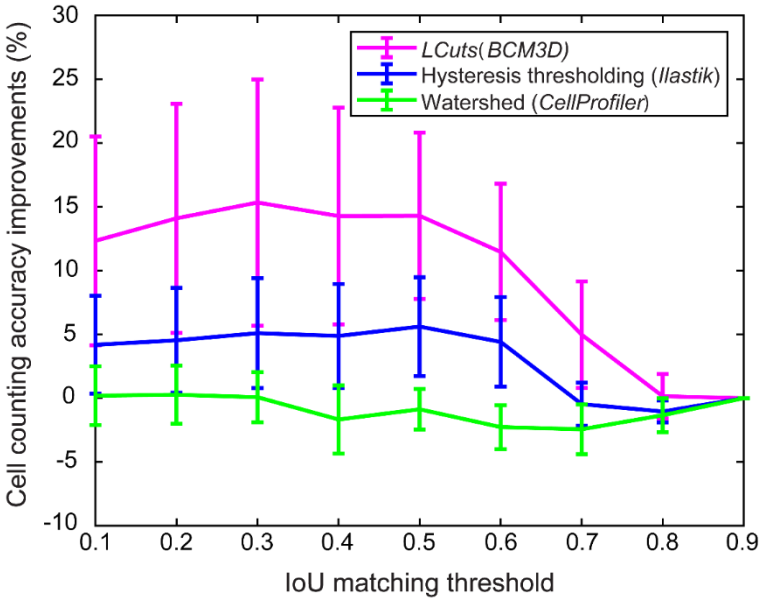


**Figure 4.11** Comparison of *LCuts* to commonly used image post-processing methods. Shown is the cell counting accuracy averaged over 20 randomly chosen, simulated datasets of low SBR and/or high cell density, for which post-processing is required. The hysteresis thresholding-based algorithm of *Ilastik* (276) improves the cell counting accuracy by less than 6% on average for IoU matching thresholds less than 0.6. On the other hand, the watershed-based pipeline used by *CellProfiler* (277) provides negligible improvements and even decreases the average cell counting accuracy in many cases. This decrease is primarily due to oversegmentation. Among the three methods tested, *LCuts* provides the highest improvement in cell counting accuracy (>12% on average for IoU matching thresholds less than 0.6).

### 4.4.3 Segmentation of Experimental Biofilm Images

To test the performance of *BCM3D* on experimentally acquired biofilm images, we acquired time-lapse images of GFP expressing *E. coli* biofilms every thirty minutes for ten hours. We then manually annotated one 2D slice in the 3D images at the t = 5, 6, and 10-hour time points. When referenced to these manual segmentation results, the *LCuts*-

processed CNN outputs consistently achieved better cell counting accuracies than conventional segmentation methods (**Figure 4.12, Figure 4.13**). Initially, *Cellpose* and the Hartmann *et al*. algorithm outperform the *in silico*-trained CNNs on two out of three of the test images ($t$ = 360 and 600 min), for which our *in silico*-trained CNNs struggle with undersegmentation problems. However, mathematical post-processing of the CNN outputs by *LCuts* corrects some of these errors, so that the integrated *BCM3D* workflow achieves improved results compared to *Cellpose* and Hartmann *et al*. at each of the indicated time points. Visual inspection of the segmentation results is also informative. *Cellpose* accurately segments individual cells in low density regions, but suffers from oversegmentation errors in high density biofilm regions (**Figure 4.13e**). The Hartmann *et al*. algorithm provides reasonable estimates of cell positions in low and high density biofilm regions, but again struggles with cell shape estimation (**Figure 4.13d**, see also **Figure 4.8g-i**). On the other hand, the integrated *BCM3D* workflow (CNN + *LCuts*) produces biologically reasonable cell shapes regardless of cell density (**Figure 4.12**).

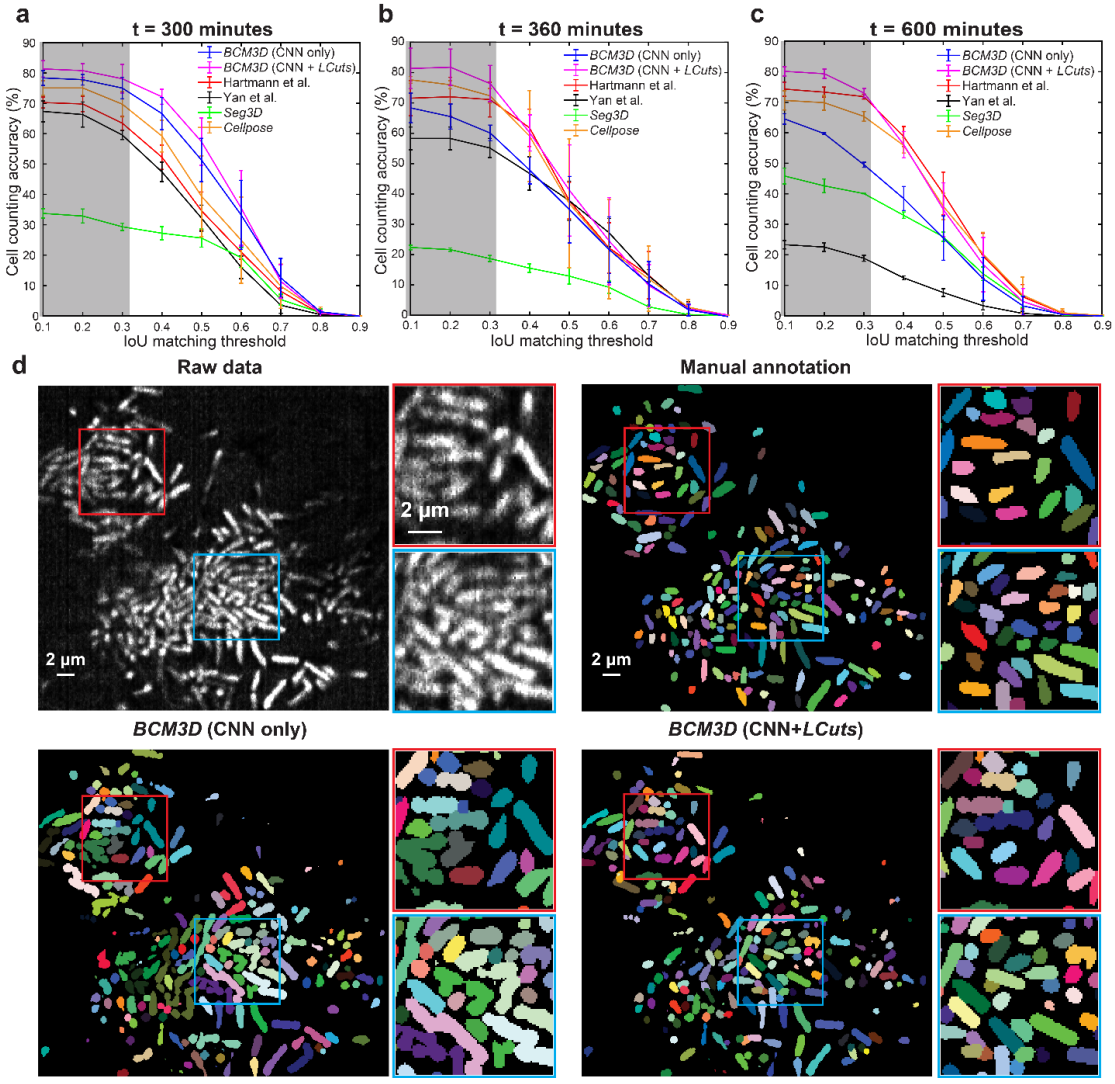


**Figure 4.12** Comparison of segmentation accuracies achieved by conventional segmentation approaches (Hartmann *et al.*, *Seg3D*, Yan *et al.*), *Cellpose*, and *BCM3D*. The estimated SBRs are 2.2, 1.8, and 1.3, respectively. The estimated cell densities are 54.8%, 59.0%, and 64.6%, respectively. (a-c) Three experimental *E. coli* datasets (cytosolic expression of GFP) acquired at different time points after inoculation of cells. Segmentation accuracy is parameterized in terms of cell counting accuracy (*y* axis) and IoU matching threshold (*x* axis). Each data point is the average of the cell counting accuracies calculated using annotation maps traced by $N = 3$ different researchers. Data are presented as mean values ± one standard deviation indicated by error bars. Curves approaching the upper right-hand corner indicate higher overall segmentation accuracy. (d)

Comparison of segmentation results achieved at the t= 600 minutes time point by manual annotation (shown is one of $N$ = 3 researchers' annotation result, the other two annotation results are shown in **Figure 4.13f** and **g**, and by BCM3D using *in silico*-trained CNNs only and after further refinement of CNN outputs using *LCuts*. Similar results were also obtained at the $t$ = 300 and $t$ = 360 minute time points. Segmentation results of the other methods are shown in **Figure 4.13**.

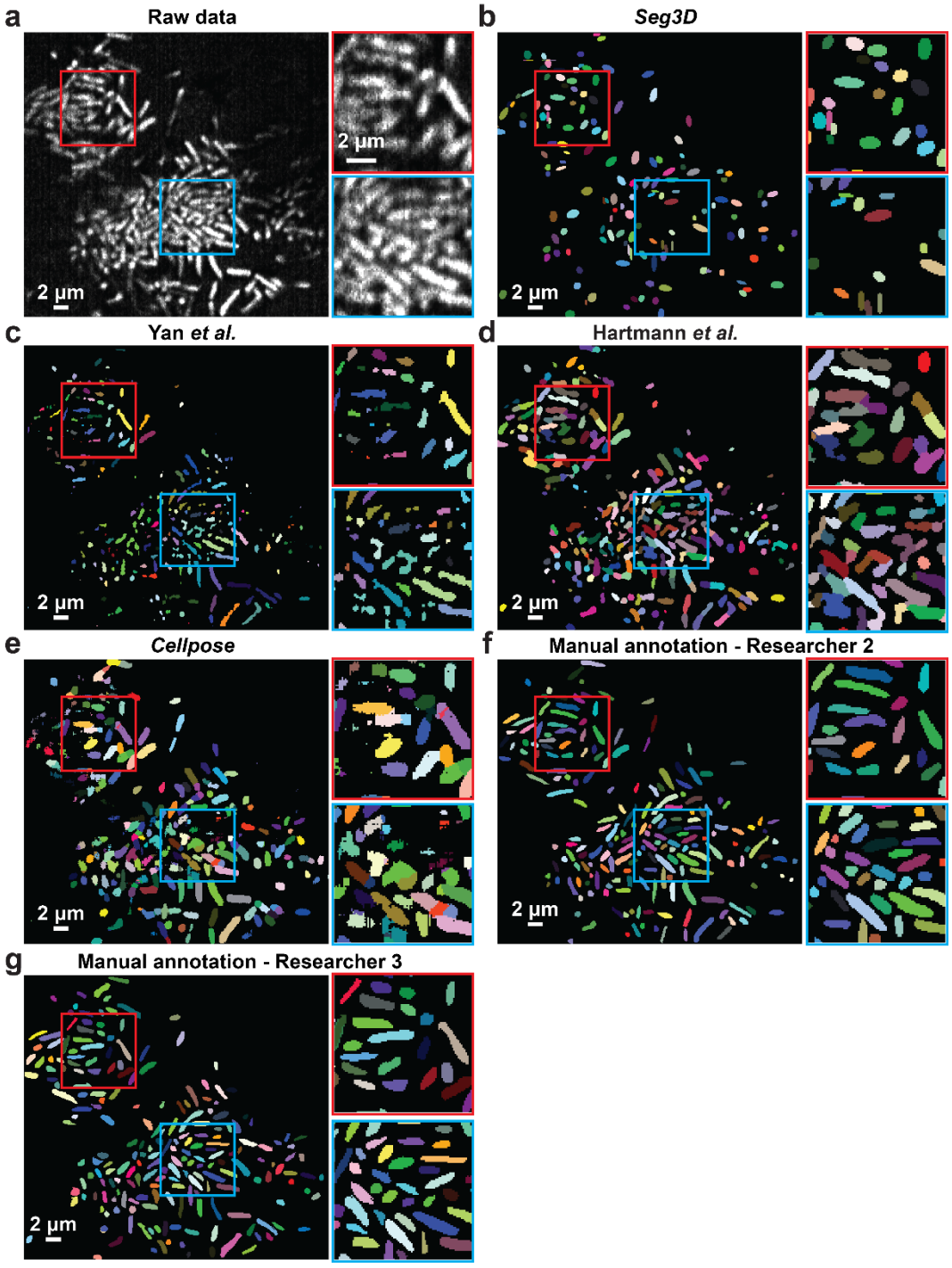


**Figure 4.13** Visual comparison of segmentation results achieved by previous segmentation approaches that rely solely on mathematical image processing. (a) Experimental dataset is the *E. coli* biofilm containing GFP expressing cells 10 hours after the inoculation. (b) Segmentation result obtained using *Seg3D* (275). (c) Segmentation result obtained using

the algorithm in Yan *et al.* (234). (d) Segmentation result obtained using Hartmann *et al.* (236). (e) Segmentation result obtained using *Cellpose* (246). (f) (g) manual annotation by two independent researchers.

We attribute the more rapid drop-off of the cell counting accuracy as a function of increasing IoU matching threshold in **Figure 4.12** to the following factors. First, human annotation of experimentally acquired biofilm images differs from the ground truth segmentation masks that are available for simulated data (**Figure 4.14**). The shape mismatches between algorithm segmented and manually annotated cell shapes (**Figure 4.14** and **4.15**) lead to a global lowering of voxel-level segmentation accuracy and thus a more rapid drop-off of the cell counting accuracy as a function of increasing IoU matching threshold. Because bacterial cell shapes are not accurately captured by manual annotation (**Figures 4.14**), cell counting accuracies referenced to manual annotations should be compared only at low IoU matching thresholds (0.1-0.3, shaded grey in **Figure 4.12a-c**), as also noted previously (271). We also note that bacterial cells in experimental images appear motion-blurred if they are only partially immobilized and therefore wiggle during image acquisition. Furthermore, optical aberrations and scattering effects were not included in training data simulations, which may decrease the performance of the CNNs on experimental data. Still, at IoU matching threshold < 0.3, the cell counting accuracy of *BCM3D* remains above 75% while also producing biologically reasonable cell shapes. Thus, the bacterial cell segmentation results of *BCM3D* represent a substantial improvement over other approaches (**Figure 4.12** and **Figure 4.13)**.

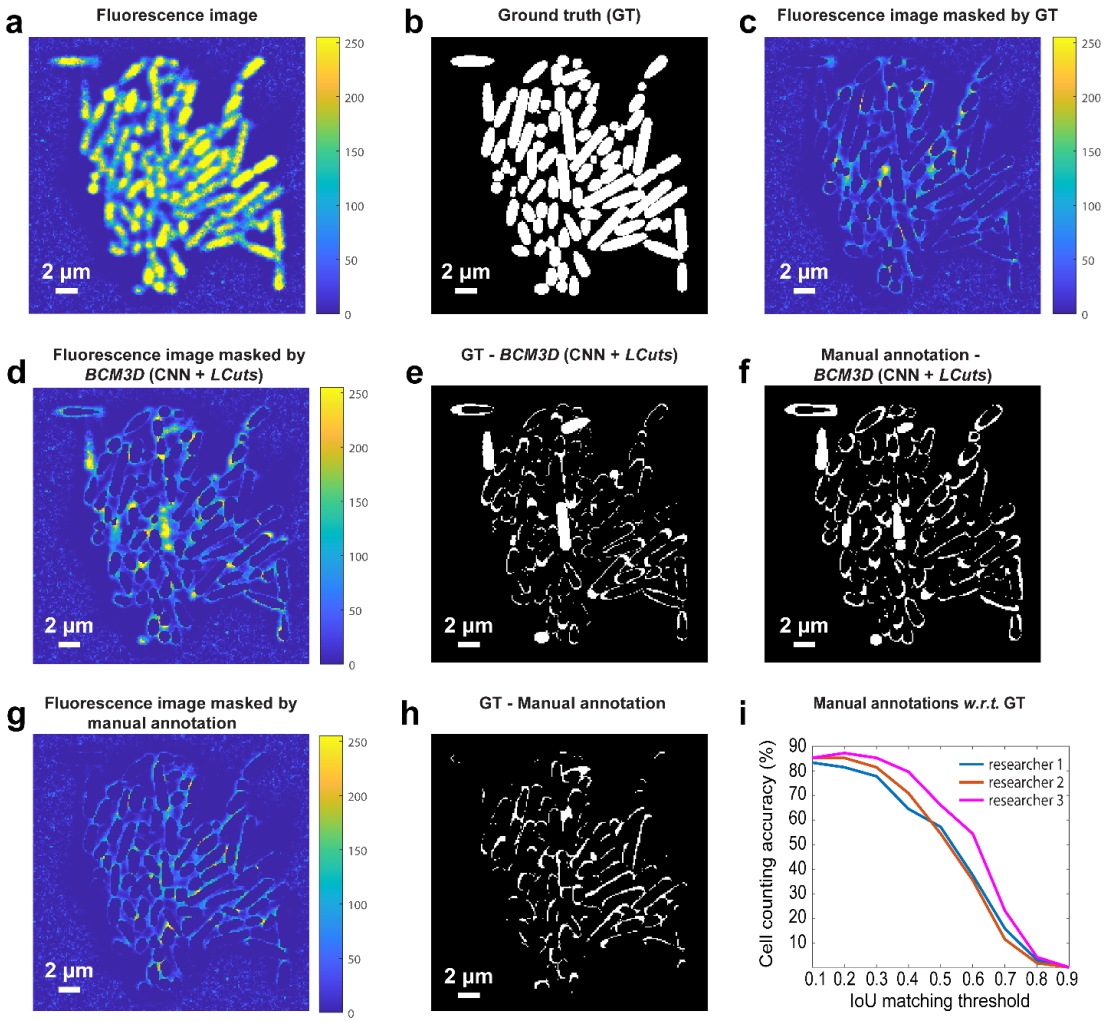


**Figure 4.14** (a) Fluorescence image slice of a 3D simulated biofilm and (b) the corresponding ground truth (GT). (c) The fluorescence image slice shown in (a) masked by its corresponding GT shown in (b). The fluorescence is not completely masked because of the diffraction-limited resolution of light microscopy. (d) Fluorescence image slice of the same simulated biofilm masked by the *BCM3D* segmentation result. (e) Absolute value of the difference image between the GT and the *BCM3D* segmentation result. White pixels indicate regions where the two masks do not agree. (f) Absolute value of the difference image between a manual annotated mask (from researcher 3) and the *BCM3D* segmentation result. (g) Fluorescence image slice of the same simulated biofilm masked by the manual annotation result. Researcher 3 chose to draw larger cell boundaries to mask more of the fluorescence intensity. (h) Absolute value of the difference image between the GT and the

manually annotated mask. White pixels indicate regions where the two masks do not agree. (I) Segmentation accuracy achieved by manual annotation performed by three different researchers. Segmentation accuracy is parameterized in terms of cell counting accuracy (*y* axis) and IoU matching threshold (*x* axis, a measure of cell shape estimation accuracy. Curves approaching the upper right-hand corner indicate higher overall segmentation accuracy with respect to the ground truth. While IoU matching thresholds <0.3 yield good cell counting accuracies, the cell counting accuracy sharply decreases for IoU matching thresholds >0.3, because manually annotated cell shapes differ from the ground truth cell shapes.

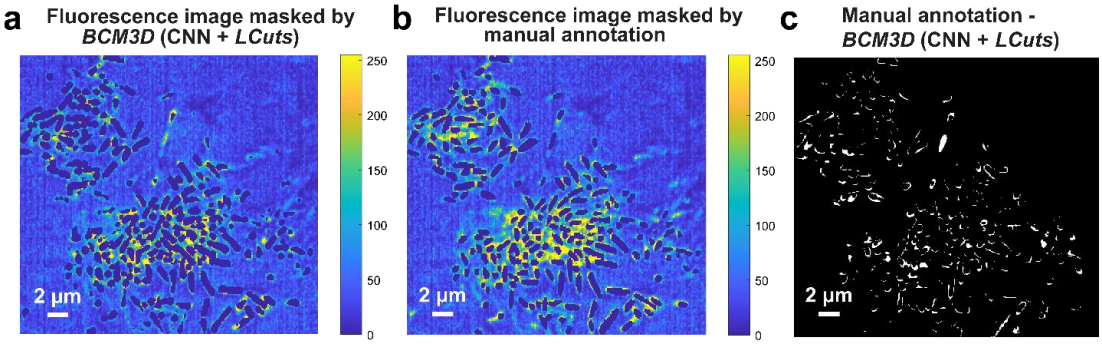


**Figure 4.15** (a) Fluorescence image slice of the 3D *E. coli* biofilm shown in Figure 5c masked by the BCM3D segmentation result. (b) Fluorescence image slice of the 3D *E. coli* biofilm shown in Figure 5c masked by manual annotation. (c) Absolute value of the difference image between manual annotation and BCM3D segmentation.

To demonstrate that *BCM3D* can achieve similarly high segmentation accuracies for membrane-stained cells in different cellular arrangements, we analyzed a small patch of a *M. xanthus* biofilm, which was stained with the membrane intercalating dye FM4-64 (**Figure 4.16**). In contrast to *E. coli* biofilms, the submerged *M. xanthus* biofilm imaged here features cells in a mesh-like arrangement with close cell-to-cell contacts, which presents a unique challenge for 3D single-cell segmentation. To obtain reference data for

3D segmentation accuracy determination, we manually annotated each *xy*, *xz*, and *yz* slice of an entire 3D image stack (**Figure 4.16b**). When referenced to this 3D manual segmentation result, *BCM3D* (**Figure 4.16c**) produced cell counting accuracies above 70% at low (0.1-0.3) IoU matching thresholds, whereas segmentation results obtained by conventional image processing (Hartmann *et al.*) and by generalist CNN-processing (*Cellpose*) produced cell counting accuracies <50% in the same IoU matching threshold region (**Figure 4.16d**). We note however that neither *Cellpose* nor the Hartmann *et al.* algorithm were specifically optimized/designed for segmenting membrane-stained cells. Indeed, the performance of *Cellpose* on this type of biofilm architecture is inferior to the results achieved using the *in silico*-trained CNNs of *BCM3D* alone (without using *LCuts* post-processing). One reason might be that the pre-trained, generalist *Cellpose* model has not been trained sufficiently on long, thin, and highly interlaced rod-shaped cells, such as those contained in a *M. xanthus* biofilm.

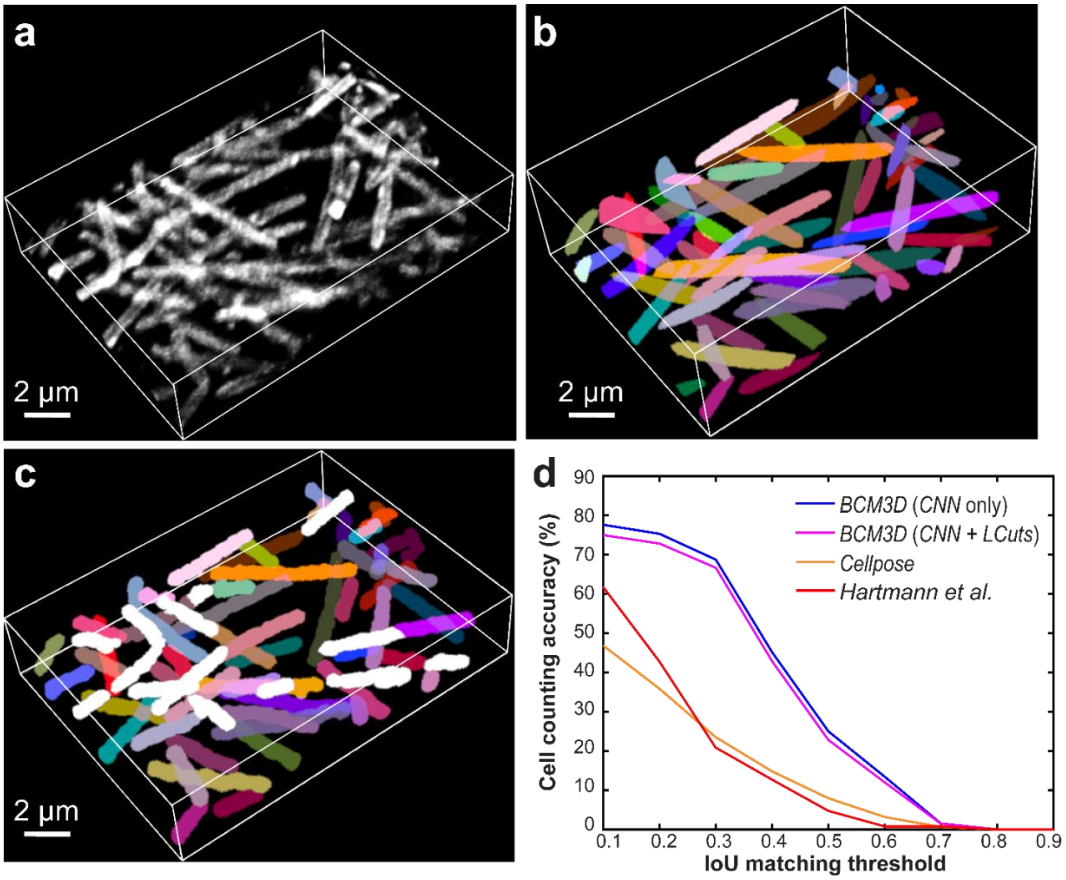


**Figure 4.16** 3D Segmentation accuracy evaluation using *M. xanthus* biofilm images (cell density = 36.2%, and SBR = 1.58) using *in silico*-trained CNN processing. (a) Maximum intensity projection of a 3D *M. xanthus* fluorescence image. Cells were labeled with membrane-intercalating dye, FM4-64. Similar images were obtained at $N$ = 120 different time points. (b) Maximum intensity projection of the manually obtained 3D segmentation result. (c) Maximum intensity projection of a CNN-based 3D segmentation result after *LCuts* post-processing. Cells that can be matched with the GT are displayed in the same colors as GT or otherwise colored in white. (d) Segmentation accuracy of compared algorithms parameterized in terms of cell counting accuracy ($y$ axis) and IoU matching threshold ($x$ axis).

### 4.4.5 Morphological Separation of Mixed Cell Populations

Given the improved segmentation results obtained using *BCM3D*, we reasoned that the same CNNs may have additional capacity to assign segmented objects to different cell types based on subtle morphological differences in the acquired images. Differences in the imaged cell morphologies arise due to physical differences in cell shapes (e.g. spherical vs. rod-shaped cells) or due to differences in the fluorescent labeling protocols (e.g. intracellular vs. cell membrane labeling), because fluorescence microscopes simply measure the spatial distributions of fluorophores in the sample. The ability to separate different cell morphologies is important for the study of multispecies biofilms, where interspecies cooperation and competition dictate population-level outcomes (46-53, 224). Separation of differentially labeled cells is also important for the study of gene activation in response to cell-to-cell signaling (278). Expression of cytosolic fluorescent proteins by transcriptional reporter strains is a widely-used technique to visualize activation of a specific gene or genetic pathway in living cells. Such genetic labeling approaches can be complemented by chemical labeling approaches, e.g. using membrane intercalating chemical dyes that help visualize cells non-specifically or environmentally-sensitive membrane dyes that provide physiological information, including membrane composition (279, 280), membrane organization and integrity (281-283), and membrane potential (284, 285). Chemical and genetic labeling approaches are traditionally implemented in two different color channels. However, there are important drawbacks to using multiple colors. First and foremost, the amount of excitation light delivered is increased by the necessity to excite differently colored fluorophores, raising phototoxicity and photobleaching concerns.

Second, it takes *N* times as along to acquire *N*-color images (unless different color channels can be acquired simultaneously), making it challenging to achieve high temporal sampling in time-lapse acquisition. For these reasons, methods that extract complementary physiological information from a single-color image are preferable.

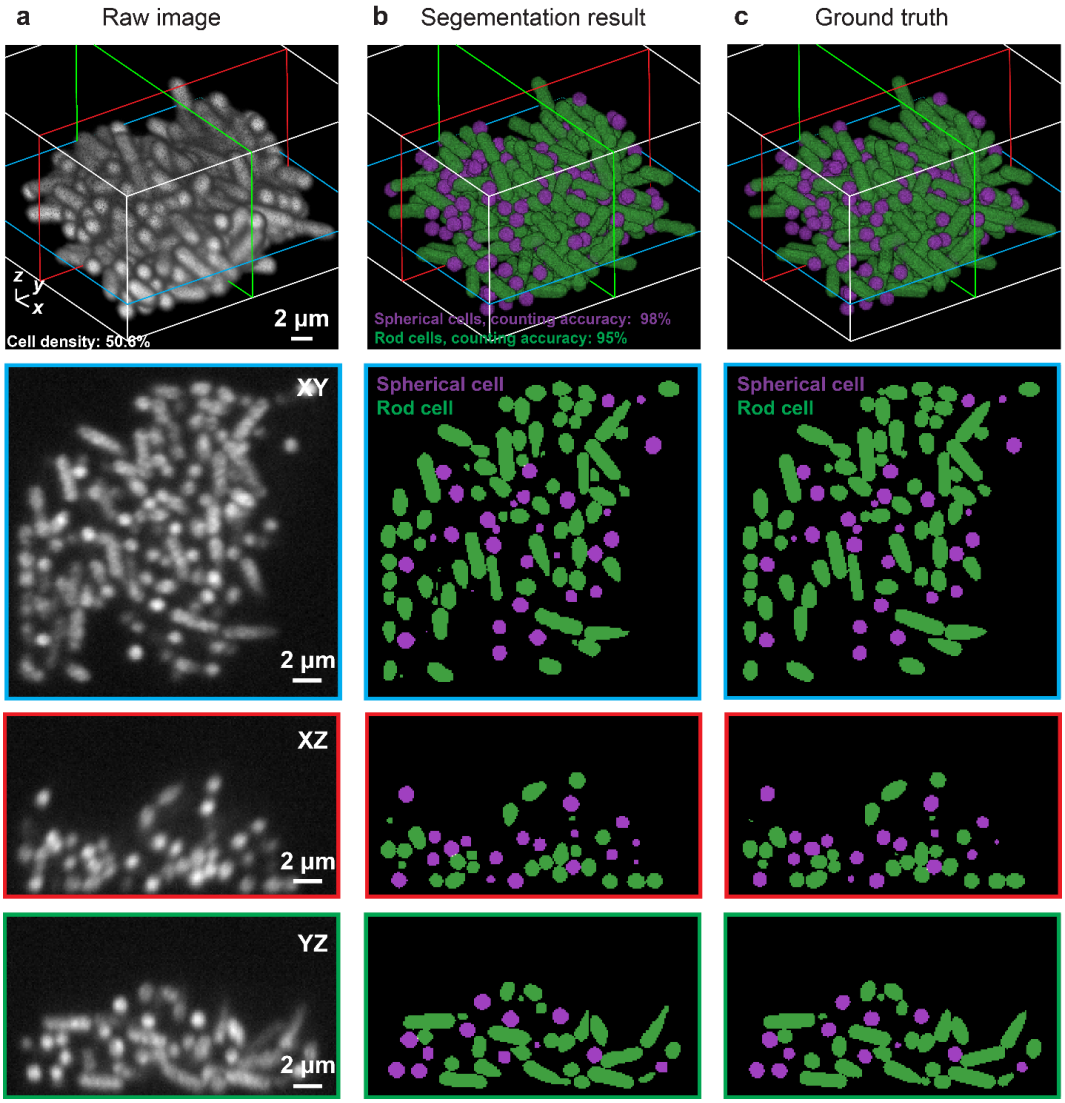


**Figure 4.17** Segmentation of mixed population biofilms containing spherical cells and rod-shaped cells. (a) Simulated fluorescence image of a mixture of spherical cells and rod-shaped cells. The mixing ratio for this particular biofilm is 50:50, the cell density is 50.6%,

and the SBR is 2.56. (b) Segmentation result obtained by *BCM3D* and (c) ground truth. Three orthogonal planes are shown below each 3D image.

We evaluated the ability of *BCM3D* to automatically segment and identify rod-shaped and spherical bacterial cells consistent with shapes of *E. coli* and *S. aureus* in simulated images (**Figure 4.17**). To segment cells in two-population biofilms, we trained CNNs that classify pixels into five different classes: 'background', 'cell interior of population 1', 'cell boundary of population 1', 'cell interior of population 2' and 'cell boundary of population 2'. Thresholding the CNNs confidence maps can achieve cell counting accuracies larger than 90% for both cell types independent of their population fractions (**Figure 4.18a**). Post-processing of this result using *LCuts* improved the cell counting accuracy by less than 0.5% on average, indicating that under-segmented cell clusters are not prevalent in this dataset.

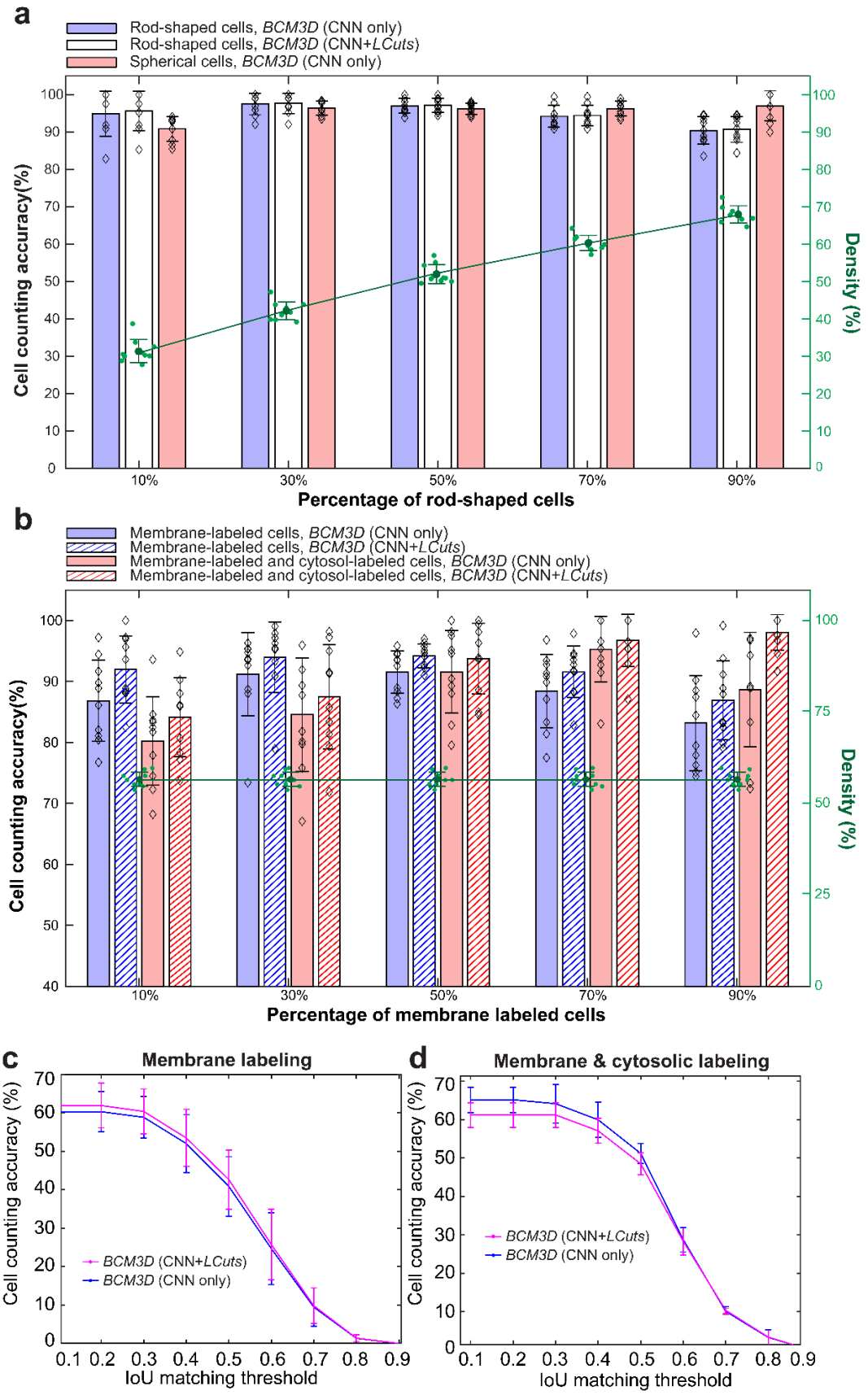
a
Rod-shaped cells, BCM3D (CNN only)
Rod-shaped cells, BCM3D (CNN+LCuts)
Spherical cells, BCM3D (CNN only)
Cell counting accuracy(%)
Density (%)
10%
30%
50%
70%
90%
Percentage of rod-shaped cells
b
Membrane-labeled cells, BCM3D (CNN only)
Membrane-labeled cells, BCM3D (CNN+LCuts)
Membrane-labeled and cytosol-labeled cells, BCM3D (CNN only)
Membrane-labeled and cytosol-labeled cells, BCM3D (CNN+LCuts)
Cell counting accuracy(%)
Density (%)
Percentage of membrane labeled cells
c
Membrane labeling
d
Membrane & cytosolic labeling
Cell counting accuracy (%)
BCM3D (CNN+LCuts)
BCM3D (CNN only)
IoU matching threshold

**Figure 4.18** Performance of *BCM3D* on mixed-population biofilm images. (a) Cell counting accuracy of *BCM3D* on simulated images containing different ratios of rod-shaped and spherical cells. Black diamonds represent the counting accuracy for $N = 10$ independently simulated datasets. Green dots represent the cell density for each independent dataset. Error bars represent ± one standard deviation. (b) Cell counting accuracy of *BCM3D* on simulated images with different ratios of membrane-labeled, and membrane-labeled and interior fluorescent protein expressing cells. Black diamonds represent the counting accuracy for $N = 10$ independently simulated datasets. Green dots represent the cell density for $N = 10$ independent datasets. Error bars represent ± one standard deviation. (c and d) Cell counting accuracy of *BCM3D* on experimental images of (c) membrane-labeled, and (d) membrane-labeled and interior fluorescent protein expressing *E. coli* cells (mixing ratio ~ 1:1). Each data point is the average of the cell counting accuracies calculated using annotation maps traced by three different researchers ($N = 3$). Data are presented as mean values ± one standard deviation indicated by error bars.

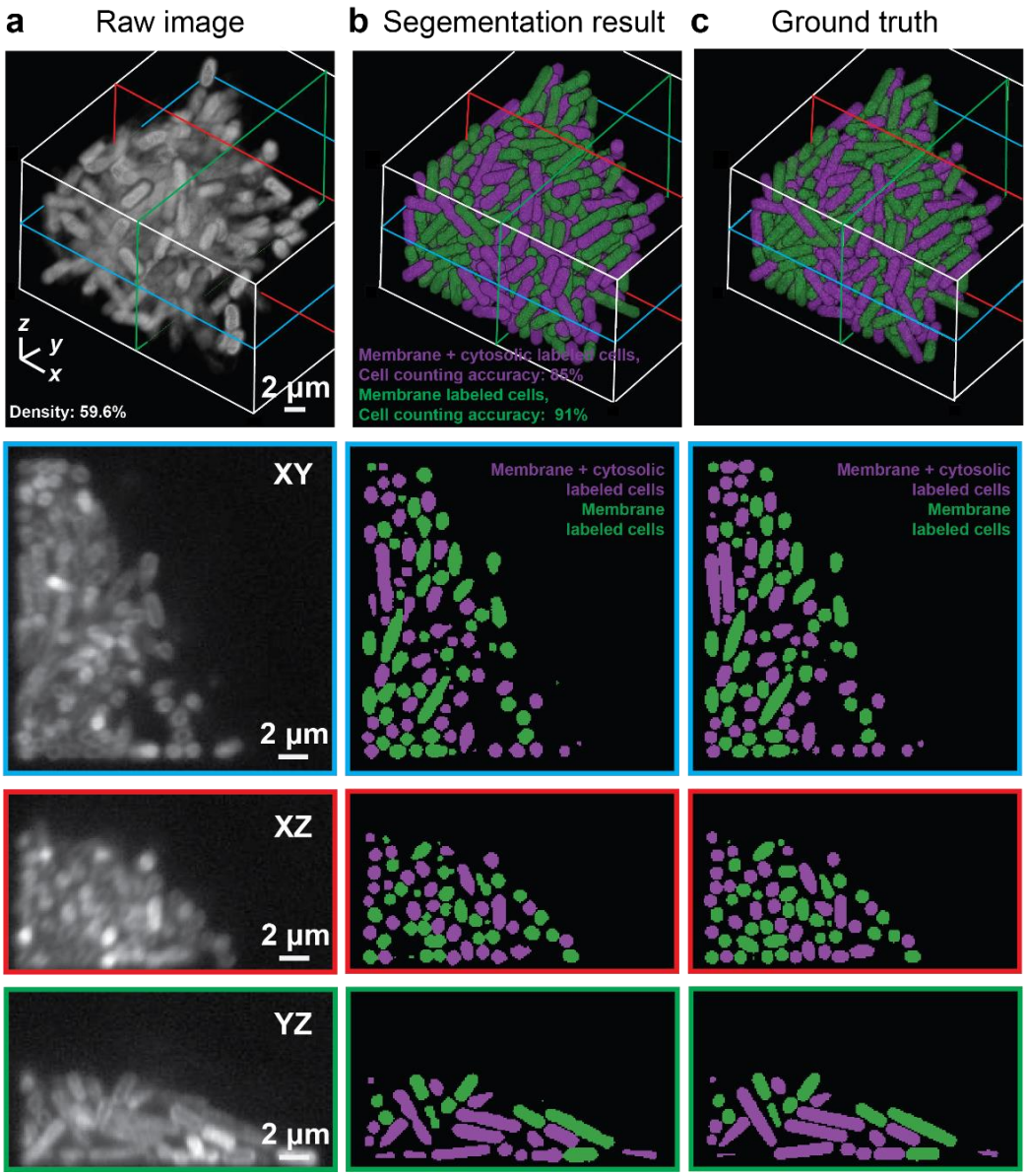


**Figure 4.19** Segmentation of mixed population biofilms containing membrane-stained cells and membrane-stained cells that additionally express an intracellular fluorescent protein. (a) Simulated fluorescence image of a mixture of membrane-stained cells and membrane-stained cells that additionally express an intracellular fluorescent protein. The mixing ratio for this particular biofilm is 50:50, the cell density is 59.6%, and the SBR is 2.56. (b) Segmentation result obtained by *BCM3D* and (c) ground truth. Three orthogonal planes are shown below each 3D image.

We next evaluated the ability of *BCM3D* to automatically segment and separate membrane-stained cells that express cytosolic fluorescent proteins from those that do not (**Figure 4.19**). Again, the cell counting accuracy is consistently above 80% for all tested mixing ratios (**Figure 4.18b**). Finally, we applied *BCM3D* to experimentally acquired biofilm images of two different *E. coli* strains. Both strains were stained by the membrane intercalating dye FM4-64, but the second strain additionally expressed GFP (**Figure 4.20**). The cells were homogeneously mixed prior to mounting to randomize the spatial distribution of different cell types in the biofilm (see Materials and Methods). Multiple 2D slices from the 3D image stack were manually annotated and compared with the results obtained by *BCM3D*. Consistent with the single-species experimental data, a cell counting accuracy of 50% is achieved for each cell type at a 0.5 IoU matching threshold and, at lower IoU matching thresholds, the counting accuracies increased to 60% to 70%, (**Figure 4.18c** and **d**). Thus, using appropriately trained CNNs in *BCM3D* enables automated and accurate cell type assignments based on subtle differences in cell morphologies in mixed population biofilms – a capability not available using conventional image processing methods.

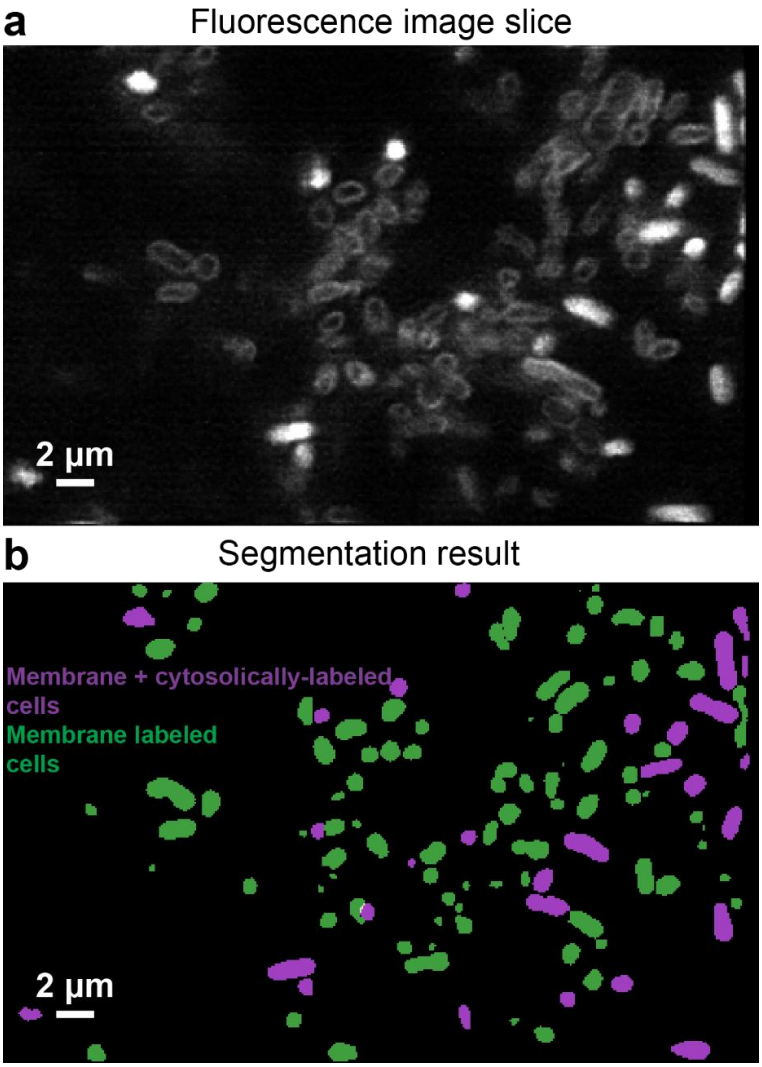


**Figure 4.20** (a) Experimental 2D slice of a mixed *E. coli* population containing membrane-stained cells and membrane-stained cells that additionally express an intracellular fluorescent protein. The mixing ratio at the time of inoculation was 50:50. All cells were labeled by the FM4-64 membrane-intercalating dye. (b) *BCM3D* segmentation result corresponding to the image shown in (a). Membrane-stained cells are displayed in green, and cells that were both membrane-stained and cytosolically-labeled are displayed in magenta.

## 4.5 Conclusions

CNNs have been successful applied to many different problems in biological image analysis, but their ability to segment individual cells in 3D and time-lapse 3D bacterial biofilm images has not yet been fully explored. Here, we demonstrated a new CNN-based image analysis workflow, termed *BCM3D*, for single-cell segmentation and shape classification (morphometry) in 3D images of bacterial biofilms. In this work, we applied *BCM3D* to 3D images acquired by lattice light sheet microscopy. However, *BCM3D* readily generalizes to 3D images acquired by confocal microscopy or advanced super-resolution microscopy modalities, provided that realistic image formation models are used to simulate the training datasets. The use of simulated training data is a major advantage of *BCM3D*, because it overcomes inconsistencies inherent in manual dataset annotation (**Figure 4.14** and **4.15**) and thus solves the problem of obtaining sufficient amounts of accurately annotated 3D image data. The ability to use simulated training data provides needed flexibility not only in terms of the microscope platform used for imaging, but also in terms of the bacterial cell shapes that are to be segmented.

We systematically investigated the advantages and limitations of *BCM3D* by evaluating both voxel- and cell-level segmentation accuracies using simulated and experimental datasets of different cell densities and SBRs. *BCM3D* enabled accurate segmentation of individual cells in crowded environments and automatic assignments of individual cells to specific cell populations for most of the tested parameter space. Such capabilities are not readily available when using previously established segmentation methods that rely exclusively on conventional image and signal processing algorithms.

While *BCM3D* surpasses the performance of previous approaches, we stress that further improvements are possible and, for long-term, high frame-rate time-lapse imaging experiments, absolutely needed. Our systematic analysis revealed that high cell density and low SBR datasets are particularly challenging for the CNNs used in this work. Future work will therefore focus on increasing the contrast and resolution in bacterial biofilm images. While, the use of optical super-resolution modalities can provide higher spatial resolution, such resolution improvements often come at a cost of reduced image contrast and faster photobleaching/phototoxicity. Software solutions that can process images with limited resolution and low SBRs will therefore play a tremendously important role in biological imaging. *BCM3D* is a general workflow that integrates computational simulation of training data, *in silico*-training of CNNs for a specific task or a specific cell type, and mathematical post-processing of the CNN outputs. Incorporating different training strategies and different CNNs, such as the generalist CNN used in *Cellpose* (246), into the *BCM3D* workflow will enable automated cross-validation of segmentation results when a ground truth or manual annotation map is not available. Furthermore, CNN-based image processing modules developed for contrast enhancement and denoising have also surpassed the performance of conventional methods based on mathematical signal processing (286-289). Incorporating these tools into the *BCM3D* workflow promises to further improve the single-cell segmentation accuracies. We anticipate that the ability to accurately identify and delineate individual cells in dense 3D biofilms will enable accurate cell tracking over long periods of time. Detailed measurements of behavioral single-cell phenotypes in larger bacterial communities will help determine how macroscopic biofilm properties, such as its

mechanical cohesion/adhesion and its biochemical metabolism, emerge from the collective actions of individual bacteria.

# Chapter 5: Single Cell Dynamics in Shigella Biofilms

## 5.1 Abstract

The individual cell behaviors in living *S. flexneri* biofilms have not yet been explored. The non-invasive imaging technique, LLSM and the accurate cell segmentation modality, *BCM3D*, enable inspecting live bacterial biofilms with subcellular resolution. However, to study individual cell behaviors in biofilms, an accurate cell tracking method is needed. In this work, we present a multi-cell tracking algorithm which tracks cells with the highest similarity by considering cell observables, including cell positions, cell orientations, cell shapes, cell volumes and fluorescence intensities. We evaluated the tracking accuracy of the algorithm with simulated biofilm data and found a linear relationship between the tracking accuracy and the cell counting accuracy. Aiming to reveal the single cell dynamics in *S. flexneri* biofilms, we applied LLSM, *BCM3D* and the newly developed tracking algorithm to study the biofilm of this pathogenic bacterium. We uncovered the fast diffusion behaviors of *S. flexneri* cells in the biofilm. Finally, we present the capacity to calculate the growth rate of single *S. flexneri* cells within a 3D biofilm.

## 5.2 Introduction

*Shigella flexneri*, an intracellular bacterial pathogen, can cause bacillary dysentery by invading epithelial cells in the colonic mucosa (34, 186-188). As a highly infectious agent, ingestion of as few as 10 to 100 *S. flexneri* cells are sufficient to result in an infection. After ingestion, the surviving and spreading of *S. flexneri* is challenged by several environmental conditions within the epithelial lining of the gut, such as host production of antimicrobial peptides, proteases, and bile salts (189). Among these reagents, the influences of bile salts have been widely investigated. The antimicrobial activities of bile salts are due to their amphipathic structures which provide detergent-like properties (190, 191). Previous research revealed that bile salts modulate the interaction between *Shigella* species and its environment (33). Pope *et al.* first reported that growing in the presence of bile salt, deoxycholate (DOC), enhanced the adhesion of *S. flexneri* and *S. dysenteriae* to HeLa cells (192). In addition to increase the adhesion to host cells, Ellafi *et al*. found that the cell size of *Shigella* species decreases after having been exposed to bile salts (33). *Shigella* spp. was not expected to form biofilms, since they do not express canonical adhesins, curli, or flagella, which are common components of biofilms formed by other species (290, 291). However, Nickerson *et al.* recently reported that exposure to a mixture of DOC and cholate (CA) stimulates *Shigella* spp. to form biofilms (38).

Due to the lack of flagellum expression, the intra- and inter- cell spread of *Shigella* spp. are accomplished by actin-based motility with the help of *IcsA*, an out membrane protein which localizes on a single pole of the cell (31, 32, 37). In addition to driving the spread of *Shigella* cells, Brotcke Zumsteg *et al.* found that *IcsA* is a necessary adhesin to

promote contact with host cells (31). Very recently, Koseoglu *et al.* reported that *IcsA* is critical for bile salt-mediated biofilm formation of *Shigella* (36).

None of the above-mentioned studies on *S. flexneri* biofilms are performed *in vivo* with single cell resolution. Only bulk information of biofilms, such as the total biomass and the thickness, are provided. The dynamics of *S. flexneri* biofilms and the single cells within it are still poorly understood. Tracking the individual cell behaviors in *S. flexneri* biofilms could help develop strategies for eliminating *S. flexneri* biofilms and preventing the spread of this pathogenic strain. Therefore, in this work, our goal is to obtain a clear picture of single cell dynamics in *S. flexneri* biofilms.

Quantitatively tracking cells within *S. flexneri* biofilms requires a suitable imaging approach with sufficient resolution, an automated cell segmentation method, a compatible biofilm formation device for the pathogenic species and a reliable cell tracking algorithm. As presented in Chapter 4, LLSM enables non-invasive imaging for biofilms and *BCM3D* (183), an image analysis workflow that combines deep learning with mathematical image analysis, enables accurate segmentation and classification of single bacterial cells in 3D fluorescence images. In Chapter 3, we designed a flow chamber system which is compatible with LLSM and allows real-time monitoring of biofilm formation for pathogenic species, such as *S. flexneri*. These imaging and cell segmentation approaches provide the data for quantitative cell tracking. However, a reliable multi-cell tracking method for dense 3D biofilms is still not available.

The existing cell tracking methods can be broadly categorized into two main types: tracking by detection and tracking by model evolution (292-302). The first type involves two steps: 1) independently segmenting all target objects in all the frames of the entire

time-lapse data sets and 2) associating detected objects between frames, typically by optimizing a probabilistic objective function (303). In contrast, the second category accomplishes segmentation and tracking simultaneously by evolution of an explicitly or implicit defined curves or surfaces (303, 304). Recently, the application of machine learning techniques for both segmentation and tracking algorithms has been widely used and achieved great success (171, 174, 246, 260, 305-307). However, robust tracking methods for multi-cell tracking in dense 3D biofilms have not yet been reported.

Multi-cell tracking in dense 3D biofilms is challenging because bacterial cells have similar morphometries and are closely packed. Cells can disappear and re-appear during imaging due to their fast wiggling. To minimize the impact of these issues on tracking, conventional tracking approaches for 3D bacterial biofilms often requires high frame rate imaging (134) or multicolor labeling (185) imaging. High frame rate imaging and multicolor imaging can both result in increased photodamage, especially for long-term experiments. However, high frame rate might be not experimentally achievable because of the large size (e. g. 50 by 50 μm) of the field of view (FOV) for imaging a biofilm, high frame rate might be not experimentally achievable.

Conventional tracking approaches for 3D bacterial biofilms are often developed based on segmentation results with low accuracies due to the low quality of the biofilm images. Precise single-cell observables, including cell positions, cell orientations, cell shapes, cell volumes and fluorescence intensities, are not available from these segmentation results with low accuracies. LLSM can provide 3D biofilm images with high quality, such as high resolution and high signal to background ratios (SBRs). In addition, *BCM3D* (183), one of the state of the art image analysis workflow, can provide accurate

segmentation of single bacterial cells in 3D fluorescence images. The precise single-cell observables, including cell positions, orientations, shapes, volumes and fluorescence intensities, can be obtained from the accurate segmentation results. In this work, aiming to address the challenges associated with multi-cell tracking in crowded biofilms, we developed a bacterial cell tracking algorithm that leverages correlations among the above-mentioned single-cell observables. The cell lineage is also determined by using observables, i.e. cell positions, length and volumes. By systematically evaluating the performance of the tracking algorithm with simulated biofilm data for a range of SBRs and cell densities, we found that the tracking accuracy improves linearly with the cell counting accuracy. We also compared the tracking accuracy of the tracking algorithm using the Hungarian algorithm (308) or the nearest neighbor algorithm to associate cells with the simulated biofilm data. We found the nearest neighbor algorithm provided higher tracking accuracy, and was therefore chosen for associating cells when processing experimental data. The tracking algorithm was then applied to investigate the dynamic events of single cells in *S. flexneri* biofilms. The diffusion coefficients and moving rates of single cells in the biofilm were calculated based on the trajectories. Our results showed that *S. flexneri* cells have larger diffusion coefficients and moving rates than the wild type *E. coli* strain, a classical model to study biofilms. The cell density of *S. flexneri* biofilms was then calculated and compared with that of *E. coli*. The much lower cell density is the likely reason why *S. flexneri* cells in the biofilm have larger diffusion coefficients.

The work in this chapter provides methodologies for studying individual cell behaviors in *S. flexneri* biofilms. This work sheds light on interpreting the emergent properties of *S. flexneri* biofilms in terms of the fully-resolved behavioral phenotypes of

individual cells. These studies could provide valuable insight into understanding the spread of *S. flexneri*, a pathogenic strain.

## 5.3 Materials and Methods

**Bacterial Strains and Growth Conditions:**

The wild-type *S. flexneri* 2457T strain was used in this study (309). The strain was labeled with fluorescent protein mCherry. The bacteria were grown overnight at 37 degrees in tryptic soy broth (TSB). Spectinomycin (100 μg/ml) was added into the media to maintain the pMMB-mCherry vector for constitutive mCherry expression. Before inoculating into the flow chamber system, the overnight culture was diluted 100 times into the same culture medium and grown to an optical density at 600 nm (OD600) of 0.6 – 1.0.

Ampicillin resistant *E.coli* K12, constitutively expressing GFP (249), were cultured at 37 degrees overnight in LB medium with 100 μg/ml ampicillin. Overnight cultures were diluted 100 times into the same culture medium and grown to an OD600 of 0.6 – 1.0. Before inoculation, the cell culture was diluted by a factor of 10.

**Biofilm Formation and Imaging:**

Cell culture was inoculated into the home-built flow chamber system (Chapter 3). Cropped glass coverslip was mounted inside the flow channel as the substrate for biofilm formation. After inoculation, cells were allowed to settle to the flow channel and adhere to the coverslip for 1 hour at room temperature. For *S. flexneri* biofilm formation, the flow chamber system was filled with 25% TSB media containing 0.4% (w/w) bile salts and 100

μg/ml spectinomycin. For *E. coli* biofilm formation, the flow chamber system was filled with M9 medium containing 100 μg/ml ampicillin. The flow rate for all experiments was 0.2 mL/hour. To keep the growth media fresh, the media was replaced every 24 hours.

Fluorescence images of bacterial biofilms were acquired on a home-built lattice light sheet microscope (LLSM). Here, a continuous illumination light sheet was produced by a time-averaged (dithered), square lattice pattern (137), and the illumination intensity at the sample was <1 W/cm$^2$. The sample-basin of LLSM was filled with sucrose solution. To minimize the aberration induced by refractive index mismatch, the concentration of the sucrose solution was adjusted to match the refractive index of the growth media (25% TSB: 1.3338, M9: 1.3352) inside the flow channel. The *S. flexneri* mCherry strain was excited using the 560 nm light sheet, while the *E. coli* GFP strain was excited using the 488 nm light sheet. The sample-basin was warmed to 37 degrees. *S. flexneri* biofilm images were acquired every second for a total of 200 time points. At each time point, a single 3D image stack contained 400 images were acquired with a 10 ms exposure time to avoid motion blur. The step size to acquire 400 frames of images was 200 nm. *E. coli* biofilm images were acquired every second for a total of 400 time points. At each time point, a single 3D image stack contained 200 images were acquired with a 10 ms exposure time. The step size to acquire 200 frames of images was 300 nm.

**Raw Data Processing:**

Raw data processing was accomplished by using the same procedure as described in Chapter 4.3.2 Raw Data Processing, which includes deskewing and deconvolution.

**Generating Simulated Biofilm:**

To generate data for evaluating the tracking algorithm, we computationally simulated a series of fluorescence images of 3D biofilms to mimic the biofilm development. The simulation was accomplished by using the same procedure as descripted in Chapter 4.3.3 Generation of Simulated Biofilm Images. Four time lapse datasets were simulated with different SBRs and cell densities. Each datasets contains 23 time points.

In the simulated datasets, spatial arrangements among individual cells, trajectories of each cell and the lineage relationships among cells are known precisely and accurately at each time point. The tracks and the lineage relationships were used as the ground truth to evaluate our tracking algorithm.

**Bacterial Cell Segmentation and Tracking:**

Precise cell segmentation was accomplished with *BCM3D* (183). The pre-trained model for processing *E. coli* biofilms were applied to inference cells in the convolutional neural network module of *BCM3D* (183).

In order to match cells between different time points, we first define a pairwise similarity function to weigh similarities among single-cells. The function is composed by five separate terms. These terms respectively quantify differences in cell position ($P$), cell orientation $\vartheta$, cell shape ($S$), cell volume ($V$) and cellular fluorescence intensity ($I$). If $A$ represents the cell-of-interest at time $t$ and $B$ represents a candidate cell to match at time $t$+1, then $T(P_A,P_B)$ is the Euclidean center-of-mass distance between the two cells, $R(\vartheta(A), \vartheta(B))$ is the difference in their relative orientation, $V(V_A, V_B)$ is their volume difference, $S(S_A, S_B)$ is the difference of their aspect ratio (the ratio of the major axis to the minor axis),

and $D_i(I_A,I_B)$ is their intensity dissimilarity between the two cells. With these definitions in hand, we define the pairwise similarity between two cells as:

$$f_{AB} = \lambda_1 * e^{-T(P_A,P_B)} + \lambda_2 * e^{-R(\vartheta_A,\vartheta_B)} + \lambda_3 * e^{-V(V_A,V_B)} + \lambda_4 * e^{-S(S_A,S_B)} + \lambda_5 * e^{-D_i(I_A,I_B)} + Reg(\lambda_1,\lambda_2,\lambda_3,\lambda_4,\lambda_5) \quad (5.1)$$

where $\lambda_1,\lambda_2,\lambda_3,\lambda_4,\lambda_5$ are weighting coefficients defining the relative importance of individual terms, and *Reg()* is the regularization of the weighting coefficients, which ensures that $f_{AB}$ takes on values between 0 (no similarity) and 1 (perfect similarity). We assume that matching the same cell in subsequent time frames maximizes $f_{AB}$ with respect to all other possible matches. In this work, $\lambda_1,\lambda_2,\lambda_3,\lambda_4,\lambda_5$ are empirically set as 0.7, 0.05, 0.1, 0.1, and 0.05, respectively. We consider linking the same cells across two different time points as a one-to-one assignment problem. We utilized both the Hungarian algorithm (310) and the nearest neighbor algorithm to solve the assignment problem (311). When applied iteratively over consecutive time frames (i.e. 1→2, 2→3, 3→4…), the algorithms determine the bacterial motion trajectories that minimize differences in cell positions, orientations, shapes, volumes and fluorescence intensities. The difference between the Hungarian algorithm and the nearest neighbor algorithm is the following. The Hungarian algorithm considers all possible one-to-one matches between segmented cells and then determines the set of matches that maximize the sum $\sum f_{AB}$ (minimize the difference). That is to say the Hungarian algorithm finds the globally optimal solution for matching. The nearest neighbor algorithm will simply match the two closest points amongst the two sets. That also means the nearest neighbor algorithm finds locally optimal solution for matching.

To set rational thresholds for each cell observable when associating cells, we manually tracked 10 pairs of cells between adjacent time points datasets. The differences of cell positions, orientations, shapes, volumes and fluorescence intensities for these 10 pairs of cells were calculated and averaged, respectively. The threshold for each observable was set by added a buffer of 25 % to the averaged value.

After obtaining tracks for all cells, the lineage relationships is determined by the following procedure. For a track A, assume it starts from time point t ($t \geq 2$) and its first cell is $C_A^{t1}$. Check all cells before time point t. A cell is assigned as the parent cell for $C_A^{t1}$ if it can satisfy three conditions: it is within a distance of 3 times of the cell length, its length and volume are 1.5 time of that of $C_A^{t1}$. Then, the tracks $C_A^{t1}$ belongs to will be split by $C_A^{t1}$ to form two new tracks.

**Evaluation of Cell Counting Accuracy:**

The same metric as descripted in Chapter 4.3.7 Performance Evaluation is used to measure the cell counting accuracy. To evaluate the accuracy of cell segmentation on experimental data, we traced the cell contours on experimental 2D slices by using freehand selections in Fiji ROI Manger (259).

**Evaluation of Tracking Accuracy:**

We use the widely accepted (244) Acyclic Oriented Graph Matching (AOGM) metric, which uniquely quantifies tracking accuracy (TRA) (312). The AOGM metric assesses how difficult it is to transform an experimental tracking result (in the form of a mathematical graph) into the reference result (a graph obtained from ground truth

trajectories or from accurately and independently determined experimental trajectories). The normalized version of the AOGM measure (312) is finally calculated by:

$$\mathrm{TRA} = 1 - \frac{\min(AOGM, AOGM_0)}{AOGM_0} \tag{5.2}$$

where $\mathrm{AOGM}_0$ is the AOGM value required for constructing the reference graph from empty tracking results. The tracking accuracy would be negative when the AOGM value is larger than $\mathrm{AOGM}_0$. The negative tracking accuracy makes no sense; therefore, the minimum operator is added in the numerator to prevent it from having a final negative value. TRA always falls in the [0, 1] interval with this operation. The higher TRA values corresponds to better tracking performance.

**Tracking Analysis:**

The Mean Squared Displacement (MSD) is calculated according to:

$$MSD_n = \frac{1}{N-n}\sum_{i=1}^{N-n}(x_{i+n} - x_i)^2,\ n = 1, \dots, N-1 \tag{5.3}$$

using all available displacements of a given duration $n\Delta t$. $\Delta t$ is the is the time between adjacent time points. $N$ is the total number of time points. $x_i$ is the position of the cell at time point $i$. $x_{i+n}$ is the position of the cell at time point $i+n\Delta t$. Only trajectories with at least 4 localizations were considered for the calculation of MSD and further analysis.

When the delay time for calculating MSD is $\Delta t$, the formula is simplified to:

$$MSD = \frac{1}{N-1}\sum_{i=1}^{N-1}(x_{i+1} - x_i)^2 \tag{5.4}$$

The apparent diffusion coefficient, $D^*$ is then computed as:

$$D^* = \frac{MSD}{2 \cdot d \cdot \Delta t} \tag{5.5}$$

where $N$ is the total number of time points and $x_i$ is the position of the cell at time point $i$. It must be noted that the so-estimated apparent diffusion coefficients do not take into account the static and dynamic localization errors (313), or the effect of confinement.

The moving rate of one cell is calculated by:

$$V = \frac{1}{(N-1)\cdot\Delta t}\sum_{i=1}^{N-1}\sqrt{(x_{i+1}-x_i)^2 + (y_{i+1}-y_i)^2 + (z_{i+1}-z_i)^2} \quad (5.6)$$

where $N$ is the total number of time points and ($x_i$, $y_i$, $z_i$) is the position of the cell at time point $i$.

**Density Calculation:**

To estimate the density of the biofilm, we manually partitioned the segmentation results into several 3D tiles of size 64 by 64 by 8 voxels. We then estimated the local density as total cell volume contained in each tile divided by the tile volume. We calculated the mean density of the 10 densest tiles to define the density of the biofilm.

## 5.4 Results and Discussion

### 5.4.1 Additional Cell Observables Improve the Tracking Accuracy

Distance between cells is conventionally only considered to associate cells when tracking. We first evaluated if we could improve the tracking accuracy by considering additional cell observables, such as cell orientation, shapes, volumes and fluorescence intensities (**Figure 5.1**). The cell observables were obtained from the segmentation results of *BCM3D* (183). The nearest neighbor algorithm, which finds cells with the highest similarity, is used to run the evaluation. For both scenarios, our results showed the tracking

accuracy improves linearly with cell counting accuracy (**Figure 5.1**). When using all the aforementioned cell observables to calculate the similarity between cells, the tracking algorithm can achieve higher tracking accuracy compared to only using the cell distance (**Figure 5.1**). However, the overall improvement is not substantial. This can be ascribed to the features of the simulated data. In the simulated biofilms, all cells grow under the control of the same setups. In this case, the change of cell orientations, shapes, volumes and fluorescence intensities between adjacent time points are very similar among all cells. The similar change of these cell observables among all cells is not so helpful for the tracking algorithm to find the correct cells belonging to the same track. However, such limitation is alleviated in the experimental data. Because cells' phenotypic behavior and gene expression will be affected by the heterogeneous local environments in biofilms, the change of cell orientations, shapes, volumes and fluorescence intensities between adjacent time points could vary more among cells in different regions of the biofilm. These cell observables should then be helpful for tracking cells.

Another key finding is that the improvement of the tracking accuracy is more pronounced when the cell counting accuracy is low (**Figure 5.1**). When the cell counting accuracy is low, the cell positions might not be enough accurate for tracking cells, thus considering more cell observables can help finding the correct cells that belongs to the same track. Overall, the results here demonstrate that by including additional terms in the computation of cell similarity, we can improve the tracking accuracy.

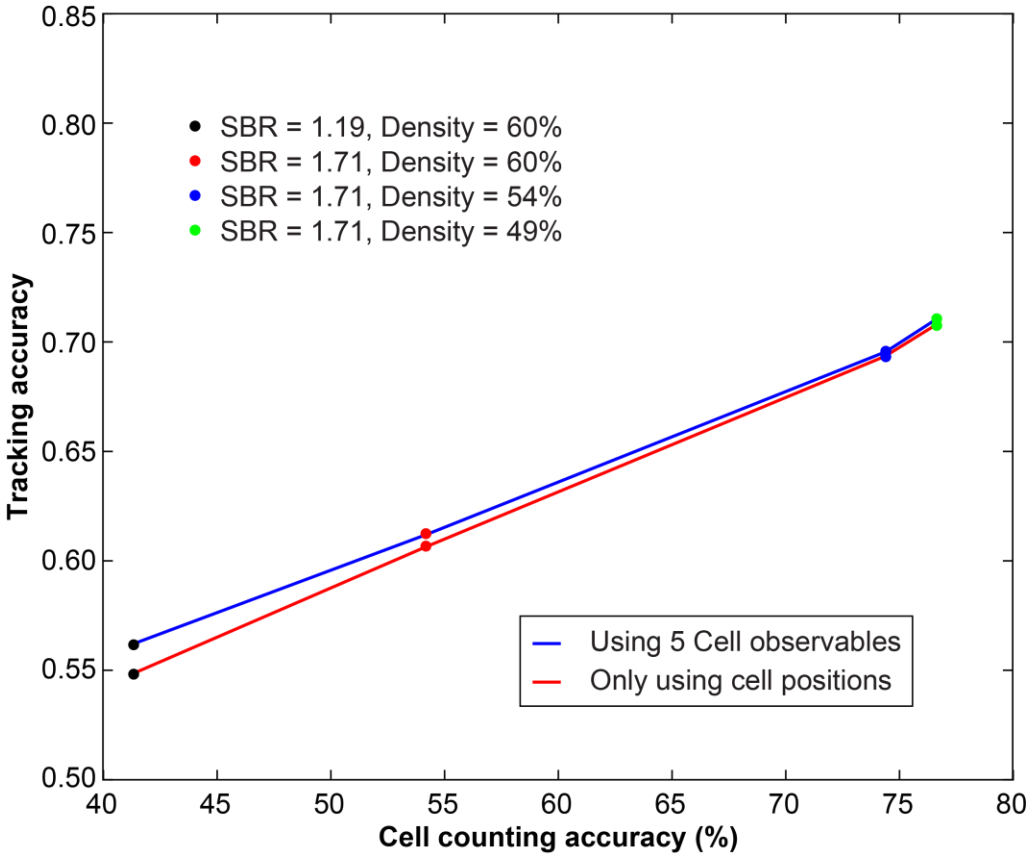


**Figure 5.1** Tracking accuracy is improved by adding 5 cell observables into the tracking algorithm. The red line represents the accuracy of the tracking algorithm by using only cell position difference (distance) to associate cells. The blue line represents the accuracy of the tracking algorithm by using 5 cell observables, including cell positions, orientations, shapes, volumes and fluorescence intensities, to associate cells. Four simulated data with different image qualities which results in different cell counting accuracies are used.

### 5.4.2 Comparison between Nearest Neighbor and Hungarian Algorithm

The basic idea for tracking cells across different time points is a one-to-one assignment problem. The nearest neighbor algorithm and the Hungarian algorithm (310) are two widely used methods to solve the assignment problem. We compared the

performance of these two algorithms with simulated data. In this experiment, the above-mentioned cell observables are all incorporated into nearest neighbor algorithm and the Hungarian algorithm when calculating the cell similarity. To set rational thresholds for each cell observable, we manually tracked 10 pairs of cells between adjacent time points datasets and then do the calculation as described in the method section (Chapter 5.3). For example, the threshold for the distance is set to 5 voxels for the simulated biofilm data. The distance threshold of 5 voxels means cells will not be linked into tracks when they are more than 5 voxels away. Setting thresholds for all cell observables significantly improves the tracking accuracy for the nearest neighbor algorithm (**Figure 5.2**). The maximum improvement of 0.11 is observed for the data with the lowest cell counting accuracy. Considering the significant improvement for the tracking accuracy, thresholds for cell observables were set with the same strategy when processing the experimental data. We observed that in this case the nearest neighbor algorithm outperforms the Hungarian algorithm for all the processed 4 simulated datasets (**Figure 5.2**). Therefore, we chose the nearest neighbor algorithm to associate cells for the experimental biofilm data.

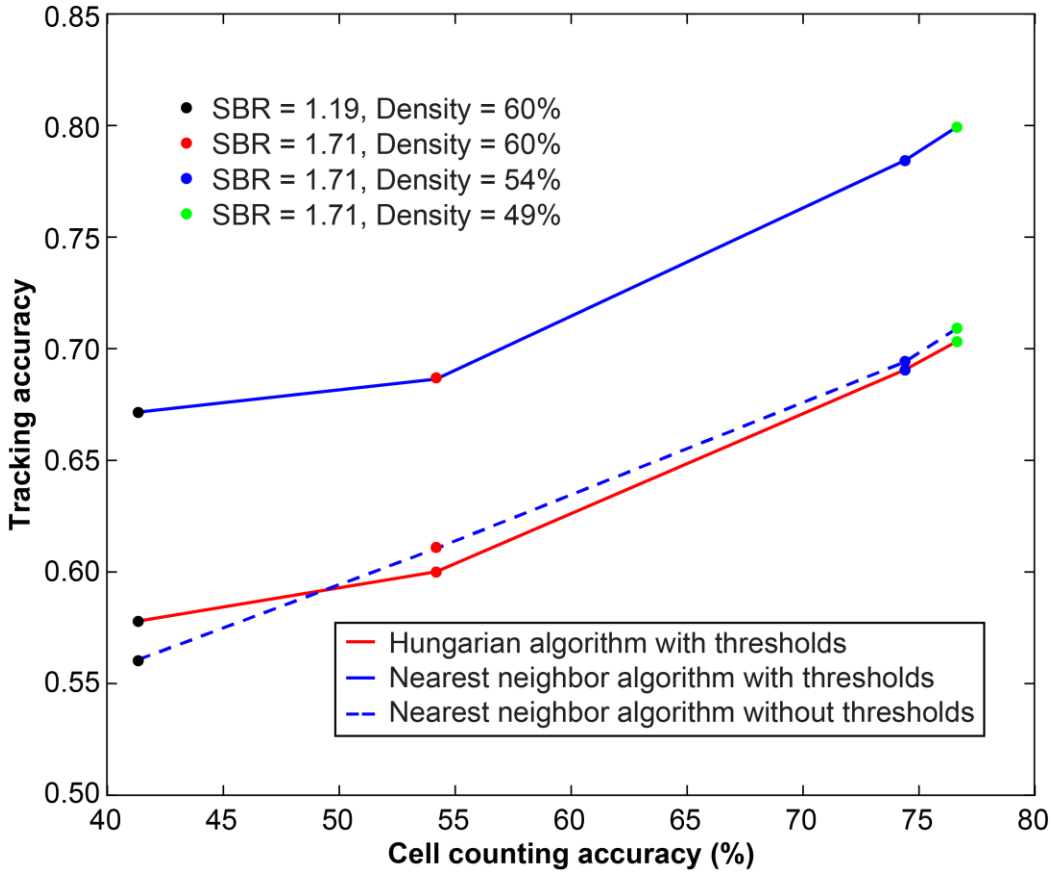


**Figure 5.2** Performance of the nearest neighbor algorithm and the Hungarian algorithm with and without setting thresholds for cell observables. The blue solid and dash lines represent tracking accuracy of the nearest neighbor algorithm with and without setting thresholds, respectively. The red solid line represents tracking accuracy of the Hungarian algorithm with setting thresholds. The result of the Hungarian algorithm without setting thresholds is about the same as with thresholds and is omitted here.

### 5.4.3 Evaluation of the Cell Counting Accuracy for the Experimental Data

We have shown that the tracking accuracy improves almost linearly with the cell counting accuracy (**Figure 5.1** and **5.2**). Therefore, higher cell counting accuracy is preferred for obtaining accurate tracking results. To evaluate the applicability of the

tracking algorithm to experimental data, we then measured the cell counting accuracy for the experimentally acquired data to see if we can obtain desired tracking accuracy (**Figure 5.3**). By choosing an IoU threshold of 0.5, which is typically chosen when reporting single cell counting accuracy values (246, 271), the cell counting accuracies for experimental *E. coli* and *S. flexneri* datasets are 62.5% and 55.2%, respectively (**Figure 5.3** vertical dash line), which falls well within the values obtained for simulated data (**Figure 5.2**), suggesting they will yield acceptable tracking accuracies.

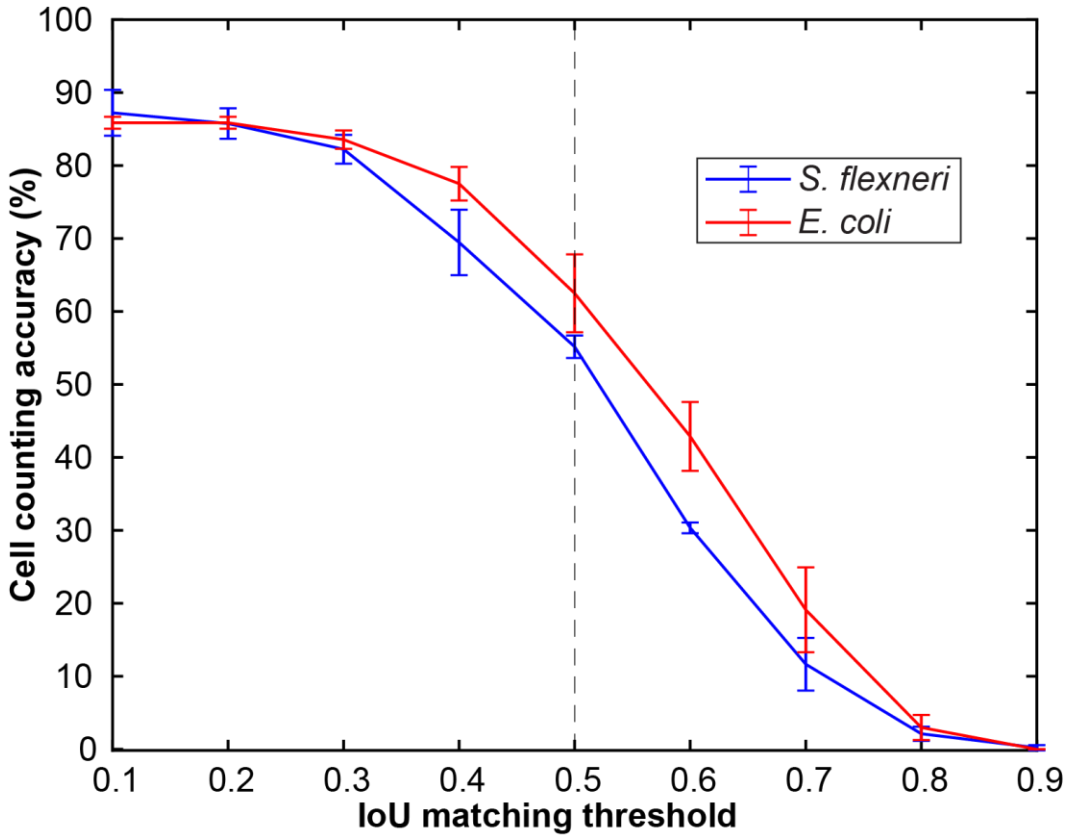


**Figure 5.3** Cell counting accuracies of experimental data. The red line represents the counting accuracy of the experimental *E. coli* datasets (cytosolic expression of GFP), while the blue one represents the *S. flexneri* datasets. Each data point is the average of the cell counting accuracies calculated using the manually traced annotation maps. The annotation

is repeated by the same researcher 3 times. Error bars represent ± one standard deviation. Curves approaching the upper right-hand corner indicate higher overall counting accuracy.

### 5.4.4 Tracking Analysis

Many studies on diffusion behaviors of bacterial cells in planktonic states, in polymeric solutions and porous media have been reported (314-325). Other studies focus on investigating the diffusion of antibiotics, oxygen and other agents in biofilms (326-331). However, little is known about the diffusion behaviors of bacterial cells in biofilms. Herein, we analyzed the diffusion of *S. flexneri* cells in the biofilm and compared the result with that of *E. coli*, the classical model for biofilm studies (**Figure 5.4**). Compared to the diffusion coefficients of planktonic cells (314, 317, 324, 332), which exhibit several $\mu m^2/s$ to tens of $\mu m^2/s$, the apparent diffusion coefficients of cells in biofilms obtained from this experiment are 2 to 4 orders of magnitude smaller. This is expected, since the gel like extracellular polymeric substances (EPS) (67, 68) in biofilms will have large constrains on cells' motilities and largely decrease their movement speed, and thus their diffusion. *S. flexneri* cells show a mean diffusion coefficient ($4.59 \times 10^{-2}$ $\mu m^2/s$) which is about 2 orders of magnitude larger than *E. coli* cells ($3.3 \times 10^{-4}$ $\mu m^2/s$). The average moving rate for *S. flexneri* and *E. coli* cells in biofilms were then calculated and compared. *S. flexneri* cells show an average moving rate (0.1630 μm/s) which is more than 1 order of magnitude larger than *E. coli* cells (0.0107 μm/s). It is worth mentioning that the average moving rate for *S. flexneri* cells obtained in this work is comparable to previously reported intracellular motility rate for individual *Shigella* cells in mouse embryonic carcinoma cells (333).

The larger apparent diffusion coefficients and faster moving rate imply that *S. flexneri* cells in the biofilm possess a more mobile feature than *E. coli*. We then calculated the cell density (~20 %) for *S. flexneri* biofilms and found it is much smaller than that (~60 %) of *E. coli* biofilms (183). The low cell density indicates that *S. flexneri* biofilms have a loose structure. This is an unexpected result, since bacterial cells in biofilms are usually densely packed. The loose structure of *S. flexneri* biofilms provide a hint to understand the increased mobility of *S. flexneri* cells compared to *E. coli*. As widely studied, *S. flexneri* utilizes actin-based motility for intra- and inter- cell spread and the bacterial factor *IcsA* is the major determinant of its actin-based motility (31, 32, 37, 332, 334, 335). However, it is unclear how *IcsA* modulates the diffusion behaviors for *S. flexneri* cells in its biofilm and needs to be further explored.

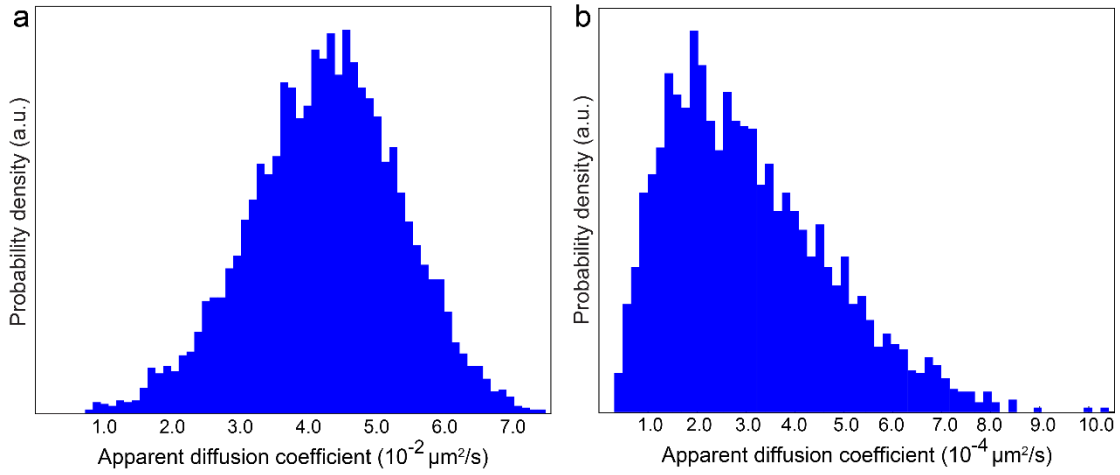


**Figure 5.4** Probability distribution of the apparent diffusion coefficients. (a) The probability distributions of the apparent diffusion coefficients for *S. flexneri* cells. 4691 trajectories which have at least 4 localizations were used to calculate the apparent diffusion coefficients. The averaged diffusion coefficients for *S. flexneri* cells is $4.59 \times 10^{-2}$ μm²/s (b) The probability distribution of the apparent diffusion coefficients for *E. coli* cells. 2768

trajectories which have at least 4 localizations were used to calculate the apparent diffusion coefficients. The averaged diffusion coefficients for *E. coli* cells is $3.3 \times 10^{-4}$ $\mu m^2/s$.

### 5.4.5 Volume Change of Single Cell

Trajectories of single cells enable researchers to inspect cells' phenotypic behaviors or developmental states along both spatial and temporal dimensions. When using fluorescent reporter strains specific to a gene or pathway of interest, the change of the fluorescence intensity of single cells can provide information about the gene expression. Single-cell resolved information of this kind will advance our understanding of the interplay between biochemical and mechanical signaling mechanisms that coordinate cellular behaviors in multicellular 3D biofilms (278, 336). As a proof of principle, we analyzed the volume change for *S. flexneri* cells in biofilms as an example to show how our tracking results provide single-cell resolved information.

The volume changes of single *S. flexneri* cells is measured by tracing cells' volumes along their trajectories. To obtain the growth rate of single cells, we analyzed trajectories of cells which have continuous growing cell volumes (**Figure 5.5**). The result shows the growth rate of these cells are in the scale of $10^{-3}$ $\mu m^3/s$. We could not find a previously reported result of the single cell growth rate for *S. flexneri*. The biological meaning of the single cell growth rate we obtained still needs further exploitation. However, we found that the slopes of the curves in **Figure 5.5** are different. That means the growth rate of different cells in the same biofilm vary. When mapping these cells into the 3D biofilm structure, we

could obtain the spatial distribution of the heterogeneous developmental states for cells in the biofilm.

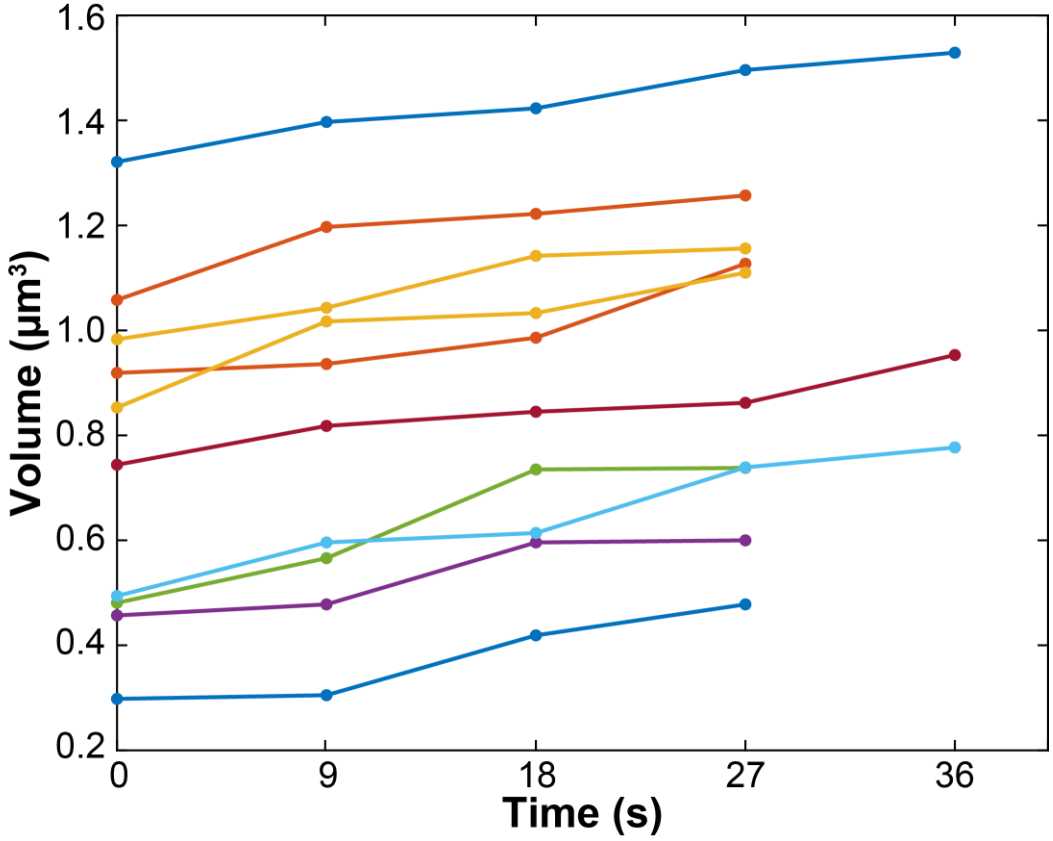


**Figure 5.5** The volume changes of single *S. flexneri* cells. Only 10 cells which have continuous growing cell volumes are shown as examples for the clarity of the figure.

## 5.5 Conclusions

The single cell behaviors within *S. flexneri* biofilms have not yet been fully explored. In this work, we first imaged live *S. flexneri* biofilms with subcellular resolution by utilizing LLSM and processed the data with one of the state of the art bacterial cell

segmentation modalities, *BCM3D* (183). We developed a multi-cell tracking approach which calculates the similarity between cells by using cell observables, including cell positions, cell orientations, shapes, volumes and fluorescence intensities. We demonstrated that considering additional cell observables can improve the tracking accuracy. The nearest neighbor algorithm is chosen to track cells based on highest similarity, since it outperforms the Hungarian algorithm. We revealed that the tracking accuracy improves almost linearly with the cell counting accuracy. We applied the tracking algorithm to the segmentation result of the experimentally acquired *S. flexneri* biofilm images and explored single cell dynamics. We observed the fast diffusion behaviors of *S. flexneri* cells in the biofilm. Being able to study the single cell behaviors in *S. flexneri* biofilm, a pathogenic strain, is a major enabling feature of the work presented here.

While our tracking algorithm can achieve high tracking accuracy in its current state, we believe that further improvements are possible by optimizing the weighting coefficients for each term in formula to calculate similarity between cells (Chapter 5, **Eq. 5.1**). It important to note that the analysis of apparent diffusion coefficients in this work might need to be refined further (313). We obtained the probability distribution of apparent diffusion coefficients, but only discussed the mean value. Representing diffusion states for all cells with the mean value of their apparent diffusion coefficients might miss sub-populations of cells with different diffusion behaviors. For example, cells adherent to the substrate or inside the biofilm could have smaller diffusion coefficients than cells on the surface of the biofilm. A potential approach for analyzing the apparent diffusion coefficients is to fit the curve of the probability distribution with a combination of different

diffusive states and to map based on the spatial distribution of the cells. The number of states can be determined by considering prior knowledge of the bacterial biofilm, such as the time for the biofilm to become mature and start dispersal cells.

# Chapter 6: Summary and Future Directions

## 6.1 Summary

Biofilms, the 3D microbial communities, have been widely investigated for their impact on many highly significant public sectors, including wastewater remediation (13), energy production (26) and global public health (57, 243, 337). Little is known about how macroscopic biofilm properties, such as its mechanical adhesion/cohesion and its biochemical metabolism, emerge from the collective actions of individual cells. A better understanding on the biochemical and mechanical mechanisms employed by single cells in biofilms could enable the design of efficient strategies for removing pathogenic biofilms (338, 339) or enable the rational design of microbial ecosystems with desirable biomedical and bioengineering capabilities (19, 43-53, 224). Obtaining these knowledge requires investigating individual cell behaviors in 3D dense biofilms.

Conventional imaging modalities, such as confocal-based microscopies are not able to resolve individual cells within thick 3D biofilms in a non-invasive manner due to the high phototoxicity (135, 278). To non-invasively image bacterial biofilms with cellular/subcellular resolution, we used lattice light-sheet microscopy (LLSM), a new imaging technology that effectively combines excellent 3D spatial resolution (200-400 nm) with fast temporal resolution (up to the scale of ms) and low phototoxicity. (137, 146-148). To enables growing and imaging biofilms at the same time, we designed a flow chamber system which is compatible with LLSM. The flow chamber system also allows growing and imaging any biofilms of interest on any desired materials. As a general sample holder, it expands the application of LLSM to perform studies when precisely *in situ* control of the environmental conditions for the sample is desired. The combination of LLSM and the

flow chamber system provide the ability to measure the spatial, phenotypic, and developmental trajectories of individual cells in 3D biofilms over multiple hours and days.

To accurately segment and classify single bacterial cells in 3D fluorescence images acquired with LLSM, we developed Bacterial Cell Morphometry 3D (*BCM3D*), an image analysis workflow that combines deep learning with mathematical image analysis. Compared to state-of-the-art bacterial cell segmentation approaches, *BCM3D* consistently achieved higher segmentation accuracy and further enables automated morphometric cell classifications in multi-population biofilms. Precise single-cell observables, including cell positions, orientations, shapes, volumes and fluorescent intensities can be obtained from the accurate segmentation results by *BCM3D*. We developed a multi-cell tracking method by utilizing these cell observables to associate cells imaged at different time points. The integrated workflow were applied to study the diffusive behavior of individual cells in *S. flexneri* biofilms.

In summary, our work enables 1) imaging of live biofilms (including pathogenic species) non-invasively at unprecedented spatial and temporal resolution using LLSM, 2) accurate segmentation and classification of single cells in 3D biofilms using *BCM3D*, 3) simultaneously tracking thousands of densely packed bacterial cells through 3D space and time. These capabilities allows study the emergent properties of microbial populations in terms of the fully-resolved behavioral phenotypes of individual cells.

## 6.2 Future Directions

Future work for the bacterial cell segmentation pipeline, *BCM3D*, include the following aspects. First, improving the simulation method to generate training data for CNNs. The current biofilm simulation model in *BCM3D* is not able to simulate species that are not straight rods, such as *Caulobacter crescentus*. To augment the application of *BCM3D*, a simulation module that can simulate biofilm formation of strains with curved cell shape should be developed. Second, it would be beneficial to integrate other types of CNNs and mathematical image processing techniques. In the current state of *BCM3D*, we combined U-Net with LCuts, but other networks and algorithms were not tested. As recently reported, *Cellpose*, a state-of-the-art, CNN-based, generalist cell segmentation algorithm can segment many cell types, without requiring parameter adjustments or further model retraining (246). The specialized algorithm designed for bacterial cell segmentation by Hartmann *et al.* using traditional mathematical image processing methods provided promising segmentation results from dense 3D *Vibrio cholerae* biofilms. Integrating these newly developed modalities into *BCM3D* might boost its performance on cell segmentation (236).

Future work for the multi-cell tracking method will focus on three aspects. First, we must develop a more precise way to calculate the shape difference between 3D objects. Currently, the aspect ratio of cells is used to calculate the shape difference. The aspect ratio only provides limited information about the 3D cell shape. Shape features, such as the curvature and the surface smoothness, are missing. Adding these terms into the calculation of the shape difference might help to improve the tracking accuracy. One possible solution

is to use elastic shape analysis (340-342). In this analysis, the dissimilarity between two 3D shapes can be measured by their geodesic distance in the shape space (340, 341). Second, optimization of the weight for the five terms, including cell positions, orientations, shapes, volumes and fluorescence intensity in the formula (Chapter 5, **Eq. 5.1**) to calculate the similarity between two cells. As said in Chapter 5, the weight for each term are empirically set. By utilizing the simulated biofilm data, we will be able to find the optimal values of the weight for each term, which can maximize the tracking accuracy. Third, precisely annotating experimental tracking data is required. Evaluation and optimization of the tracking algorithm are accomplished by using simulated biofilm data (Chapter 5), because the ground truth cell tracks are known *a priori*. However, the ground truth is unknown for the experimental biofilm data. To evaluate the performance of the tracking algorithm on experimental data, the reference for comparison must be first obtained. To obtain accurately and independently determined experimental trajectories, we can pursue three different approaches. (1) Generating the ground truth for the experimental data by human annotation. Specifically, the annotation includes two steps: manual annotation of the cells in the data set at each time point and manually association cells at different time points to generate cell tracks. Manual annotations are time consuming, but the human annotated tracking results are valuable not only for us to improve the performance of our tracking algorithm, but also for the research community when published. (2) Mixing doubly-labeled (GFP- and tdTomato-expressing) cells with singly-labeled (GFP-expressing) cells at mixing ratios of 1:100 - 1:1000. The doubly-labeled cells are visible upon red and green excitation, while the GFP-expressing cells are only visible upon green excitation. Tracking the sparse tdTomoato fluorescence signal (by fluorescence centroid

tracking, as described previously (250, 343)) will provide accurate trajectories of a subset of cells in the biofilm. (3) Expressing fluorescent protein fusions that form bright fluorescent foci at the bacterial cell poles, such as PopZ-eYFP (344, 345), YFP-PilM (346), and mNeonGreen-μNS (146), in addition to intracellular or membrane labeling. This will allow tracking individual cells by 3D single-particle tracking, which can be accomplished with many publically available modalities (257, 347-350).

Future work on the *S. flexneri* biofilms will focus on studying their development on physiologically relevant environments (e.g. human-derived intestinal organoid monolayers (351-353)). By taking the advantage of our flow chamber system, we can investigate biofilm formation on any desired substrates under controllable environmental conditions. Initial efforts will include growing intestinal organoids in the flow channel and subsequent inoculation of the infectious species, *S. flexneri* cell culture. Then, we can observe the *S. flexneri* biofilm growth on the layer of intestinal organoids with single cell resolution by imaging with LLSM. Obtaining physiologically relevant, contextual measurements of dynamic bacterial cell behaviors (e.g. surface adhesion and cell cohesion, biofilm formation, cell dispersal, and host cell and tissue invasion) is critical to understand how commensal and pathogenic bacteria colonize the human gastrointestinal system.

The current analysis of the diffusion behaviors for *S. flexneri* cells in biofilms are based on Stokes-Einstein relation (313), under the assumption of a Brownian motion model. However, bacterial cells might not undergo pure Brownian motion, especially in biofilms. Additional terms, such as the confinement from the EPS and the effect of machineries that drive bacterial cells' motion, should be incorporated into the model. As *S. flexneri* utilizes

actin-based motility for intra- and inter- cell spread, which relies on the bacterial factor *IcsA* (31, 32, 37, 332, 334, 335), exploring the effect of *IcsA* on the diffusive behaviors of *S. flexneri* cells in the biofilm would be desirable.

# References

1. Hall-Stoodley, L., J. W. Costerton, and P. Stoodley. 2004. Bacterial biofilms: From the natural environment to infectious diseases. Nat Rev Microbiol 2(2):95-108.
2. Nadell, C. D., K. Drescher, and K. R. Foster. 2016. Spatial structure, cooperation and competition in biofilms. Nat Rev Microbiol 14(9):589-600.
3. O'Toole, G., H. B. Kaplan, and R. Kolter. 2000. Biofilm formation as microbial development. Annual Review of Microbiology 54:49-79.
4. Flemming, H. C., and S. Wuertz. 2019. Bacteria and archaea on Earth and their abundance in biofilms. Nat Rev Microbiol 17(4):247-260.
5. Consortiu., H. M. P. 2012. Structure, function and diversity of the healthy human microbiome. Nature 486(7402):207-214.
6. Lovley, D. R. 2017. Happy together: microbial communities that hook up to swap electrons. Isme J 11(2):327-336.
7. Marritt, S. J., T. G. Lowe, J. Bye, D. G. G. McMillan, L. Shi, J. Fredrickson, J. Zachara, D. J. Richardson, M. R. Cheesman, L. J. C. Jeuken, and J. N. Butt. 2012. A functional description of CymA, an electron-transfer hub supporting anaerobic respiratory flexibility in Shewanella. Biochem J 444:465-474.
8. Min, D., L. Cheng, F. Zhang, X. N. Huang, D. B. Li, D. F. Liu, T. C. Lau, Y. Mu, and H. Q. Yu. 2017. Enhancing Extracellular Electron Transfer of Shewanella oneidensis MR-1 through Coupling Improved Flavin Synthesis and Metal-Reducing Conduit for Pollutant Degradation. Environ Sci Technol 51(9):5082-5089.
9. Pirbadian, S., S. E. Barchinger, K. M. Leung, H. S. Byun, Y. Jangir, R. A. Bouhenni, S. B. Reed, M. F. Romine, D. A. Saffarini, L. Shi, Y. A. Gorby, J. H. Golbeck, and M. Y. El-Naggar. 2014. Shewanella oneidensis MR-1 nanowires are outer membrane and periplasmic extensions of the extracellular electron transport components. P Natl Acad Sci USA 111(35):12883-12888.

10. Richardson, D. J., J. K. Fredrickson, and J. M. Zachara. 2012. Electron Transport at the Microbe-Mineral Interface: a synthesis of current research challenges. Biochem Soc T 40:1163-1166.
11. Shi, L., H. L. Dong, G. Reguera, H. Beyenal, A. H. Lu, J. Liu, H. Q. Yu, and J. K. Fredrickson. 2016. Extracellular electron transfer mechanisms between microorganisms and minerals. Nat Rev Microbiol 14(10):651-662.
12. Zhao, C. E., P. P. Gai, R. B. Song, Y. Chen, J. R. Zhang, and J. J. Zhu. 2017. Nanostructured material-based biofuel cells: recent advances and future prospects. Chem Soc Rev 46(5):1545-1564.
13. Lovley, D. R. 2011. Live wires: direct extracellular electron exchange for bioenergy and the bioremediation of energy-related contamination. Energy & Environmental Science 4(12).
14. Lovley, D. R., and N. S. Malvankar. 2015. Seeing is believing: novel imaging techniques help clarify microbial nanowire structure and function. Environ Microbiol 17(7):2209-2215.
15. Reguera, G., R. B. Pollina, J. S. Nicoll, and D. R. Lovley. 2007. Possible nonconductive role of Geobacter sulfurreducens pilus nanowires in biofilm formation. J Bacteriol 189(5):2125-2127.
16. Renslow, R., J. Babauta, A. Kuprat, J. Schenk, C. Ivory, J. Fredrickson, and H. Beyenal. 2013. Modeling biofilms with dual extracellular electron transfer mechanisms. Phys Chem Chem Phys 15(44):19262-19283.
17. Richter, H., K. McCarthy, K. P. Nevin, J. P. Johnson, V. M. Rotello, and D. R. Lovley. 2008. Electricity generation by Geobacter sulfurreducens attached to gold electrodes. Langmuir 24(8):4376-4379.
18. Rollefson, J. B., C. S. Stephen, M. Tien, and D. R. Bond. 2011. Identification of an extracellular polysaccharide network essential for cytochrome anchoring and biofilm formation in Geobacter sulfurreducens. J Bacteriol 193(5):1023-1033.

19. Jagmann, N., and B. Philipp. 2014. Design of synthetic microbial communities for biotechnological production processes. J Biotechnol 184:209-218.
20. Hindatu, Y., M. S. M. Annuar, and A. M. Gumel. 2017. Mini-review: Anode modification for improved performance of microbial fuel cell. Renewable and Sustainable Energy Reviews 73:236-248.
21. Mustakeem. 2015. Electrode materials for microbial fuel cells: nanomaterial approach. Materials for Renewable and Sustainable Energy 4(4).
22. Santoro, C., C. Arbizzani, B. Erable, and I. Ieropoulos. 2017. Microbial fuel cells: From fundamentals to applications. A review. J Power Sources 356:225-244.
23. Sonawane, J. M., A. Yadav, P. C. Ghosh, and S. B. Adeloju. 2017. Recent advances in the development and utilization of modern anode materials for high performance microbial fuel cells. Biosens Bioelectron 90:558-576.
24. Zhang, P., J. Liu, Y. P. Qu, J. Zhang, Y. J. Zhong, and Y. J. Feng. 2017. Enhanced performance of microbial fuel cell with a bacteria/multi-walled carbon nanotube hybrid biofilm. J Power Sources 361:318-325.
25. Zhou, M., M. Chi, J. Luo, H. He, and T. Jin. 2011. An overview of electrode materials in microbial fuel cells. J Power Sources 196(10):4427-4435.
26. Logan, B. E. 2009. Exoelectrogenic bacteria that power microbial fuel cells. Nat Rev Microbiol 7(5):375-381.
27. Hentzer, M., G. M. Teitzel, G. J. Balzer, A. Heydorn, S. Molin, M. Givskov, and M. R. Parsek. 2001. Alginate overproduction affects Pseudomonas aeruginosa biofilm structure and function. J Bacteriol 183(18):5395-5401.
28. Wei, Q., and L. Y. Z. Ma. 2013. Biofilm Matrix and Its Regulation in Pseudomonas aeruginosa. Int J Mol Sci 14(10):20983-21005.
29. Wozniak, D. J., T. J. O. Wyckoff, M. Starkey, R. Keyser, P. Azadi, G. A. O'Toole, and M. R. Parsek. 2003. Alginate is not a significant component of the extracellular polysaccharide matrix of PA14 and PAO1 Pseudomonas aeruginosa biofilms. P Natl Acad Sci USA 100(13):7907-7912.

30. Cole, S. J., A. R. Records, M. W. Orr, S. B. Linden, and V. T. Lee. 2014. Catheter-Associated Urinary Tract Infection by Pseudomonas aeruginosa Is Mediated by Exopolysaccharide-Independent Biofilms. Infect Immun 82(5):2048-2058.

31. Brotcke Zumsteg, A., C. Goosmann, V. Brinkmann, R. Morona, and A. Zychlinsky. 2014. IcsA is a Shigella flexneri adhesin regulated by the type III secretion system and required for pathogenesis. Cell Host Microbe 15(4):435-445.

32. Doyle, M. T., M. Grabowicz, and R. Morona. 2015. A small conserved motif supports polarity augmentation of Shigella flexneri IcsA. Microbiology 161(11):2087-2097.

33. Ellafi, A., F. B. Abdallah, R. Lagha, B. Harbi, and A. Bakhrouf. 2011. Biofilm production, adherence and morphological alterations of Shigella spp. under salt conditions. Annals of Microbiology 61(4):741-747.

34. Goldberg, M. B., and J. A. Theriot. 1995. Shigella-Flexneri Surface Protein Icsa Is Sufficient to Direct Actin-Based Motility. P Natl Acad Sci USA 92(14):6572-6576.

35. Kaoukab-Raji, A., L. Biskri, and A. Allaoui. 2020. Inactivation of the sfgtr4 Gene of Shigella flexneri Induces Biofilm Formation and Affects Bacterial Pathogenicity. Microorganisms 8(6).

36. Koseoglu, V. K., C. P. Hall, E. M. Rodriguez-Lopez, and H. Agaisse. 2019. The Autotransporter IcsA Promotes Shigella flexneri Biofilm Formation in the Presence of Bile Salts. Infect Immun 87(7).

37. Leupold, S., P. Busing, P. J. Mas, D. J. Hart, and A. Scrima. 2017. Structural insights into the architecture of the Shigella flexneri virulence factor IcsA/VirG and motifs involved in polar distribution and secretion. J Struct Biol 198(1):19-27.

38. Nickerson, K. P., R. B. Chanin, J. R. Sistrunk, D. A. Rasko, P. J. Fink, E. M. Barry, J. P. Nataro, and C. S. Faherty. 2017. Analysis of Shigella flexneri

Resistance, Biofilm Formation, and Transcriptional Profile in Response to Bile Salts. Infect Immun 85(6).

39. Bryers, J. D. 2008. Medical biofilms. Biotechnol Bioeng 100(1):1-18.
40. Miquel, S., R. Lagrafeuille, B. Souweine, and C. Forestier. 2016. Anti-biofilm Activity as a Health Issue. Front Microbiol 7(592).
41. Costerton, J. W., P. S. Stewart, and E. P. Greenberg. 1999. Bacterial Biofilms A Common Cause of Persistent Infections. Science 284(5418):1318-1322.
42. Klevens, R. M., J. R. Edwards, C. L. Richards, Jr., T. C. Horan, R. P. Gaynes, D. A. Pollock, and D. M. Cardo. 2007. Estimating health care-associated infections and deaths in U.S. hospitals, 2002. Public Health Rep 122(2):160-166.
43. Fredrickson, J. K. 2015. Ecological communities by design. Science 348(6242):1425-1427.
44. Grosskopf, T., and O. S. Soyer. 2014. Synthetic microbial communities. Curr Opin Microbiol 18:72-77.
45. Kouzuma, A., S. Kato, and K. Watanabe. 2015. Microbial interspecies interactions: recent findings in syntrophic consortia. Front Microbiol 6:477.
46. Liu, J., A. Prindle, J. Humphries, M. Gabalda-Sagarra, M. Asally, D. Y. Lee, S. Ly, J. Garcia-Ojalvo, and G. M. Suel. 2015. Metabolic co-dependence gives rise to collective oscillations within biofilms. Nature 523(7562):550-554.
47. Prindle, A., J. Liu, M. Asally, S. Ly, J. Garcia-Ojalvo, and G. M. Suel. 2015. Ion channels enable electrical communication in bacterial communities. Nature 527(7576):59-63.
48. Humphries, J., L. Xiong, J. Liu, A. Prindle, F. Yuan, H. A. Arjes, L. Tsimring, and G. M. Suel. 2017. Species-Independent Attraction to Biofilms through Electrical Signaling. Cell 168(1-2):200-209 e212.
49. Liu, J., R. Martinez-Corral, A. Prindle, D.-y. D. Lee, J. Larkin, M. Gabalda-Sagarra, J. Garcia-Ojalvo, and G. M. Süel. 2017. Coupling between distant biofilms and emergence of nutrient time-sharing. Science 356(6338):638-642.

50. Mitri, S., and K. R. Foster. 2013. The genotypic view of social interactions in microbial communities. Annu Rev Genet 47:247-273.
51. Drescher, K., C. D. Nadell, H. A. Stone, N. S. Wingreen, and B. L. Bassler. 2014. Solutions to the public goods dilemma in bacterial biofilms. Curr Biol 24(1):50-55.
52. Persat, A., C. D. Nadell, M. K. Kim, F. Ingremeau, A. Siryaporn, K. Drescher, N. S. Wingreen, B. L. Bassler, Z. Gitai, and H. A. Stone. 2015. The mechanical world of bacteria. Cell 161(5):988-997.
53. Papenfort, K., and B. L. Bassler. 2016. Quorum sensing signal-response systems in Gram-negative bacteria. Nat Rev Microbiol 14(9):576-588.
54. Garrett, T. R., M. Bhakoo, and Z. B. Zhang. 2008. Bacterial adhesion and biofilms on surfaces. Prog Nat Sci-Mater 18(9):1049-1056.
55. Hermansson, M. 1999. The DLVO theory in microbial adhesion. Colloid Surface B 14(1-4):105-119.
56. Kostakioti, M., M. Hadjifrangiskou, and S. J. Hultgren. 2013. Bacterial Biofilms: Development, Dispersal, and Therapeutic Strategies in the Dawn of the Postantibiotic Era. Csh Perspect Med 3(4).
57. Donlan, R. M. 2002. Biofilms: Microbial life on surfaces. Emerg Infect Dis 8(9):881-890.
58. Beitelshees, M., A. Hill, C. H. Jones, and B. A. Pfeifer. 2018. Phenotypic Variation during Biofilm Formation: Implications for Anti-Biofilm Therapeutic Design. Materials (Basel) 11(7).
59. O'Toole, G. A., and R. Kolter. 1998. Flagellar and twitching motility are necessary for Pseudomonas aeruginosa biofilm development. Mol Microbiol 30(2):295-304.
60. Pratt, L. A., and R. Kolter. 1998. Genetic analysis of Escherichia coli biofilm formation: roles of flagella, motility, chemotaxis and type I pili. Mol Microbiol 30(2):285-293.
61. Watnick, P. I., and R. Kolter. 1999. Steps in the development of a Vibrio cholerae El Tor biofilm. Mol Microbiol 34(3):586-595.

62. Klausen, M., A. Aaes-Jorgensen, S. Molin, and T. Tolker-Nielsen. 2003. Involvement of bacterial migration in the development of complex multicellular structures in Pseudomonas aeruginosa biofilms. Mol Microbiol 50(1):61-68.

63. Toutain, C. M., N. C. Caizza, M. E. Zegans, and G. A. O'Toole. 2007. Roles for flagellar stators in biofilm formation by Pseudomonas aeruginosa. Research in Microbiology 158(5):471-477.

64. Abbot, E. L., W. D. Smith, G. P. S. Siou, C. Chiriboga, R. J. Smith, J. A. Wilson, B. H. Hirst, and M. A. Kehoe. 2007. Pili mediate specific adhesion of Streptococcus pyogenes to human tonsil and skin. Cell Microbiol 9(7):1822-1833.

65. Maisey, H. C., M. Hensler, V. Nizet, and K. S. Doran. 2007. Group B streptococcal pilus proteins contribute to adherence to and invasion of brain microvascular endothelial cells. J Bacteriol 189(4):1464-1467.

66. Manetti, A. G. O., C. Zingaretti, F. Falugi, S. Capo, M. Bombaci, F. Bagnoli, G. Gambellini, G. Bensi, M. Mora, A. M. Edwards, J. M. Musser, E. A. Graviss, J. L. Telford, G. Grandi, and I. Margarit. 2007. Streptococcus pyogenes pili promote pharyngeal cell adhesion and biofilm formation. Mol Microbiol 64(4):968-983.

67. Flemming, H. C., T. R. Neu, and D. J. Wozniak. 2007. The EPS matrix: The "House of Biofilm cells". J Bacteriol 189(22):7945-7947.

68. Flemming, H. C., and J. Wingender. 2010. The biofilm matrix. Nat Rev Microbiol 8(9):623-633.

69. Hong, S. H., J. Lee, and T. K. Wood. 2010. Engineering global regulator Hha of Escherichia coli to control biofilm dispersal. Microb Biotechnol 3(6):717-728.

70. Karatan, E., and P. Watnick. 2009. Signals, Regulatory Networks, and Materials That Build and Break Bacterial Biofilms. Microbiol Mol Biol R 73(2):310-+.

71. Rowe, M. C., H. L. Withers, and S. Swift. 2010. Uropathogenic Escherichia coli forms biofilm aggregates under iron restriction that disperse upon the supply of iron. Fems Microbiol Lett 307(1):102-109.

72. Sauer, K., M. C. Cullen, A. H. Rickard, L. A. H. Zeef, D. G. Davies, and P. Gilbert. 2004. Characterization of nutrient-induced dispersion in Pseudomonas aeruginosa PAO1 biofilm. J Bacteriol 186(21):7312-7326.

73. Stewart, P. S., and M. J. Franklin. 2008. Physiological heterogeneity in biofilms. Nat Rev Microbiol 6(3):199-210.

74. Franklin, M. J., C. Chang, T. Akiyama, and B. Bothner. 2015. New Technologies for Studying Biofilms. Microbiol Spectr 3(4).

75. Becraft, E. D., F. M. Cohan, M. Kuhl, S. I. Jensen, and D. M. Ward. 2011. Fine-Scale Distribution Patterns of Synechococcus Ecological Diversity in Microbial Mats of Mushroom Spring, Yellowstone National Park. Appl Environ Microb 77(21):7689-7697.

76. Kim, W., F. Racimo, J. Schluter, S. B. Levy, and K. R. Foster. 2014. Importance of positioning for microbial evolution. P Natl Acad Sci USA 111(16):E1639-E1647.

77. Ramsing, N. B., M. J. Ferris, and D. M. Ward. 2000. Highly ordered vertical structure of Synechococcus populations within the one-millimeter-thick photic zone of a hot spring cyanobacterial mat. Appl Environ Microb 66(3):1038-1049.

78. Rani, S. A., B. Pitts, H. Beyenal, R. A. Veluchamy, Z. Lewandowski, W. M. Davison, K. Buckingham-Meyer, and P. S. Stewart. 2007. Spatial patterns of DNA replication, protein synthesis, and oxygen concentration within bacterial biofilms reveal diverse physiological states. J Bacteriol 189(11):4223-4233.

79. Rasmussen, K., and Z. Lewandowski. 1998. Microelectrode measurements of local mass transport rates in heterogeneous biofilms. Biotechnol Bioeng 59(3):302-309.

80. Werner, E., F. Roe, A. Bugnicourt, M. J. Franklin, A. Heydorn, S. Molin, B. Pitts, and P. S. Stewart. 2004. Stratified growth in Pseudomonas aeruginosa biofilms. Appl Environ Microb 70(10):6188-6196.

81. Boles, B. R., M. Thoendel, and P. K. Singh. 2004. Self-generated diversity produces "insurance effects" in biofilm communities. P Natl Acad Sci USA 101(47):16630-16635.

82. Hansen, S. K., P. B. Rainey, J. A. J. Haagensen, and S. Molin. 2007. Evolution of species interactions in a biofilm community. Nature 445(7127):533-536.

83. Kirisits, M. J., L. Prost, M. Starkey, and M. R. Parsek. 2005. Characterization of colony morphology variants isolated from Pseudomonas aeruginosa biofilms. Appl Environ Microb 71(8):4809-4821.

84. Nguyen, D., and P. K. Singh. 2006. Evolving stealth: Genetic adaptation of Pseudomonas aeruginosa during cystic fibrosis infections. P Natl Acad Sci USA 103(22):8305-8306.

85. Yildiz, F. H., and G. K. Schoolnik. 1999. Vibrio cholerae O1 El Tor: Identification of a gene cluster required for the rugose colony type, exopolysaccharide production, chlorine resistance, and biofilm formation. P Natl Acad Sci USA 96(7):4028-4033.

86. Baty, A. M., C. C. Eastburn, Z. Diwu, S. Techkarnjanaruk, A. E. Goodman, and G. G. Geesey. 2000. Differentiation of chitinase-active and non-chitinase-active subpopulations of a marine bacterium during chitin degradation. Appl Environ Microb 66(8):3566-3573.

87. Baty, A. M., C. C. Eastburn, S. Techkarnjanaruk, A. E. Goodman, and G. G. Geesey. 2000. Spatial and temporal variations in chitinolytic gene expression and bacterial biomass production during chitin degradation. Appl Environ Microb 66(8):3574-3585.

88. Chai, Y. R., F. Chu, R. Kolter, and R. Losick. 2008. Bistability and biofilm formation in Bacillus subtilis. Mol Microbiol 67(2):254-263.

89. Elowitz, M. B., A. J. Levine, E. D. Siggia, and P. S. Swain. 2002. Stochastic gene expression in a single cell. Science 297(5584):1183-1186.
90. McAdams, H. H., and A. Arkin. 1997. Stochastic mechanisms in gene expression. P Natl Acad Sci USA 94(3):814-819.
91. Hasty, J., J. Pradines, M. Dolnik, and J. J. Collins. 2000. Noise-based switches and amplifiers for gene expression. P Natl Acad Sci USA 97(5):2075-2080.
92. Vlamakis, H., C. Aguilar, R. Losick, and R. Kolter. 2008. Control of cell fate by the formation of an architecturally complex bacterial community. Gene Dev 22(7):945-953.
93. Branda, S. S., F. Chu, D. B. Kearns, R. Losick, and R. Kolter. 2006. A major protein component of the Bacillus subtilis biofilm matrix. Mol Microbiol 59(4):1229-1238.
94. Liu, J. T., R. Martinez-Corral, A. Prindle, D. Y. D. Lee, J. Larkin, M. Gabalda-Sagarra, J. Garcia-Ojalvo, and G. M. Suel. 2017. Coupling between distant biofilms and emergence of nutrient time-sharing. Science 356(6338):638-641.
95. Gelens, L., L. Hill, A. Vandervelde, J. Danckaert, and R. Loris. 2013. A General Model for Toxin-Antitoxin Module Dynamics Can Explain Persister Cell Formation in E. coli. Plos Comput Biol 9(8).
96. Koh, R. S., and M. J. Dunlop. 2012. Modeling suggests that gene circuit architecture controls phenotypic variability in a bacterial persistence network. Bmc Syst Biol 6.
97. Lewis, K. 2007. Persister cells, dormancy and infectious disease. Nat Rev Microbiol 5(1):48-56.
98. Mulcahy, L. R., J. L. Burns, S. Lory, and K. Lewis. 2010. Emergence of Pseudomonas aeruginosa Strains Producing High Levels of Persister Cells in Patients with Cystic Fibrosis. J Bacteriol 192(23):6191-6199.
99. Zhang, Q. C., G. Lambert, D. Liao, H. Kim, K. Robin, C. K. Tung, N. Pourmand, and R. H. Austin. 2011. Acceleration of Emergence of Bacterial

Antibiotic Resistance in Connected Microenvironments. Science 333(6050):1764-1767.

100. Rossi, N. A., I. El Meouche, and M. J. Dunlop. 2019. Forecasting cell fate during antibiotic exposure using stochastic gene expression. Commun Biol 2:259.

101. Pinto, R. M., F. A. Soares, S. Reis, C. Nunes, and P. Van Dijck. 2020. Innovative Strategies Toward the Disassembly of the EPS Matrix in Bacterial Biofilms. Front Microbiol 11:952.

102. Srivastava, S., and A. Bhargava. 2016. Biofilms and human health. Biotechnol Lett 38(1):1-22.

103. Donlan, R. M., and J. W. Costerton. 2002. Biofilms: Survival mechanisms of clinically relevant microorganisms. Clin Microbiol Rev 15(2):167-+.

104. Flemming, H. C., J. Wingender, U. Szewzyk, P. Steinberg, S. A. Rice, and S. Kjelleberg. 2016. Biofilms: an emergent form of bacterial life. Nat Rev Microbiol 14(9):563-575.

105. Dobretsov, S., R. M. M. Abed, K. Sharp, O. Skalli, L. G. Boykins, and L. Coons. 2014. Microscopy of biofilms. Biofouling Methods:1-43.

106. Azeredo, J., N. F. Azevedo, R. Briandet, N. Cerca, T. Coenye, A. R. Costa, M. Desvaux, G. Di Bonaventura, M. Hebraud, Z. Jaglic, M. Kacaniova, S. Knochel, A. Lourenco, F. Mergulhao, R. L. Meyer, G. Nychas, M. Simoes, O. Tresse, and C. Sternberg. 2017. Critical review on biofilm methods. Crit Rev Microbiol 43(3):313-351.

107. Lawrence, J. R., D. R. Korber, B. D. Hoyle, J. W. Costerton, and D. E. Caldwell. 1991. Optical Sectioning of Microbial Biofilms. J Bacteriol 173(20):6558-6567.

108. Parthasarathy, R. 2018. Monitoring microbial communities using light sheet fluorescence microscopy. Curr Opin Microbiol 43:31-37.

109. Sankaran, J., A. Karampatzakis, S. A. Rice, and T. Wohland. 2018. Quantitative imaging and spectroscopic technologies for microbiology. Fems Microbiol Lett 365(9).

110. Taute, K. M., S. Gude, S. J. Tans, and T. S. Shimizu. 2015. High-throughput 3D tracking of bacteria on a standard phase contrast microscope. Nat Commun 6:8776.

111. Tolker-Nielsen, T., and C. Sternberg. 2014. Methods for Studying Biofilm Formation: Flow Cells and Confocal Laser Scanning Microscopy. Pseudomonas: Methods and Protocols 1149:615-629.

112. Shapiro, H. H. 2000. Microbial analysis at the single-cell level: tasks and techniques. J Microbiol Meth 42(1):3-16.

113. Arnold, J. W., and G. W. Bailey. 2000. Surface finishes on stainless steel reduce bacterial attachment and early biofilm formation: Scanning electron and atomic force microscopy study. Poultry Sci 79(12):1839-1845.

114. Asahi, Y., J. Miura, T. Tsuda, S. Kuwabata, K. Tsunashima, Y. Noiri, T. Sakata, S. Ebisu, and M. Hayashi. 2015. Simple observation of Streptococcus mutans biofilm by scanning electron microscopy using ionic liquids. Amb Express 5.

115. Asally, M., M. Kittisopikul, P. Rue, Y. J. Du, Z. X. Hu, T. Cagatay, A. B. Robinson, H. B. Lu, J. Garcia-Ojalvo, and G. M. Suel. 2012. Localized cell death focuses mechanical forces during 3D patterning in a biofilm. P Natl Acad Sci USA 109(46):18891-18896.

116. Bakke, R., R. Kommedal, and S. Kalvenes. 2001. Quantification of biofilm accumulation by an optical approach. J Microbiol Meth 44(1):13-26.

117. Baum, M. M., A. Kainovic, T. O'Keeffe, R. Pandita, K. McDonald, S. Wu, and P. Webster. 2009. Characterization of structures in biofilms formed by a Pseudomonas fluorescens isolated from soil. Bmc Microbiol 9.

118. Bridier, A., F. Dubois-Brissonnet, A. Boubetra, V. Thomas, and R. Briandet. 2010. The biofilm architecture of sixty opportunistic pathogens deciphered using a high throughput CLSM method. J Microbiol Meth 82(1):64-70.

119. Bulut, F., F. Meric, E. Yorgancilar, Y. Nergiz, M. Akkus, S. Nergiz, and Y. Nasir. 2014. Effects of N-acetyl-cysteine and acetylsalicylic acid on the tonsil

bacterial biofilm tissues by light and electron microscopy. Eur Rev Med Pharmaco 18(23):3720-3725.

120. Chao, Y. Q., and T. Zhang. 2011. Optimization of fixation methods for observation of bacterial cell morphology and surface ultrastructures by atomic force microscopy. Appl Microbiol Biot 92(2):381-392.

121. de Carvalho, C. C. C. R., and M. M. R. da Fonseca. 2007. Assessment of three-dimensional biofilm structure using an optical microscope. Biotechniques 42(5):616-620.

122. Guilbaud, M., P. Piveteau, M. Desvaux, S. Brisse, and R. Briandet. 2015. Exploring the Diversity of Listeria monocytogenes Biofilm Architecture by High-Throughput Confocal Laser Scanning Microscopy and the Predominance of the Honeycomb-Like Morphotype. Appl Environ Microb 81(5):1804-1810.

123. Holling, N., C. Dedi, C. E. Jones, J. A. Hawthorne, G. W. Hanlon, J. P. Salvage, B. A. Patel, L. M. Barnes, and B. V. Jones. 2014. Evaluation of environmental scanning electron microscopy for analysis of Proteus mirabilis crystalline biofilms in situ on urinary catheters. Fems Microbiol Lett 355(1):20-27.

124. Hung, C., Y. Z. Zhou, J. S. Pinkner, K. W. Dodson, J. R. Crowley, J. Heuser, M. R. Chapman, M. Hadjifrangiskou, J. P. Henderson, and S. J. Hultgren. 2013. Escherichia coli Biofilms Have an Organized and Complex Extracellular Matrix Structure. Mbio 4(5).

125. Hunter, R. C., and T. J. Beveridge. 2005. High-resolution visualization of Pseudomonas aeruginosa PAO1 biofilms by freeze-substitution transmission electron microscopy. J Bacteriol 187(22):7619-7630.

126. Kner, P., B. B. Chhun, E. R. Griffis, L. Winoto, and M. G. Gustafsson. 2009. Super-resolution video microscopy of live cells by structured illumination. Nat Methods 6(5):339-342.

127. Neu, T. R., and J. R. Lawrence. 2014. Investigation of Microbial Biofilm Structure by Laser Scanning Microscopy. Adv Biochem Eng Biot 146:1-51.

128. Neu, T. R., and J. R. Lawrence. 2014. Advanced Techniques for In Situ Analysis of the Biofilm Matrix (Structure, Composition, Dynamics) by Means of Laser Scanning Microscopy. Methods Mol Biol 1147:43-64.

129. Sun, L. M., K. Liao, and D. Y. Wang. 2015. Effects of Magnolol and Honokiol on Adhesion, Yeast-Hyphal Transition, and Formation of Biofilm by Candida albicans. Plos One 10(2).

130. Yamakawa, T., K. Tomita, and J. Sawai. 2018. Characteristics of Biofilms Formed by Co-Culture of Listeria monocytogenes with Pseudomonas aeruginosa at Low Temperatures and Their Sensitivity to Antibacterial Substances. Biocontrol Sci 23(3):107-119.

131. Yan, J., A. G. Sharo, H. A. Stone, N. S. Wingreen, and B. L. Bassler. 2016. Vibrio cholerae biofilm growth program and architecture revealed by single-cell live imaging. P Natl Acad Sci USA 113(36):E5337-E5343.

132. Gregor, I., and J. Enderlein. 2019. Image scanning microscopy. Curr Opin Chem Biol 51:74-83.

133. Drescher, K., J. Dunkel, C. D. Nadell, S. van Teeffelen, I. Grnja, N. S. Wingreen, H. A. Stone, and B. L. Bassler. 2016. Architectural transitions in Vibrio cholerae biofilms at single-cell resolution. P Natl Acad Sci USA 113(14):E2066-E2072.

134. Hartmann, R., P. K. Singh, P. Pearce, R. Mok, B. Song, F. Diaz-Pascual, J. Dunkel, and K. Drescher. 2019. Emergence of three-dimensional order and structure in growing biofilms. Nat Phys 15(3):251-+.

135. Waldchen, S., J. Lehmann, T. Klein, S. van de Linde, and M. Sauer. 2015. Light-induced cell damage in live-cell super-resolution microscopy. Sci Rep-Uk 5.

136. Qin, B., C. Fei, A. A. Bridges, A. A. Mashruwala, H. A. Stone, N. S. Wingreen, and B. L. Bassler. 2020. Cell position fates and collective fountain flow in bacterial biofilms revealed by light-sheet microscopy. Science 369(6499):71.

137. Chen, B. C., W. R. Legant, K. Wang, L. Shao, D. E. Milkie, M. W. Davidson, C. Janetopoulos, X. S. Wu, J. A. Hammer, 3rd, Z. Liu, B. P. English, Y. Mimori-Kiyosue, D. P. Romero, A. T. Ritter, J. Lippincott-Schwartz, L. Fritz-Laylin, R. D. Mullins, D. M. Mitchell, J. N. Bembenek, A. C. Reymann, R. Bohme, S. W. Grill, J. T. Wang, G. Seydoux, U. S. Tulu, D. P. Kiehart, and E. Betzig. 2014. Lattice light-sheet microscopy: imaging molecules to embryos at high spatiotemporal resolution. Science 346(6208):1257998.

138. Li, D., L. Shao, B. C. Chen, X. Zhang, M. Zhang, B. Moses, D. E. Milkie, J. R. Beach, J. A. Hammer, 3rd, M. Pasham, T. Kirchhausen, M. A. Baird, M. W. Davidson, P. Xu, and E. Betzig. 2015. Extended-resolution structured illumination imaging of endocytic and cytoskeletal dynamics. Science 349(6251):aab3500.

139. Chang, B. J., M. Kittisopikul, K. M. Dean, P. Roudot, E. S. Welf, and R. Fiolka. 2019. Universal light-sheet generation with field synthesis. Nat Methods 16(3):235-238.

140. Dean, K. M., P. Roudot, E. S. Welf, G. Danuser, and R. Fiolka. 2015. Deconvolution-free Subcellular Imaging with Axially Swept Light Sheet Microscopy. Biophys J 108(12):2807-2815.

141. Chakraborty, T., M. K. Driscoll, E. Jeffery, M. M. Murphy, P. Roudot, B. J. Chang, S. Vora, W. M. Wong, C. D. Nielson, H. Zhang, V. Zhemkov, C. Hiremath, E. D. De La Cruz, Y. Yi, I. Bezprozvanny, H. Zhao, R. Tomer, R. Heintzmann, J. P. Meeks, D. K. Marciano, S. J. Morrison, G. Danuser, K. M. Dean, and R. Fiolka. 2019. Light-sheet microscopy of cleared tissues with isotropic, subcellular resolution. Nat Methods 16(11):1109-1113.

142. Dunsby, C. 2008. Optically sectioned imaging by oblique plane microscopy. Opt. Express 16(25):20306-20316.

143. Voleti, V., K. B. Patel, W. Li, C. P. Campos, S. Bharadwaj, H. Yu, C. Ford, M. J. Casper, R. W. Yan, and W. Liang. 2019. Real-time volumetric microscopy of in vivo dynamics and large-scale samples with SCAPE 2.0. Nature methods 16(10):1054-1062.

144. Bouchard, M. B., V. Voleti, C. S. Mendes, C. Lacefield, W. B. Grueber, R. S. Mann, R. M. Bruno, and E. M. Hillman. 2015. Swept confocally-aligned planar excitation (SCAPE) microscopy for high-speed volumetric imaging of behaving organisms. Nature photonics 9(2):113.

145. York, A. 2020. High NA single-objective light-sheet. In https://andrewgyork.github.io/high_na_single_objective_lightsheet/, Github.

146. Qin, B., C. Fei, A. A. Bridges, A. A. Mashruwala, H. A. Stone, N. S. Wingreen, and B. L. Bassler. 2020. Cell position fates and collective fountain flow in bacterial biofilms revealed by light-sheet microscopy. Science:eabb8501.

147. Yang, B., X. Chen, Y. Wang, S. Feng, V. Pessino, N. Stuurman, N. H. Cho, K. W. Cheng, S. J. Lord, L. Xu, D. Xie, R. D. Mullins, M. D. Leonetti, and B. Huang. 2019. Epi-illumination SPIM for volumetric imaging with high spatial-temporal resolution. Nat Methods 16(6):501-504.

148. Voleti, V., K. B. Patel, W. Li, C. Perez Campos, S. Bharadwaj, H. Yu, C. Ford, M. J. Casper, R. W. Yan, W. Liang, C. Wen, K. D. Kimura, K. L. Targoff, and E. M. C. Hillman. 2019. Real-time volumetric microscopy of in vivo dynamics and large-scale samples with SCAPE 2.0. Nat Methods 16(10):1054-1062.

149. Kampf, J., J. Gerwig, K. Kruse, R. Cleverley, M. Dormeyer, A. Grunberger, D. Kohlheyer, F. M. Commichau, R. J. Lewis, and J. Stulke. 2018. Selective Pressure for Biofilm Formation in Bacillus subtilis: Differential Effect of Mutations in the Master Regulator SinR on Bistability. Mbio 9(5).

150. Chimileski, S., M. J. Franklin, and R. T. Papke. 2014. Biofilms formed by the archaeon Haloferax volcanii exhibit cellular differentiation and social motility, and facilitate horizontal gene transfer. Bmc Biol 12.

151. Johnson, L., S. R. Horsman, L. Charron-Mazenod, A. L. Turnbull, H. Mulcahy, M. G. Surette, and S. Lewenza. 2013. Extracellular DNA-induced antimicrobial peptide resistance in Salmonella enterica serovar Typhimurium. Bmc Microbiol 13.

152. Berney, M., F. Hammes, F. Bosshard, H. U. Weilenmann, and T. Egli. 2007. Assessment and interpretation of bacterial viability by using the LIVE/DEAD BacLight kit in combination with flow cytometry. Appl Environ Microb 73(10):3283-3290.

153. Sanchez, Z., A. Tani, and K. Kimbara. 2013. Extensive Reduction of Cell Viability and Enhanced Matrix Production in Pseudomonas aeruginosa PAO1 Flow Biofilms Treated with a D-Amino Acid Mixture. Appl Environ Microb 79(4):1396-1399.

154. Tsai, Y. J., Y. C. Lin, W. B. Wu, P. H. Chiu, B. J. Lin, and S. P. Hao. 2013. Biofilm Formations in Nasopharyngeal Tissues of Patients with Nasopharyngeal Osteoradionecrosis. Otolaryng Head Neck 148(4):633-636.

155. Rice, K. C., E. E. Mann, J. L. Endres, E. C. Weiss, J. E. Cassat, M. S. Smeltzer, and K. W. Bayles. 2007. The cidA murein hydrolase regulator contributes to DNA release and biofilm development in Staphylococcus aureus. P Natl Acad Sci USA 104(19):8113-8118.

156. Fletcher, M. 1977. The effects of culture concentration and age, time, and temperature on bacterial attachment to polystyrene. Canadian Journal of Microbiology 23(1):1-6.

157. Djordjevic, D., M. Wiedmann, and L. A. McLandsborough. 2002. Microtiter plate assay for assessment of Listeria monocytogenes biofilm formation. Appl Environ Microb 68(6):2950-2958.

158. Ceri, H., M. E. Olson, C. Stremick, R. R. Read, D. Morck, and A. Buret. 1999. The Calgary Biofilm Device: New technology for rapid determination of antibiotic susceptibilities of bacterial biofilms. J Clin Microbiol 37(6):1771-1776.

159. McCoy, W. F., J. D. Bryers, J. Robbins, and J. W. Costerton. 1981. Observations of fouling biofilm formation. Canadian Journal of Microbiology 27(9):910-917.

160. Linton, C. J., A. Sherriff, and M. R. Millar. 1999. Use of a modified Robbins device to directly compare the adhesion of Staphylococcus epidermidis RP62A to surfaces. J Appl Microbiol 86(2):194-202.

161. Manz, W., U. Szewzyk, P. Ericsson, R. Amann, K. H. Schleifer, and T. A. Stenström. 1993. In situ identification of bacteria in drinking water and adjoining biofilms by hybridization with 16S and 23S rRNA-directed fluorescent oligonucleotide probes. Appl Environ Microb 59(7):2293-2298.

162. Teodosio, J. S., M. Simoes, and F. J. Mergulhao. 2012. The influence of nonconjugative Escherichia coli plasmids on biofilm formation and resistance. J Appl Microbiol 113(2):373-382.

163. Haagensen, J. A. J., M. Klausen, R. K. Ernst, S. I. Miller, A. Folkesson, T. Tolker-Nielsen, and S. Molin. 2007. Differentiation and distribution of colistin- and sodium dodecyl sulfate-tolerant cells in Pseudomonas aeruginosa biofilms. J Bacteriol 189(1):28-37.

164. Moller, S., C. Sternberg, J. B. Andersen, B. B. Christensen, J. L. Ramos, M. Givskov, and S. Molin. 1998. In situ gene expression in mixed-culture biofilms: Evidence of metabolic interactions between community members. Appl Environ Microb 64(2):721-732.

165. Sternberg, C., B. B. Christensen, T. Johansen, A. T. Nielsen, J. B. Andersen, M. Givskov, and S. Molin. 1999. Distribution of bacterial growth activity in flow-chamber biofilms. Appl Environ Microb 65(9):4108-4117.

166. Lewandowski, Z., H. Beyenal, and D. Stookey. 2004. Reproducibility of biofilm processes and the meaning of steady state in biofilm reactors. Water Sci Technol 49(11-12):359-364.

167. Bakker, D. P., A. van der Mats, G. J. Verkerke, H. J. Busscher, and H. C. van der Mei. 2003. Comparison of velocity profiles for different flow chamber designs used in studies of microbial adhesion to surfaces. Appl Environ Microb 69(10):6280-6287.

168. Tolker-Nielsen, T., and C. Sternberg. 2011. Growing and Analyzing Biofilms in Flow Chambers. Current Protocols in Microbiology 21(1):1B.2.1-1B.2.17.

169. Stoodley, P., I. Dodds, J. D. Boyle, and H. M. Lappin-Scott. 1999. Influence of hydrodynamics and nutrients on biofilm structure. J Appl Microbiol 85:19s-28s.

170. Diaz-Pascual, F., R. Hartmann, M. Lempp, L. Vidakovic, B. Song, H. Jeckel, K. M. Thormann, F. H. Yildiz, J. Dunkel, H. Link, C. D. Nadell, and K. Drescher. 2019. Breakdown of Vibrio cholerae biofilm architecture induced by antibiotics disrupts community barrier function. Nat Microbiol 4(12):2136-+.

171. Ulman, V., M. Maska, K. E. G. Magnusson, O. Ronneberger, C. Haubold, N. Harder, P. Matula, P. Matula, D. Svoboda, M. Radojevic, I. Smal, K. Rohr, J. Jalden, H. M. Blau, O. Dzyubachyk, B. Lelieveldt, P. D. Xiao, Y. X. Li, S. Y. Cho, A. C. Dufour, J. C. Olivo-Marin, C. C. Reyes-Aldasoro, J. A. Solis-Lemus, R. Bensch, T. Brox, J. Stegmaier, R. Mikut, S. Wolf, F. A. Hamprecht, T. Esteves, P. Quelhas, O. Demirel, L. Malmstrom, F. Jug, P. Tomancak, E. Meijering, A. Munoz-Barrutia, M. Kozubek, and C. Ortiz-de-Solorzano. 2017. An objective comparison of cell-tracking algorithms. Nature Methods 14(12):1141-+.

172. Buetti-Dinh, A., V. Galli, S. Bellenberg, O. Ilie, M. Herold, S. Christel, M. Boretska, I. V. Pivkin, P. Wilmes, W. Sand, M. Vera, and M. Dopson. 2019. Deep neural networks outperform human expert's capacity in characterizing bioleaching bacterial biofilm composition. Biotechnol Rep (Amst) 22:e00321.

173. Moen, E., D. Bannon, T. Kudo, W. Graf, M. Covert, and D. Van Valen. 2019. Deep learning for cellular image analysis. Nat Methods 16(12):1233-1246.

174. Van Valen, D. A., T. Kudo, K. M. Lane, D. N. Macklin, N. T. Quach, M. M. DeFelice, I. Maayan, Y. Tanouchi, E. A. Ashley, and M. W. Covert. 2016. Deep Learning Automates the Quantitative Analysis of Individual Cells in Live-Cell Imaging Experiments. Plos Comput Biol 12(11):e1005177.

175. Anwar, S. M., M. Majid, A. Qayyum, M. Awais, M. Alnowami, and M. K. Khan. 2018. Medical Image Analysis using Convolutional Neural Networks: A Review. J Med Syst 42(11):226.

176. Haberl, M. G., C. Churas, L. Tindall, D. Boassa, S. Phan, E. A. Bushong, M. Madany, R. Akay, T. J. Deerinck, S. T. Peltier, and M. H. Ellisman. 2018. CDeep3M-Plug-and-Play cloud-based deep learning for image segmentation. Nature Methods 15(9):677-+.

177. Falk, T., D. Mai, R. Bensch, O. Cicek, A. Abdulkadir, Y. Marrakchi, A. Bohm, J. Deubner, Z. Jackel, K. Seiwald, A. Dovzhenko, O. Tietz, C. Dal Bosco, S. Walsh, D. Saltukoglu, T. L. Tay, M. Prinz, K. Palme, M. Simons, I. Diester, T. Brox, and O. Ronneberger. 2019. U-Net: deep learning for cell counting, detection, and morphometry. Nature Methods 16(1):67-+.

178. Ronneberger, O., P. Fischer, and T. Brox. 2015. U-Net: Convolutional Networks for Biomedical Image Segmentation. In Medical Image Computing and Computer-Assisted Intervention – MICCAI 2015. N. Navab, J. Hornegger, W. M. Wells, and A. F. Frangi, editors. Springer International Publishing, Cham. 234-241.

179. Carpenter, A. E., T. R. Jones, M. R. Lamprecht, C. Clarke, I. H. Kang, O. Friman, D. A. Guertin, J. H. Chang, R. A. Lindquist, J. Moffat, P. Golland, and D. M. Sabatini. 2006. CellProfiler: image analysis software for identifying and quantifying cell phenotypes. Genome Biol 7(10).

180. McQuin, C., A. Goodman, V. Chernyshev, L. Kamentsky, B. A. Cimini, K. W. Karhohs, M. Doan, L. Ding, S. M. Rafelski, D. Thirstrup, W. Wiegraebe, S. Singh, T. Becker, J. C. Caicedo, and A. E. Carpenter. 2018. CellProfiler 3.0: Next-generation image processing for biology. PLOS Biology 16(7):e2005970.

181. He, K. M., G. Gkioxari, P. Dollar, and R. Girshick. 2020. Mask R-CNN. Ieee T Pattern Anal 42(2):386-397.

182. Facchetti, G., B. Knapp, I. Flor-Parra, F. Chang, and M. Howard. 2019. Reprogramming Cdr2-Dependent Geometry-Based Cell Size Control in Fission Yeast. Curr Biol 29(2):350-358 e354.

183. Zhang, M., J. Zhang, Y. Wang, J. Wang, A. Achimovich, S. T. Acton, and A. Gahlmann. 2020. Non-invasive single-cell morphometry in living bacterial biofilms. Nat Commun 11:6151.

184. Stewart, E. J., M. Ganesan, J. G. Younger, and M. J. Solomon. 2015. Artificial biofilms establish the role of matrix interactions in staphylococcal biofilm assembly and disassembly. Sci Rep-Uk 5.

185. Shrivastava, A., V. K. Patel, Y. S. Tang, S. C. Yost, F. E. Dewhirst, and H. C. Berg. 2018. Cargo transport shapes the spatial organization of a microbial community. P Natl Acad Sci USA 115(34):8633-8638.

186. Anderson, M., P. J. Sansonetti, and B. S. Marteyn. 2016. Shigella Diversity and Changing Landscape: Insights for the Twenty-First Century. Front Cell Infect Mi 6.

187. Mattock, E., and A. J. Blocker. 2017. How Do the Virulence Factors of Shigella Work Together to Cause Disease ? Front Cell Infect Mi 7.

188. Schroeder, G. N., and H. Hilbi. 2008. Molecular pathogenesis of Shigella spp.: Controlling host cell signaling, invasion, and death by type III secretion. Clin Microbiol Rev 21(1):134-+.

189. Marteyn, B. S., A. D. Gazi, and P. J. Sansonetti. 2012. Shigella A model of virulence regulation in vivo. Gut Microbes 3(2):104-120.

190. Begley, M., C. G. M. Gahan, and C. Hill. 2005. The interaction between bacteria and bile. Fems Microbiol Rev 29(4):625-651.

191. Urdaneta, V., and J. Casadesus. 2017. Interactions between Bacteria and Bile Salts in the Gastrointestinal and Hepatobiliary Tracts. Front Med-Lausanne 4.

192. Pope, L. M., K. E. Reed, and S. M. Payne. 1995. Increased Protein Secretion and Adherence to Hela-Cells by Shigella Spp Following Growth in the Presence of Bile-Salts. Infect Immun 63(9):3642-3648.

193. Qin, J. L., M. T. Doyle, E. N. H. Tran, and R. Morona. 2020. The virulence domain of Shigella IcsA contains a subregion with specific host cell adhesion function. Plos One 15(1).

194. Beale, D. J., R. Barratt, D. R. Marlow, M. S. Dunn, E. A. Palombo, P. D. Morrison, and C. Key. 2013. Application of metabolomics to understanding biofilms in water distribution systems: a pilot study. Biofouling 29(3):283-294.

195. Secor, P. R., L. K. Jennings, G. A. James, K. R. Kirker, E. D. Pulcini, K. McInnerney, R. Gerlach, T. Livinghouse, J. K. Hilmer, B. Bothner, P. Fleckman, J. E. Olerud, and P. S. Stewart. 2012. Phevalin (aureusimine B)Production by Staphylococcus aureus Biofilm and Impacts on Human Keratinocyte Gene Expression. Plos One 7(7).

196. Denef, V. J., R. S. Mueller, and J. F. Banfield. 2010. AMD biofilms: using model communities to study microbial evolution and ecological complexity in nature. Isme J 4(5):599-610.

197. Folsom, J. P., L. Richards, B. Pitts, F. Roe, G. D. Ehrlich, A. Parker, A. Mazurie, and P. S. Stewart. 2010. Physiology of Pseudomonas aeruginosa in biofilms as revealed by transcriptome analysis. Bmc Microbiol 10.

198. Grzymski, J. J., A. E. Murray, B. J. Campbell, M. Kaplarevic, G. R. Gao, C. Lee, R. Daniel, A. Ghadiri, R. A. Feldman, and S. C. Cary. 2008. Metagenome analysis of an extreme microbial symbiosis reveals eurythermal adaptation and metabolic flexibility. P Natl Acad Sci USA 105(45):17516-17521.

199. Inskeep, W. P., D. B. Rusch, Z. J. Jay, M. J. Herrgard, M. A. Kozubal, T. H. Richardson, R. E. Macur, N. Hamamura, R. D. Jennings, B. W. Fouke, A. L. Reysenbach, F. Roberto, M. Young, A. Schwartz, E. S. Boyd, J. H. Badger, E. J. Mathur, A. C. Ortmann, M. Bateson, G. Geesey, and M. Frazier. 2010. Metagenomes from High-Temperature Chemotrophic Systems Reveal Geochemical Controls on Microbial Community Structure and Function. Plos One 5(3).

200. Ishii, S., S. Suzuki, T. M. Norden-Krichmar, A. Tenney, P. S. G. Chain, M. B. Scholz, K. H. Nealson, and O. Bretschger. 2013. A novel metatranscriptomic approach to identify gene expression dynamics during extracellular electron transfer. Nature Communications 4.

201. Lenz, A. P., K. S. Williamson, B. Pitts, P. S. Stewart, and M. J. Franklin. 2008. Localized gene expression in Pseudomonas aeruginosa Biofilms. Appl Environ Microb 74(14):4463-4471.

202. Williamson, K. S., L. A. Richards, A. C. Perez-Osorio, B. Pitts, K. McInnerney, P. S. Stewart, and M. J. Franklin. 2012. Heterogeneity in Pseudomonas aeruginosa Biofilms Includes Expression of Ribosome Hibernation Factors in the Antibiotic-Tolerant Subpopulation and Hypoxia-Induced Stress Response in the Metabolically Active Population. J Bacteriol 194(8):2062-2073.

203. Xu, P., and J. Gunsolley. 2014. Application of metagenomics in understanding oral health and disease. Virulence 5(3):424-432.

204. Nina Parker, Mark Schneegurt, Anh-Hue Thi Tu, Philip Lister, and B. M. Forster. 2016. Microbiology. OpenStax, Houston, Texas, https://openstax.org/books/microbiology/pages/2-3-instruments-of-microscopy.

205. Jemielita, M., M. J. Taormina, A. DeLaurier, C. B. Kimmel, and R. Parthasarathy. 2013. Comparing phototoxicity during the development of a zebrafish craniofacial bone using confocal and light sheet fluorescence microscopy techniques. J Biophotonics 6(11-12):920-928.

206. Keller, P. J., A. D. Schmidt, J. Wittbrodt, and E. H. K. Stelzer. 2008. Reconstruction of Zebrafish Early Embryonic Development by Scanned Light Sheet Microscopy. Science 322(5904):1065-1069.

207. Olarte, O. E., J. Andilla, E. J. Gualda, and P. Loza-Alvarez. 2018. Light-sheet microscopy: a tutorial. Advances in Optics and Photonics 10(1).

208. Zernike, v. F. 1934. Beugungstheorie des schneidenver-fahrens und seiner verbesserten form, der phasenkontrastmethode. Physica 1(7-12):689-704.

209. Rocha, J. 2021. Dynamic Assembly of the Type-3 Secretion System in Yersinia enterocolitica Probed by Super-Resolution Fluorescence Imaging. https://doi.org/10.18130/v18133-qqs18133-et18140. PhD Thesis.

210. Durnin, J., J. J. Miceli, and J. H. Eberly. 1988. Comparison of Bessel and Gaussian Beams. Opt Lett 13(2):79-80.

211. Overfelt, P. L., and C. S. Kenney. 1991. Comparison of the Propagation Characteristics of Bessel, Bessel-Gauss, and Gaussian Beams Diffracted by a Circular Aperture. J Opt Soc Am A 8(5):732-745.

212. Durnin, J. 1987. Exact-Solutions for Nondiffracting Beams .1. The Scalar Theory. J Opt Soc Am A 4(4):651-654.

213. Durnin, J., J. J. Miceli, and J. H. Eberly. 1987. Diffraction-Free Beams. Phys Rev Lett 58(15):1499-1501.

214. Maddox, J. 1987. Making Light-Spots Travel Further. Nature 327(6119):183-183.

215. Petsas, K. I., A. B. Coates, and G. Grynberg. 1994. Crystallography of Optical Lattices. Phys Rev A 50(6):5173-5189.

216. Betzig, E. 2005. Sparse and composite coherent lattices. Phys Rev A 71(6).

217. Kner, P., B. B. Chhun, E. R. Griffis, L. Winoto, and M. G. L. Gustafsson. 2009. Super-resolution video microscopy of live cells by structured illumination. Nature Methods 6(5):339-U336.

218. Brillouin, L. 1922. Diffusion de la lumière et des rayons X par un corps transparent homogène. Ann. Phys. 9(17):88-122. 10.1051/anphys/192209170088.

219. Debye, P., and F. W. Sears. 1932. On the scattering of light by supersonic waves. P Natl Acad Sci USA 18:409-414.

220. Lucas, R., and P. Biquard. 1932. Propriétés optiques des milieux solides et liquides soumis aux vibrations élastiques ultra sonores. J. Phys. Radium 3(10):464-477. 10.1051/jphysrad:01932003010046400.

221. Raman, C. V., and N. S. Nagendra Nath. 1935. The Dif fraction of Light by High Frequency Sound Waves. Proc. Ind. Acad. Sci. 2:406-412.

222. Schindelin, J., I. Arganda-Carreras, E. Frise, V. Kaynig, M. Longair, T. Pietzsch, S. Preibisch, C. Rueden, S. Saalfeld, B. Schmid, J. Y. Tinevez, D. J. White, V. Hartenstein, K. Eliceiri, P. Tomancak, and A. Cardona. 2012. Fiji: an open-source platform for biological-image analysis. Nature Methods 9(7):676-682.

223. Hall-Stoodley, L., J. W. Costerton, and P. Stoodley. 2004. Bacterial biofilms: from the natural environment to infectious diseases. Nat Rev Microbiol 2(2):95-108.

224. Nadell, C. D., K. Drescher, and K. R. Foster. 2016. Spatial structure, cooperation and competition in biofilms. Nat Rev Microbiol 14(9):589-600.

225. Persat, A., Y. F. Inclan, J. N. Engel, H. A. Stone, and Z. Gitai. 2015. Type IV pili mechanochemically regulate virulence factors in Pseudomonas aeruginosa. Proc Natl Acad Sci U S A 112(24):7563-7568.

226. Zhang, Q., G. Lambert, D. Liao, H. Kim, K. Robin, C.-k. Tung, N. Pourmand, and R. H. Austin. 2011. Acceleration of Emergence of Bacterial Antibiotic Resistance in Connected Microenvironments. Science 333(6050):1764-1767.

227. Donlan, R. M. 2002. Biofilms: microbial life on surfaces. Emerg Infect Dis 8(9):881-890.

228. Yan, J., and B. L. Bassler. 2019. Surviving as a Community: Antibiotic Tolerance and Persistence in Bacterial Biofilms. Cell host & microbe 26(1):15-21.

229. Kovach, K., M. Davis-Fields, Y. Irie, K. Jain, S. Doorwar, K. Vuong, N. Dhamani, K. Mohanty, A. Touhami, and V. D. Gordon. 2017. Evolutionary adaptations of biofilms infecting cystic fibrosis lungs promote mechanical toughness by adjusting polysaccharide production. NPJ Biofilms Microbiomes 3:1.

230. Vidakovic, L., P. K. Singh, R. Hartmann, C. D. Nadell, and K. Drescher. 2018. Dynamic biofilm architecture confers individual and collective mechanisms of viral protection. Nat Microbiol 3(1):26-31.

231. Berk, V., J. C. N. Fong, G. T. Dempsey, O. N. Develioglu, X. W. Zhuang, J. Liphardt, F. H. Yildiz, and S. Chu. 2012. Molecular Architecture and Assembly Principles of Vibrio cholerae Biofilms. Science 337(6091):236-239.

232. Stewart, E. J., M. Ganesan, J. G. Younger, and M. J. Solomon. 2015. Artificial biofilms establish the role of matrix interactions in staphylococcal biofilm assembly and disassembly. Sci Rep 5:13081.

233. Stewart, E. J., A. E. Satorius, J. G. Younger, and M. J. Solomon. 2013. Role of environmental and antibiotic stress on Staphylococcus epidermidis biofilm microstructure. Langmuir 29(23):7017-7024.

234. Yan, J., A. G. Sharo, H. A. Stone, N. S. Wingreen, and B. L. Bassler. 2016. Vibrio cholerae biofilm growth program and architecture revealed by single-cell live imaging. Proc Natl Acad Sci U S A 113(36):E5337-5343.

235. Drescher, K., J. Dunkel, C. D. Nadell, S. van Teeffelen, I. Grnja, N. S. Wingreen, H. A. Stone, and B. L. Bassler. 2016. Architectural transitions in Vibrio cholerae biofilms at single-cell resolution. Proceedings of the National Academy of Sciences 113(14):E2066-E2072.

236. Hartmann, R., P. K. Singh, P. Pearce, R. Mok, B. Song, F. Díaz-Pascual, J. Dunkel, and K. Drescher. 2019. Emergence of three-dimensional order and structure in growing biofilms. Nature Physics 15(3):251-256.

237. Gregor, I., and J. Enderlein. 2019. Image scanning microscopy. Curr Opin Chem Biol 51:74-83.

238. Waldchen, S., J. Lehmann, T. Klein, S. van de Linde, and M. Sauer. 2015. Light-induced cell damage in live-cell super-resolution microscopy. Sci Rep 5:15348.

239. Nadell, C. D., D. Ricaurte, J. Yan, K. Drescher, and B. L. Bassler. 2017. Flow environment and matrix structure interact to determine spatial competition in Pseudomonas aeruginosa biofilms. Elife 6.

240. Diaz-Pascual, F., R. Hartmann, M. Lempp, L. Vidakovic, B. Song, H. Jeckel, K. M. Thormann, F. H. Yildiz, J. Dunkel, H. Link, C. D. Nadell, and K.

Drescher. 2019. Breakdown of Vibrio cholerae biofilm architecture induced by antibiotics disrupts community barrier function. Nat Microbiol.

241. Qin, B., C. Fei, A. A. Bridges, A. A. Mashruwala, H. A. Stone, N. S. Wingreen, and B. L. Bassler. 2020. Cell position fates and collective fountain flow in bacterial biofilms revealed by light-sheet microscopy. Science.

242. Wu, Y., P. Wawrzusin, J. Senseney, R. S. Fischer, R. Christensen, A. Santella, A. G. York, P. W. Winter, C. M. Waterman, and Z. Bao. 2013. Spatially isotropic four-dimensional imaging with dual-view plane illumination microscopy. Nature biotechnology 31(11):1032-1038.

243. Flemming, H. C., and S. Wuertz. 2019. Bacteria and archaea on Earth and their abundance in biofilms. Nat Rev Microbiol 17(4):247-260.

244. Ulman, V., M. Maska, K. E. G. Magnusson, O. Ronneberger, C. Haubold, N. Harder, P. Matula, P. Matula, D. Svoboda, M. Radojevic, I. Smal, K. Rohr, J. Jalden, H. M. Blau, O. Dzyubachyk, B. Lelieveldt, P. Xiao, Y. Li, S. Y. Cho, A. C. Dufour, J. C. Olivo-Marin, C. C. Reyes-Aldasoro, J. A. Solis-Lemus, R. Bensch, T. Brox, J. Stegmaier, R. Mikut, S. Wolf, F. A. Hamprecht, T. Esteves, P. Quelhas, O. Demirel, L. Malmstrom, F. Jug, P. Tomancak, E. Meijering, A. Munoz-Barrutia, M. Kozubek, and C. Ortiz-de-Solorzano. 2017. An objective comparison of cell-tracking algorithms. Nat Methods 14(12):1141-1152.

245. Source code available at: https://github.com/GahlmannLab/BCM3D.git.

246. Stringer, C., T. Wang, M. Michaelos, and M. Pachitariu. 2020. Cellpose: a generalist algorithm for cellular segmentation. bioRxiv:2020.2002.2002.931238.

247. Chen, B. C., W. R. Legant, K. Wang, L. Shao, D. E. Milkie, M. W. Davidson, C. Janetopoulos, X. S. Wu, J. A. Hammer, and Z. Liu. 2014. Lattice light-sheet microscopy: imaging molecules to embryos at high spatiotemporal resolution. Science 346(6208):1257998.

248. Valm, A. M., S. Cohen, W. R. Legant, J. Melunis, U. Hershberg, E. Wait, A. R. Cohen, M. W. Davidson, E. Betzig, and J. Lippincott-Schwartz. 2017.

Applying systems-level spectral imaging and analysis to reveal the organelle interactome. Nature 546(7656):162.

249. Glass, D. S., and I. H. Riedel-Kruse. 2018. A synthetic bacterial cell-cell adhesion toolbox for programming multicellular morphologies and patterns. Cell 174(3):649-658. e616.

250. Cotter, C. R., H. B. Schuttler, O. A. Igoshin, and L. J. Shimkets. 2017. Data-driven modeling reveals cell behaviors controlling self-organization during Myxococcus xanthus development. Proc Natl Acad Sci U S A 114(23):E4592-E4601.

251. Gao, R., S. M. Asano, S. Upadhyayula, I. Pisarev, D. E. Milkie, T.-L. Liu, V. Singh, A. Graves, G. H. Huynh, and Y. Zhao. 2019. Cortical column and whole-brain imaging with molecular contrast and nanoscale resolution. Science 363(6424):eaau8302.

252. Goddard, T. D., C. C. Huang, E. C. Meng, E. F. Pettersen, G. S. Couch, J. H. Morris, and T. E. Ferrin. 2018. UCSF ChimeraX: Meeting modern challenges in visualization and analysis. Protein Sci 27(1):14-25.

253. Rudge, T. J., P. J. Steiner, A. Phillips, and J. Haseloff. 2012. Computational modeling of synthetic microbial biofilms. ACS Synth Biol 1(8):345-352.

254. Reshes, G., S. Vanounou, I. Fishov, and M. Feingold. 2008. Cell shape dynamics in Escherichia coli. Biophysical journal 94(1):251-264.

255. Starruß, J., F. Peruani, V. Jakovljevic, L. Søgaard-Andersen, A. Deutsch, and M. Bär. 2012. Pattern-formation mechanisms in motility mutants of Myxococcus xanthus. Interface focus 2(6):774-785.

256. Harris, L. G., S. Foster, and R. G. Richards. 2002. An introduction to Staphylococcus aureus, and techniques for identifying and quantifying S. aureus adhesins in relation to adhesion to biomaterials: review. Eur Cell Mater 4(3):39-60.

257. Yan, T., C. J. Richardson, M. Zhang, and A. Gahlmann. 2019. Computational correction of spatially variant optical aberrations in 3D single-molecule localization microscopy. Optics Express 27(9):12582-12599.

258. Muller, F. D., C. W. Schink, E. Hoiczyk, E. Cserti, and P. I. Higgs. 2012. Spore formation in Myxococcus xanthus is tied to cytoskeleton functions and polysaccharide spore coat deposition. Mol Microbiol 83(3):486-505.

259. Schindelin, J., I. Arganda-Carreras, E. Frise, V. Kaynig, M. Longair, T. Pietzsch, S. Preibisch, C. Rueden, S. Saalfeld, and B. Schmid. 2012. Fiji: an open-source platform for biological-image analysis. Nature methods 9(7):676-682.

260. Çiçek, Ö., A. Abdulkadir, S. S. Lienkamp, T. Brox, and O. Ronneberger. 2016. 3D U-Net: Learning Dense Volumetric Segmentation from Sparse Annotation. Springer International Publishing, Cham. 424-432.

261. Gibson, E., W. Li, C. Sudre, L. Fidon, D. I. Shakir, G. Wang, Z. Eaton-Rosen, R. Gray, T. Doel, Y. Hu, T. Whyntie, P. Nachev, M. Modat, D. C. Barratt, S. Ourselin, M. J. Cardoso, and T. Vercauteren. 2018. NiftyNet: a deep-learning platform for medical imaging. Computer Methods and Programs in Biomedicine 158:113-122.

262. Acton, S. T. 2001. Fast Algorithms for Area Morphology. Digit Signal Process 11(3):187-203.

263. Jaccard, P. 1912. The distribution of the flora in the alpine zone. New Phytologist 11(2):37-50.

264. Yu, Y., and S. T. Acton. 2002. Speckle reducing anisotropic diffusion. Trans. Img. Proc. 11(11):1260-1270.

265. Tabassum, N., A. Vaccari, and S. Acton. 2018. Speckle removal and change preservation by distance-driven anisotropic diffusion of synthetic aperture radar temporal stacks. Digit Signal Process 74:43-55.

266. Choi, H. I., S. W. Choi, and H. P. Moon. 1997. Mathematical theory of medial axis transform. Pacific Journal of Mathematics 181(1):57-88.

267. Yan, T. Q., and C. X. Zhou. 2012. A Continuous Skeletonization Method Based on Distance Transform. Comm Com Inf Sc 304:251-258.

268. Wang, J., T. Batabyal, M. X. Zhang, J. Zhang, A. Aziz, A. Gahlmann, and S. T. Acton. 2019. LCuts: Linear Clustering of Bacteria Using Recursive Graph

Cuts. 2019 IEEE International Conference on Image Processing (ICIP):1575-1579.

269. Source code available at: https://github.com/jwang-c/Postprocessing-using-LCuts.

270. Shi, J. B., and J. Malik. 2000. Normalized cuts and image segmentation. Ieee Transactions on Pattern Analysis and Machine Intelligence 22(8):888-905.

271. Weigert, M., U. Schmidt, R. Haase, K. Sugawara, and G. Myers. 2020. Star-convex Polyhedra for 3D Object Detection and Segmentation in Microscopy. In 2020 IEEE Winter Conference on Applications of Computer Vision (WACV). 3655-3662.

272. Ester, M., H.-P. Kriegel, J. Sander, and X. Xu. 1996. A density-based algorithm for discovering clusters a density-based algorithm for discovering clusters in large spatial databases with noise. In Proceedings of the Second International Conference on Knowledge Discovery and Data Mining. AAAI Press, Portland, Oregon. 226-231.

273. Moen, E., D. Bannon, T. Kudo, W. Graf, M. Covert, and D. Van Valen. 2019. Deep learning for cellular image analysis. Nat Methods.

274. Caicedo, J. C., J. Roth, A. Goodman, T. Becker, K. W. Karhohs, M. Broisin, C. Molnar, C. McQuin, S. Singh, F. J. Theis, and A. E. Carpenter. 2019. Evaluation of Deep Learning Strategies for Nucleus Segmentation in Fluorescence Images. Cytometry Part A 95(9):952-965.

275. Reyer, M. A., E. L. McLean, S. Chennakesavalu, and J. Y. Fei. 2018. An Automated Image Analysis Method for Segmenting Fluorescent Bacteria in Three Dimensions. Biochemistry-Us 57(2):209-215.

276. Berg, S., D. Kutra, T. Kroeger, C. N. Straehle, B. X. Kausler, C. Haubold, M. Schiegg, J. Ales, T. Beier, and M. Rudy. 2019. Ilastik: interactive machine learning for (bio) image analysis. Nature Methods:1-7.

277. McQuin, C., A. Goodman, V. Chernyshev, L. Kamentsky, B. A. Cimini, K. W. Karhohs, M. Doan, L. Ding, S. M. Rafelski, D. Thirstrup, W. Wiegraebe, S. Singh, T. Becker, J. C. Caicedo, and A. E. Carpenter. 2018. CellProfiler

3.0: Next-generation image processing for biology. PLoS Biol 16(7):e2005970.

278. Kroos, L. 2017. Highly Signal-Responsive Gene Regulatory Network Governing Myxococcus Development. Trends Genet 33(1):3-15.

279. Moon, S., R. Yan, S. J. Kenny, Y. Shyu, L. Xiang, W. Li, and K. Xu. 2017. Spectrally resolved, functional super-resolution microscopy reveals nanoscale compositional heterogeneity in live-cell membranes. Journal of the American Chemical Society 139(32):10944-10947.

280. Bramkamp, M., and D. Lopez. 2015. Exploring the existence of lipid rafts in bacteria. Microbiol. Mol. Biol. Rev. 79(1):81-100.

281. Zou, S. B., S. J. Hersch, H. Roy, J. B. Wiggers, A. S. Leung, S. Buranyi, J. L. Xie, K. Dare, M. Ibba, and W. W. Navarre. 2012. Loss of elongation factor P disrupts bacterial outer membrane integrity. Journal of bacteriology 194(2):413-425.

282. Gonelimali, F. D., J. Lin, W. Miao, J. Xuan, F. Charles, M. Chen, and S. R. Hatab. 2018. Antimicrobial properties and mechanism of action of some plant extracts against food pathogens and spoilage microorganisms. Frontiers in microbiology 9:1639.

283. Parasassi, T., G. De Stasio, A. d'Ubaldo, and E. Gratton. 1990. Phase fluctuation in phospholipid membranes revealed by Laurdan fluorescence. Biophysical journal 57(6):1179-1186.

284. Strahl, H., and L. W. Hamoen. 2010. Membrane potential is important for bacterial cell division. Proceedings of the National Academy of Sciences 107(27):12281-12286.

285. Prindle, A., J. Liu, M. Asally, S. Ly, J. Garcia-Ojalvo, and G. M. Süel. 2015. Ion channels enable electrical communication in bacterial communities. Nature 527(7576):59-63.

286. Weigert, M., U. Schmidt, T. Boothe, A. Müller, A. Dibrov, A. Jain, B. Wilhelm, D. Schmidt, C. Broaddus, and S. Culley. 2018. Content-aware

image restoration: pushing the limits of fluorescence microscopy. Nature methods 15(12):1090-1097.

287. Krull, A., T. Vicar, and F. Jug. 2019. Probabilistic Noise2Void: Unsupervised content-aware denoising. arXiv preprint arXiv:1906.00651.

288. Krull, A., T.-O. Buchholz, and F. Jug. 2019. Noise2void-learning denoising from single noisy images. In Proceedings of the IEEE Conference on Computer Vision and Pattern Recognition. 2129-2137.

289. Buchholz, T.-O., M. Prakash, A. Krull, and F. Jug. 2020. DenoiSeg: Joint Denoising and Segmentation. arXiv preprint arXiv:2005.02987.

290. Sakellaris, H., N. K. Hannink, K. Rajakumar, D. Bulach, M. Hunt, C. Sasakawa, and B. Adler. 2000. Curli loci of Shigella spp. Infect Immun 68(6):3780-3783.

291. Carayol, N., and G. T. V. Nhieu. 2013. The Inside Story of Shigella Invasion of Intestinal Epithelial Cells. Csh Perspect Med 3(10).

292. Al-Kofahi, O., R. J. Radke, S. K. Goderie, Q. Shen, S. Temple, and B. Roysam. 2006. Automated cell lineage construction - A rapid method to analyze clonal development established with murine neural progenitor cells. Cell Cycle 5(3):327-335.

293. Dufour, A., R. Thibeaux, E. Labruyere, N. Guillen, and J. C. Olivo-Marin. 2011. 3-D Active Meshes: Fast Discrete Deformable Models for Cell Tracking in 3-D Time-Lapse Microscopy. Ieee T Image Process 20(7):1925-1937.

294. Dzyubachyk, O., W. A. van Cappellen, J. Essers, W. J. Niessen, and E. Meijering. 2010. Advanced Level-Set-Based Cell Tracking in Time-Lapse Fluorescence Microscopy. Ieee T Med Imaging 29(3):852-867.

295. Harder, N., R. Batra, N. Diessl, S. Gogolin, R. Eils, F. Westermann, R. Konig, and K. Rohr. 2015. Large-scale tracking and classification for automatic analysis of cell migration and proliferation, and experimental optimization of high-throughput screens of neuroblastoma cells. Cytom Part A 87a(6):524-540.

296. Li, F. H., X. B. Zhou, J. W. Ma, and S. T. C. Wong. 2010. Multiple Nuclei Tracking Using Integer Programming for Quantitative Cancer Cell Cycle Analysis. Ieee T Med Imaging 29(1):96-105.

297. Li, K., E. D. Miller, M. Chen, T. Kanade, L. E. Weiss, and P. G. Campbell. 2008. Cell population tracking and lineage construction with spatiotemporal context. Med Image Anal 12(5):546-566.

298. Magnusson, K. E. G., J. Jalden, P. M. Gilbert, and H. M. Blau. 2015. Global Linking of Cell Tracks Using the Viterbi Algorithm. Ieee T Med Imaging 34(4):911-929.

299. Maska, M., O. Danek, S. Garasa, A. Rouzaut, A. Munoz-Barrutia, and C. Ortiz-de-Solorzano. 2013. Segmentation and Shape Tracking of Whole Fluorescent Cells Based on the Chan-Vese Model. Ieee T Med Imaging 32(6):995-1006.

300. Meijering, E. 2012. Cell Segmentation: 50 Years Down the Road. Ieee Signal Proc Mag 29(5):140-145.

301. Padfield, D., J. Rittscher, and B. Roysam. 2011. Coupled minimum-cost flow cell tracking for high-throughput quantitative analysis. Med Image Anal 15(4):650-668.

302. Padfield, D., J. Rittscher, N. Thomas, and B. Roysam. 2009. Spatio-temporal cell cycle phase analysis using level sets and fast marching methods. Med Image Anal 13(1):143-155.

303. Matula, P., M. Maska, D. V. Sorokin, P. Matula, C. Ortiz-de-Solorzano, and M. Kozubek. 2015. Cell Tracking Accuracy Measurement Based on Comparison of Acyclic Oriented Graphs. Plos One 10(12).

304. Ortiz-de-Solorzano, C., A. Munoz-Barrutia, E. Meijering, and M. Kozubek. 2015. Toward a Morphodynamic Model of the Cell [Signal processing for cell modeling]. Ieee Signal Proc Mag 32(1):20-29.

305. He, T., H. Mao, J. X. Guo, and Z. Yi. 2017. Cell tracking using deep neural networks with multi-task learning. Image Vision Comput 60:142-153.

306. Xing, F. Y., Y. P. Xie, H. Su, F. J. Liu, and L. Yang. 2018. Deep Learning in Microscopy Image Analysis: A Survey. Ieee T Neur Net Lear 29(10):4550-4568.

307. Falk, T., D. Mai, R. Bensch, O. Cicek, A. Abdulkadir, Y. Marrakchi, A. Bohm, J. Deubner, Z. Jackel, K. Seiwald, A. Dovzhenko, O. Tietz, C. Dal Bosco, S. Walsh, D. Saltukoglu, T. L. Tay, M. Prinz, K. Palme, M. Simons, I. Diester, T. Brox, and O. Ronneberger. 2019. U-Net: deep learning for cell counting, detection, and morphometry. Nat Methods 16(1):67-70.

308. Kuhn, H. W. 2005. The Hungarian Method for the assignment problem. Nav Res Log 52(1):7-21.

309. Labrec, E. H., H. Schneider, T. J. Magnani, and S. B. Formal. 1964. EPITHELIAL CELL PENETRATION AS AN ESSENTIAL STEP IN THE PATHOGENESIS OF BACILLARY DYSENTERY. J Bacteriol 88(5):1503-1518.

310. Kuhn, H. W. 1955. The Hungarian method for the assignment problem. Naval research logistics quarterly 2(1‐2):83-97.

311. Tinevez, J.-Y. 2019. simpletracker (https://github.com/tinevez/simpletracker).

312. Matula, P., M. Maska, D. V. Sorokin, P. Matula, C. Ortiz-de-Solorzano, and M. Kozubek. 2015. Cell Tracking Accuracy Measurement Based on Comparison of Acyclic Oriented Graphs. PLoS One 10(12):e0144959.

313. Michalet, X., and A. J. Berglund. 2012. Optimal diffusion coefficient estimation in single-particle tracking. Physical Review E 85(6).

314. Kim, Y. C. 1996. Diffusivity of bacteria. Korean J Chem Eng 13(3):282-287.

315. Licata, N. A., B. Mohari, C. Fuqua, and S. Setayeshgar. 2016. Diffusion of Bacterial Cells in Porous Media. Biophysical Journal 110(1):247-257.

316. Patteson, A. E., A. Gopinath, M. Goulian, and P. E. Arratia. 2015. Running and tumbling with E-coli in polymeric solutions. Sci Rep-Uk 5.

317. Wu, M. M., J. W. Roberts, S. Kim, D. L. Koch, and M. P. DeLisa. 2006. Collective bacterial dynamics revealed using a three-dimensional population-

scale defocused particle tracking technique. Appl Environ Microb 72(7):4987-4994.

318. Berg, H. C. 2003. The rotary motor of bacterial flagella. Annu Rev Biochem 72:19-54.

319. Tailleur, J., and M. E. Cates. 2008. Statistical mechanics of interacting run-and-tumble bacteria. Phys Rev Lett 100(21).

320. Lauga, E. 2016. Bacterial Hydrodynamics. Annu Rev Fluid Mech 48:105-130.

321. Mannik, J., R. Driessen, P. Galajda, J. E. Keymer, and C. Dekker. 2009. Bacterial growth and motility in sub-micron constrictions. P Natl Acad Sci USA 106(35):14861-14866.

322. Bhattacharjee, T., and S. S. Datta. 2019. Bacterial hopping and trapping in porous media. Nature Communications 10.

323. Sosa-Hernandez, J. E., M. Santillan, and J. Santana-Solano. 2017. Motility of Escherichia coli in a quasi-two-dimensional porous medium. Phys Rev E 95(3).

324. Theves, M., J. Taktikos, V. Zaburdaev, H. Stark, and C. Beta. 2015. Random walk patterns of a soil bacterium in open and confined environments. Epl-Europhys Lett 109(2).

325. Zhong, H., G. S. Liu, Y. B. Jiang, J. Z. Yang, Y. Liu, X. Yang, Z. F. Liu, and G. M. Zeng. 2017. Transport of of bacteria in porous media and its enhancement by surfactants for bioaugmentation: A review. Biotechnol Adv 35(4):490-504.

326. Floury, J., I. El Mourdi, J. V. C. Silva, S. Lortal, A. Thierry, and S. Jeanson. 2015. Diffusion of solutes inside bacterial colonies immobilized in model cheese depends on their physicochemical properties: a time-lapse microscopy study. Frontiers in Microbiology 6.

327. Gonzalez, S., L. Fernandez, D. Gutierrez, A. B. Campelo, A. Rodriguez, and P. Garcia. 2018. Analysis of Different Parameters Affecting Diffusion,

Propagation and Survival of Staphylophages in Bacterial Biofilms. Frontiers in Microbiology 9.

328. Kosztolowicz, T., and R. Metzler. 2020. Diffusion of antibiotics through a biofilm in the presence of diffusion and absorption barriers. Phys Rev E 102(3).

329. Stewart, P. S. 1996. Theoretical aspects of antibiotic diffusion into microbial biofilms. Antimicrob Agents Ch 40(11):2517-2522.

330. Stewart, P. S. 2003. Diffusion in biofilms. J Bacteriol 185(5):1485-1491.

331. Stewart, P. S., T. Y. Zhang, R. F. Xu, B. Pitts, M. C. Walters, F. Roe, J. Kikhney, and A. Moter. 2016. Reaction-diffusion theory explains hypoxia and heterogeneous growth within microbial biofilms associated with chronic infections. Npj Biofilms Microbi 2.

332. Goldberg, M. B. 2001. Actin-based motility of intracellular microbial pathogens. Microbiol Mol Biol R 65(4):595-+.

333. Southwick, F. S., E. D. Adamson, and D. L. Purich. 2000. Shigella actin-based motility in the presence of truncated vinculin. Cell Motility 45(4):272-278.

334. Bernardini, M. L., J. Mounier, H. Dhauteville, M. Coquisrondon, and P. J. Sansonetti. 1989. Identification of Icsa, a Plasmid Locus of Shigella-Flexneri That Governs Bacterial Intra-Cellular and Intercellular Spread through Interaction with F-Actin. P Natl Acad Sci USA 86(10):3867-3871.

335. Makino, S., C. Sasakawa, K. Kamata, T. Kurata, and M. Yoshikawa. 1986. A Genetic Determinant Required for Continuous Reinfection of Adjacent Cells on Large Plasmid in Shigella-Flexneri 2a. Cell 46(4):551-555.

336. Lee, C. K., J. de Anda, A. E. Baker, R. R. Bennett, Y. Luo, E. Y. Lee, J. A. Keefe, J. S. Helali, J. Ma, K. Zhao, R. Golestanian, G. A. O'Toole, and G. C. L. Wong. 2018. Multigenerational memory and adaptive adhesion in early bacterial biofilm communities. Proc Natl Acad Sci U S A.

337. Human Microbiome Project Consortium. 2012. Structure, function and diversity of the healthy human microbiome. Nature 486(7402):207-214.

338. Bjarnsholt, T., M. Alhede, M. Alhede, S. R. Eickhardt-Sørensen, C. Moser, M. Kühl, P. Jensen, and N. Høiby. 2013. The in vivo biofilm. Trends Microbiol 21(9):466-474.

339. Prince, A. S. 2002. Biofilms, Antimicrobial Resistance, and Airway Infection. New England Journal of Medicine 347(14):1110-1111.

340. Srivastava, A., E. Klassen, S. H. Joshi, and I. H. Jermyn. 2011. Shape Analysis of Elastic Curves in Euclidean Spaces. IEEE Transactions on Pattern Analysis and Machine Intelligence 33(7):1415-1428.

341. Wang, J., Z. Fu, N. Sadeghzadehyazdi, J. Kipnis, and S. T. Acton. 2018. Nonlinear Shape Regression for Filtering Segmentation Results from Calcium Imaging. In 2018 25th IEEE International Conference on Image Processing (ICIP). 738-742.

342. You, Y., W. Huang, K. A. Gallivan, and P. Absil. 2015. A Riemannian approach for computing geodesies in elastic shape analysis. In 2015 IEEE Global Conference on Signal and Information Processing (GlobalSIP). 727-731.

343. Zhang, Z., O. A. Igoshin, C. R. Cotter, and L. J. Shimkets. 2018. Agent-Based Modeling Reveals Possible Mechanisms for Observed Aggregation Cell Behaviors. Biophysical journal 115(12):2499-2511.

344. Gahlmann, A., J. L. Ptacin, G. Grover, S. Quirin, A. R. S. von Diezmann, M. K. Lee, M. P. Backlund, L. Shapiro, R. Piestun, and W. E. Moerner. 2013. Quantitative Multicolor Subdiffraction Imaging of Bacterial Protein Ultrastructures in Three Dimensions. Nano Letters 13(3):987-993.

345. Ptacin, J. L., A. Gahlmann, G. R. Bowman, A. M. Perez, A. R. von Diezmann, M. R. Eckart, W. E. Moerner, and L. Shapiro. 2014. Bacterial scaffold directs pole-specific centromere segregation. Proc Natl Acad Sci U S A 111(19):E2046-2055.

346. Friedrich, C., I. Bulyha, and L. Sogaard-Andersen. 2014. Outside-In Assembly Pathway of the Type IV Pilus System in Myxococcus xanthus. J Bacteriol 196(2):378-390.

347. Achimovich, A. M., H. Ai, and A. Gahlmann. 2019. Enabling technologies in super-resolution fluorescence microscopy: reporters, labeling, and methods of measurement. Current Opinion in Structural Biology 58:224-232.

348. Rocha, J. M., C. J. Richardson, M. Zhang, C. M. Darch, E. Cai, A. Diepold, and A. Gahlmann. 2018. Single-molecule tracking in live Yersinia enterocolitica reveals distinct cytosolic complexes of injectisome subunits. Integrative Biology 10(9):502-515.

349. Rocha, J., J. Corbitt, T. Yan, C. Richardson, and A. Gahlmann. 2019. Resolving Cytosolic Diffusive States in Bacteria by Single-Molecule Tracking. Biophysical journal 116(10):1970-1983.

350. Rocha, J. M., and A. Gahlmann. 2019. Single-Molecule Tracking Microscopy - A Tool for Determining the Diffusive States of Cytosolic Molecules. Journal of Visualized Experiments 151(151):e59387.

351. Chanin, R. B., K. P. Nickerson, A. Llanos-Chea, J. R. Sistrunk, D. A. Rasko, D. K. V. Kumar, J. de la Parra, J. R. Auclair, J. Ding, K. Li, S. K. Dogiparthi, B. J. D. Kusber, and C. S. Faherty. 2019. Shigella flexneri Adherence Factor Expression in In Vivo-Like Conditions. mSphere 4(6).

352. Ranganathan, S., M. Doucet, C. L. Grassel, B. Delaine-Elias, N. C. Zachos, and E. M. Barry. 2019. Evaluating *Shigella flexneri* Pathogenesis in the Human Enteroid Model. Infection and Immunity 87(4):e00740-00718.

353. Koestler, B. J., C. M. Ward, C. R. Fisher, A. Rajan, A. W. Maresso, and S. M. Payne. 2019. Human Intestinal Enteroids as a Model System of Shigella Pathogenesis. Infect Immun 87(4).